Thesis

Extreme hip movements based on optical motion capture

CHARBONNIER, Caecilia

Abstract

Many causes can be at the origin of hip osteoarthritis, but the exact pathogenesis for idiopathic osteoarthritis has not yet been clearly delineated. Indeed, changes in the movement and alignment of the hip could be other potential causes of early osteoarthritis. In particular, athletes seem to present a higher risk of developing such disease due to repetitive and extreme movements performed during their daily activities. In this thesis, a clinical study with professional ballet dancers is being conducted. The goal of this study is to verify if repetitive extreme movements can be a factor of hip joint degeneration through joint subluxation and excessive cartilage deformations. To achieve these goals, we developed a motion protocol using optical motion capture system to estimate the kinematics of patient-specific hip joint 3D models. We also developed an effective and robust correction method to minimize soft tissue artifacts, a critical issue in human motion analysis.

Reference

CHARBONNIER, Caecilia. *Extreme hip movements based on optical motion capture*. Thèse de doctorat : Univ. Genève, 2010, no. Sc. 4193

UNIVERSITÉ DE GENÈVE

FACULTÉ DES SCIENCES

Département d'informatique — Professeur José Rolim

FACULTÉ DES SCIENCES
ÉCONOMIQUES ET SOCIALES

Département de systèmes d'information — Professeur Nadia Magnenat-Thalmann

---

Extreme Hip Movements Based on Optical Motion Capture

THÈSE

présentée à la Faculté des sciences de l'Université de Genève
pour obtenir le grade de Docteur ès sciences, mention interdisciplinaire

par

Caecilia CHARBONNIER

de

Plan-Les-Ouates (GE)

Thèse N° 4193

GENÈVE

Atelier de reprographie ReproMail

2010

Acknowledgments

My first thanks and gratitude go to my supervisor Prof. Nadia Magnenat-Thalmann for her invaluable support during the time I have been at MIRALab. Many thanks to the jury members: Prof. José Rolim (University of Geneva), Prof. Franz-Erich Wolter (Leibniz Hannover University), Dr. Mark de Zee (Aalborg University) and Dr. Eric Stindel (University Hospital of Brest) for accepting to review the manuscript.

I would like to thank the past and current PhD students of the MIRALab medical group for their kindness and scientific collaboration: Dr. Benjamin Gilles, Jérôme Schmid, Lazhari Assassi and Dr. Lydia Yahia-Cherif. Thanks to Marlène Arévalo-Poizat, Nedjma Cadi, Jody Hausmann and Yacine Benmansour for hours spent on post-processing the motion capture and body scanning data. Thanks to Dr. Etienne Lyard, Dr. Pascal Volino and Dr. Gwenael Guillard for their support and help. Great thanks to other MIRALab members for the friendly working atmosphere. I would also like to credit colleagues from EPFL - Lausanne: Prof. Daniel Thalmann, Dr. Ronan Boulic and Dr. Ehsan Arbabi, and from ARTORG Center Bern: Salman Chegini and Dr. Stephen Fergusson for the enjoyable partnership within the CO-ME project all along these years.

This work would not have been possible without a very active participation from the clinical side: so, many thanks to Dr. Frank Kolo-Christophe, Prof. Christoph Becker from the Department of Radiology, and Dr. Jacques Ménétrey, Dr. Victoria Duthon and Prof. Pierre Hoffmeyer from the Department of Orthopaedic Surgery of the University Hospital of Geneva for their enthusiasm and availability.

I am also grateful to the dancers from the Ballet of the Grand Théâtre de Genève, the Junior Ballet and the Company of Tamara Bacci for having accepted to take part in these studies.

Thanks to CO-ME (Computer Aided and Image Guided Medical Interventions) funded by Swiss

National Research Foundation and FOCUS K3D (FP7-ICT-2007-214993) funded by the European Union for the financial support. I would like to acknowledge the Hans Wilsdorf Foundation for the generous 2007-2009 research grant.

Finally, last but not least, I would like to thank my personal relatives, family and friends, who have supported me over the years, especially my mother, my father and my brother. Special thanks to Caroline Falciola and Clémentine Lo for proofreading the manuscript.

Abstract

Osteoarthritis (OA) is among the leading causes of chronic musculoskeletal disabilities and typical symptoms include functional impairment, pain, stiffness and limited motion. OA commonly affects large weight-bearing joints such as the hips and knees. In some cases, hip OA could be explained by femoroacetabular impingements (FAI) caused by an abnormal morphology of the joint components: a non spherical head (cam FAI) or an acetabular overcoverage (pincer FAI).

Although the mechanism of degeneration in the cam/ pincer -FAI hip is pretty well understood, the exact pathogenesis for idiopathic OA has not yet been clearly delineated. Indeed, changes in the movement (e.g., hyperrotation or hyperabduction of the hip) and alignment of the hip (e.g., subluxation) could be other potential causes of early OA. In particular, athletes seem to present a higher risk of developing OA due to repetitive and extreme movements performed during their daily activities. In this thesis, a clinical study with professional ballet dancers is being conducted. The goal of this study is to verify if repetitive extreme movements can be a factor of hip joint degeneration through joint subluxation and excessive labral deformations. This work aims at investigating methods to identify arthrogenous activities, visualize/ locate femoroacetabular conflicts, and prospectively quantify the range of motion and congruence of the hip joint in extreme postures.

To achieve these goals, the motion of the hip joint must be accurately reproduced. To this end, we use an optical motion capture system to obtain bone poses of patient-specific hip joint 3D models. The major drawback with this system is the soft tissue deformation due to muscle contractions, causing markers movements with respect to the underlying bones. Thus, rigid motion of the bony segments cannot be robustly estimated. Several methods were proposed to reduce these errors, but these techniques do not perform better than traditional bone pose estimators, or are based on invalid assumptions or are limited to the use of non subject-specific models (e.g., ball and socket joints). To solve this issue, we propose in this work an optimized fitting algorithm which accounts for soft tissue artifacts and anatomical constraints, and allows some shifts at the joint. We will demonstrate that

this algorithm is robust, more accurate and converges faster than the classical methods. Moreover, to improve the correspondence between anatomical and motion frames over previous methods, we also present a new anatomical calibration technique. Our technique is based on the 3D body scanning technology and exploits geometric features of the 3D models.

Once the movement of the hip joint is precisely estimated, the morphology and motion of the dancers' hips can be analyzed. To this aim, we propose to investigate several methods, including morphological measurements (e.g., femoral alpha neck angle, acetabular depth, acetabular version), joint congruency quantification and FAI region detection (e.g., by detecting the collisions between the joint tissues). Eventually, the simulation results are compared with the clinical study (i.e., the radiological analysis and the clinical examination).

Résumé

Contexte de recherche

Après des années de développement à MIRALab, les cliniciens peuvent obtenir une vue 3D complète de l'articulation de la hanche, y compris les os et les tissus mous, reconstruite à partir d'algorithmes de segmentation basés sur l'imagerie par résonance magnétique (IRM) [Gil07]. Ce processus est presque automatique et les modèles 3D sont spécifiques aux patients.

Comme la plupart des pathologies sont liées à la cinématique articulaire (niveau fonctionnel), ces modèles 3D statiques ne sont pas suffisants pour diagnostiquer les anomalies et comprendre la physiologie articulaire. Par conséquent, une recherche importante a également été menée à MIRALab dans l'utilisation de techniques non-invasives pour quantifier la cinématique articulaire *in vivo* et *in silico*. Premièrement, des méthodes ont été proposées pour localiser le centre de rotation de la hanche et pour évaluer son amplitude de mouvement [Kan05]. Cette information est importante pour la planification chirurgicale. Toutefois, seuls des patients effectuant des mouvements d'amplitude normale ont été étudiés. Le comportement de la hanche lors de l'exécution de postures extrêmes (ex : postures de danse) est donc encore inconnu. Deuxièmement, un autre travail combinant IRM dynamique et capture de mouvement optique a été réalisé [YC06]. L'IRM dynamique était utilisée pour quantifier le déplacement des marqueurs et pour développer un algorithme de correction afin de réduire les erreurs de mouvement de peau liées aux systèmes de capture optique. Malgré une approche intéressante, cette méthode utilisait un squelette virtuel pour évaluer le mouvement lors de l'utilisation du système optique. Cette méthodologie n'était donc pas spécifique au sujet, était simplifiée au niveau de la modélisation des articulations et était sujette à de nombreuses erreurs lors de la calibration du squelette (erreur $\approx 2cm$ par segment), ce qui n'est pas suffisamment précis pour des applications médicales. De nouveaux travaux de recherche sont donc nécessaires dans ce domaine.

De nos jours, l'accent est mis sur la simulation physique. En effet, l'analyse du stress et de la

distribution des contacts dans les tissus mous contribue à la compréhension de la biomécanique de la hanche [MSBT05] [SMBT05] [CBF06] [CBF08]. Cependant, ces techniques ne simulent généralement pas des maillages 3D complexes (par exemple des modèles spécifiques aux patients) lors de mouvements sophistiqués. Le mouvement est typiquement simplifié à des angles anatomiques simples ou à un mouvement de faible amplitude. Pourtant, il est crucial de simuler l'anatomie du patient, ainsi que sa cinématique, puisque de grandes variations anatomiques existent entre les individus et que nous nous déplaçons tous différemment.

Le travail présenté dans cette thèse a été réalisé dans le cadre du projet CO-ME (Computer Aided and Image Guided Medical Interventions)[1]. CO-ME est un projet du Fonds National Suisse de la recherche scientifique, l'objectif global étant de "*développer une visualisation interactive pour l'examen clinique de la hanche*". Nos contributions dans ce projet et dans ce contexte de recherche sont : 1) de fournir le mouvement requis pour la simulation, où les mouvements de peau sont effectivement réduits et 2) d'étudier l'articulation de la hanche dans des postures extrêmes et complexes.

Motivations

Les pathologies liées au système locomoteur sont certainement les causes les plus courantes de douleur et de handicap physique à long terme, affectant plusieurs centaines de millions de personnes a travers le monde. Dans le cadre de cette recherche, un accent particulier est mis sur la détection de signes annonciateurs d'arthrose de la hanche et sur leur traitement ultérieur. Le patient typique souffrant d'arthrose est d'âge moyen ou âgé. Vu que le vieillissement de la population croît à un rythme rapide, une meilleure connaissance de la pathogenèse est nécessaire.

L'arthrose de la hanche pourrait être causée par des conflits fémoroacetabulaires qui se produisent lorsqu'il existe un contact anormal entre le fémur et le cotyle dû à des anomalies morphologiques [RLK99] [InL$^+$01] [GPB$^+$03] [LPB$^+$04] [BKG05] [PMD$^+$06] [TGB$^+$08]. Celles-ci induisent des lésions dégénératives du cartilage et du labrum [TGB$^+$08] [LeG09].

Le mécanisme de ces conflits semblerait également être l'une des principales causes du développement de l'arthrose précoce chez les jeunes adultes pratiquant des mouvements répétitifs et extrêmes (ex : les danseurs, les gymnastes, etc.). En effet, des changements dans le mouvement et dans l'alignement de la hanche pourraient mener à une usure excessive des surfaces articulaires [Mas01] [Bin03] [LS06]. Des rotations externes récurrentes [Mas01] [MNS$^+$01] [MNA$^+$03] [Bin03] [CKH$^+$09] [GH09] ou des

[1] `http://www.co-me.ch/`, accédé novembre 2009

hyperabductions [NV00] [GH09] de la hanche sembleraient aussi être un facteur critique de micro-traumatismes du labrum. En revanche, les mouvements arthrogènes n'ont point encore été clairement identifiés. De plus, l'amplitude de mouvement de la hanche des personnes effectuant des positions extrêmes n'a pas encore été déterminée. Il est aussi difficile de savoir si la tête fémorale et le cotyle sont congruents dans les positions extrêmes (ex : grand écart). La congruence de l'articulation pourrait être une autre cause potentielle d'arthrose précoce, induisant un stress élevé au niveau du labrum. Par conséquent, le but de ce travail de thèse est de vérifier si les mouvements répétitifs extrêmes pourraient être un facteur de dégénérescence de l'articulation de la hanche, à cause de subluxations et de déformations excessives du labrum. Ce travail vise à mettre en place des méthodes afin d'identifier les activités arthrogènes, de visualiser/ localiser les conflits fémoroacetabulaires, et de prospectivement quantifier l'amplitude de mouvement et la congruence de la hanche dans les postures extrêmes.

Pour atteindre ces objectifs, le mouvement de l'articulation de la hanche doit être fidèlement reproduit. Dans ce but, notre méthodologie traite un thème principal : nous avons élaboré un protocole pour estimer le mouvement des articulations en utilisant un système de capture optique. Comparée à d'autres systèmes, la capture optique n'est pas invasive, mais l'os reste inaccessible. La déformation de la peau et son déplacement (en raison de l'activité musculaire) induisent des déplacements de marqueurs par rapport à l'os (Figure 1). Ces mouvements représentent un artefact qui affecte l'estimation de la cinématique du squelette et est considéré comme la source d'erreur la plus critique dans l'analyse du mouvement humain [LCCC05]. Plusieurs méthodes ont été proposées pour réduire ces erreurs, mais ces techniques souffrent des limitations suivantes :

- Les approches mathématiques, telles que la technique du Point Cluster [AA01], sont instables et ne réussissent pas mieux que les estimateurs traditionnels (ex : l'algorithme de décomposition en valeur singulière [SB93]). Ces approches ne sont donc pas efficaces pour compenser les artefacts de peau.

- Les méthodes, telles que la calibration multiple de repères anatomiques [CSFL05], sont fondées sur des hypothèses invalides (ex : supposer que le mouvement de la peau au cours d'une posture statique est le même que pendant des activités dynamiques).

- Les techniques, telles que l'optimisation globale [LO99], sont limitées par l'utilisation d'articulations à rotule (c'est-à-dire qu'aucune translation articulaires n'est permise), ce qui simplifie la structure de l'articulation et ce qui n'est pas spécifique au sujet.

En conclusion, la correction des artefacts de peau est toujours d'actualité. Dans cette thèse, nous

proposons d'étendre les travaux existants avec une méthode de correction qui combine l'optimisation non-linéaire avec des contraintes de mouvement articulaire, et permet surtout des translations au niveau de l'articulation.

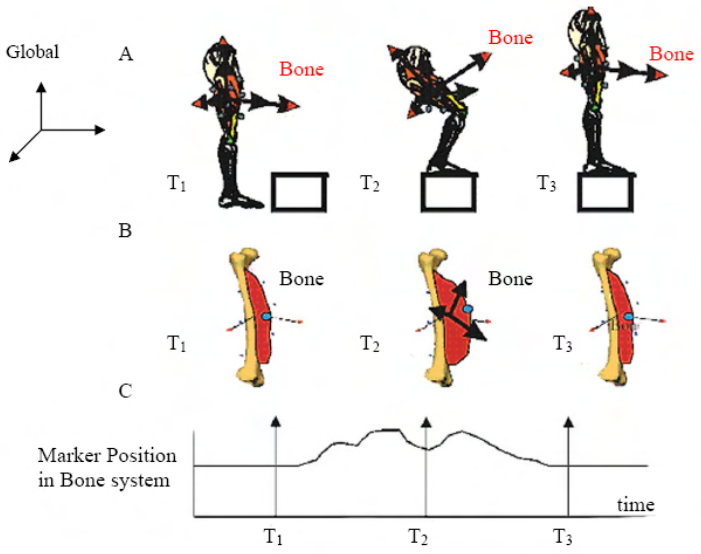

Figure 1: La trajectoire d'un marqueur au cours d'une activité de flexion. En T2, le marqueur se déplace dans le système de coordonnées de l'os, lorsque le muscle se contracte. Image provenant de [AA01], utilisée avec permission.

Une fois que le mouvement de l'articulation de la hanche est estimé de façon précise, une étude clinique peut être effectuée. Ce travail comprend une étude du mouvement de la hanche chez les danseuses professionnelles de ballet, une population sujette à développer de l'arthrose [Mas01] [Bin03] [LS06] [GH09]. En effet, des lésions chondrolabrales caractéristiques sont diagnostiquées à un âge très jeune dans cette population (ex : à l'âge de 18-25 ans). Les questions suivantes sont posées :

- Est-ce que l'arthrose est le résultat unique de conflits fémoroacetabulaires (anomalies morpholigues) ?
- Est-ce que l'arthrose est une conséquence de l'activité des danseuses (mouvements répétitifs extrêmes, subluxations) ?
- Est-ce la morphologie du patient qui n'est pas adaptée au mouvement ?
- Quels sont les patients à risque ?
- Quelles sont les morphologies à risque ?

Pour répondre à ces questions, nous proposons d'examiner plusieurs méthodes, comme d'effectuer des mesures morphologiques (ex : mesure de l'angle alpha, de la profondeur de l'acétabulum, de la version acétabulaire), de quantifier la congruence de l'articulation et de détecter la région du conflit fémoroacetabulaire (ex : en détectant les collisions entre les tissus articulaires). L'enregistrement et l'étude des hanches des danseuses professionnelles de ballet lors de postures extrêmes a pour but de nous fournir un modèle cinématique extrême de l'articulation de la hanche.

Objectifs et contributions

Les objectifs fondamentaux de cette étude sont les suivants :

- L'identification des mouvements arthrogènes à travers l'étude du mouvement de la hanche des danseuses professionnelles de ballet.
- La visualisation et la localisation des conflits fémoroacetabulaires potentiels, et la quantification de l'amplitude de mouvement de la hanche et sa congruence dans les postures extrêmes.
- Une meilleure compréhension de l'arthrose de la hanche en rapport avec la morphologie et la cinématique.
- Le diagnostic précoce de l'arthrose de la hanche, en apportant aux orthopédistes des outils fiables.

Pour atteindre ces objectifs, notre recherche est réalisée en deux étapes :
Tout d'abord, nous avons mis en place un protocole d'estimation du mouvement de la hanche du patient en utilisant un système de capture de mouvement optique. Pour résoudre les problèmes de déformation de la peau, nous proposons une méthode de correction basée sur trois composantes :

- Un estimation par les moindres carrés pour optimiser le calcul des centres de rotation et les orientations des segments. En raison des mouvements non-linéaires des marqueurs [CCL93], nous utilisons un *algorithme de programmation quadratique et séquentiel* [LT01] pour assurer robustesse et convergence rapide.
- Il a été observé [KASS94] que les artefacts de peau peuvent provoquer des translations non-physiologiques ou même des dislocations. Par conséquent, *des contraintes anatomiques* sont appliquées pour éviter ces effets indésirables.
- Bien que le centre de rotation de la hanche puisse être considéré comme étant fixe au cours des mouvements de faible amplitude, ceci n'est pas valide pour les mouvements extrêmes [GKCMT$^+$09].

En effet, une subluxation potentielle pourrait se produire pour éviter les pénétrations osseuses. Ainsi, des *détections de collision* sont effectuées entre les os et les réponses à ces collisions sont ensuite calculées pour atteindre l'état de non-pénétration (ce qui permet de déplacer le centre de rotation de la hanche au cours du mouvement).

Cette méthode de correction a l'avantage de fonctionner en temps réel et est applicable à d'autres articulations. La validation de cette méthode est obtenue avec des données recueillies à l'aide d'un protocole d'IRM dynamique.

Avant de convertir les trajectoires des marqueurs en animation, notre travail se porte sur un autre problème classique en analyse de mouvement : les positions des marqueurs par rapport aux os sont inconnues. Une calibration est donc nécessaire afin d'établir une correspondance entre l'anatomie et le mouvement. Cette procédure est appelée *calibration anatomique*. Dans la plupart des études cinématiques, les positions des segments et leurs orientations par rapport au cluster de marqueurs sont établies à partir de la calibration d'un certain nombre de repères anatomiques, externes et palpables [CCCL95]. Le mauvais placement de ces repères est une source d'erreur qui affecte la détermination de la position de l'os, et de ce fait, l'estimation et l'interprétation de la cinématique articulaire [CLCC05]. Pour réaliser cette calibration, notre idée est de combiner IRM et body scanner 3D afin d'obtenir une meilleure approximation grâce à la position des marqueurs sur la peau.

La deuxième étape est la phase expérimentale et analytique. Celle-ci consiste à étudier le mouvement des hanches des danseuses professionnelles de ballet, puisqu'elles sont soumises à de fortes amplitudes de mouvement pendant leurs activités quotidiennes. Des conflits fémoroacetabulaires et/ ou des subluxations pourraient être des causes potentielles de développement d'arthrose de hanche chez cette population avec des stigmates potentielles chez les danseuses symptomatiques. Dans ce travail, ces hypothèses sont évaluées grâce à :

- L'analyse de mesures morphologiques standards (ex : mesure de l'angle alpha, de la profondeur de l'acétabulum, de la version acétabulaire) qui sont généralement utilisées pour diagnostiquer les conflits fémoroacetabulaires. Dans ce but, un ensemble d'outils de mesure est mis en place pour évaluer la normalité de l'articulation de la hanche du sujet en améliorant la lecture (subjective) des images radiologiques.
- La quantification des translations fémoroacetabulaires pour déterminer la présence de subluxation, en se basant sur la troisième composante de notre méthode de correction d'artefacts de peau.

- La détection de la région des conflits fémoroacetabulaires en utilisant des méthodes de détection de collision et en mesurant la compression des cartilages par des méthodes de calcul de pénétration (des simulations basées sur la physique pourraient être aussi intégrées afin de visualiser la déformation des cartilages et calculer la pression à l'intérieur de l'articulation).

Les résultats de nos simulations sont ensuite comparés à l'étude clinique (analyse radiologique et examen clinique). Si nous pouvons comprendre la relation entre la morphologie et la cinématique, nous serons en mesure de déterminer si certaines morphologies sont mieux adaptées aux activités pratiquées par les danseurs. Finalement, pour mettre en œuvre et tester nos contributions, toutes nos données d'acquisition et nos méthodes sont intégrées dans une plateforme clinique dirigée par une ontologie médicale. L'objectif est de fournir aux orthopédistes une visualisation et une simulation interactive de la hanche pour son examen clinique.

Résultats

Nous démontrons l'efficacité des méthodes proposées [MTCS08] [CLMT08] [CAVMT09] [CSKC+09] par rapport aux techniques précédentes dans les aspects suivants :

- **Précision :** à travers une validation adéquate, nous montrons que la précision de nos méthodes est de l'ordre du millimètre. Grâce au body scanner 3D et à l'utilisation de modèles 3D, la calibration anatomique est plus précise. Contrairement aux techniques précédentes qui appliquent de fortes contraintes cinématiques, notre algorithme d'estimation du mouvement permet des translations au niveau de l'articulation, ce qui apporte une simulation plus valable d'un point de vue physiologique.

- **Robustesse :** notre algorithme d'estimation du mouvement est capable de gérer de larges et diverses amplitudes de mouvement, ainsi que de gérer la variabilité inter-patient.

- **Automatisation :** à partir de peu de paramètres de l'utilisateur (un fichier standard de trajectoires de marqueurs), notre algorithme d'estimation du mouvement est en mesure de calculer directement la cinématique de la hanche du sujet. En outre, en exploitant les caractéristiques géométriques des modèles 3D, notre méthode de calibration anatomique est quasi automatique.

- **Faisabilité clinique :** par rapport aux techniques précédentes qui sont coûteuses en temps en raison des acquisitions de données supplémentaires et requises, notre protocole de mouvement est plus faisable cliniquement, car il ne nécessite qu'une seule et unique acquisition de données supplémentaire (un body scan 3D de 15 secondes de la surface corporelle du sujet).

- **Vitesse de calcul :** notre algorithme d'estimation du mouvement permet une visualisation et une interaction avec les données en temps réel, ce qui facilite l'analyse de systèmes humains complexes.

- **Flexibilité :** les méthodes proposées sont génériques et ne sont pas limitées à une articulation spécifique.

Grâce à l'étude des danseuses, nous mettons également en avant les constatations cliniques suivantes [CKCD$^+$09] [DMKC$^+$09] [CKCD$^+$10a] [CKCD$^+$10b] [DKCC$^+$10] :

- Chez les jeunes adultes, l'arthrose précoce n'est pas seulement le résultat de conflits fémoroacetabulaires. Les mouvements répétitifs extrêmes pourraient aussi affecter le développement précoce de l'arthrose de la hanche.

- Une pratique prolongée de la danse pourrait exposer la hanche morphologiquement "normale" à des conflits fémoroacetabulaires récurrents en position supérieure ou postérosupérieure et à des subluxations de l'articulation.

- Certains mouvements de danse semblent être arthrogènes : développé à la seconde, grand écart facial, grand écart latéral et grand plié. Ces mouvements devraient donc être limités en fréquence.

- Aucune morphologie spécifique semble être nécessaire pour la danse. Les amplitutes extrêmes de mouvement sont possibles grâce à un entraînement intensif et régulier. Elles sont le résultat d'une combinaison de trois mouvements articulaires.

Limitations et perspectives

Malgré les avancées attribuables aux méthodes que nous présentons, il y a un certain nombre de limitations. L'expérience acquise au cours de cette thèse nous permet de mettre en évidence certains aspects et problèmes qui devront recevoir une attention particulière dans des travaux futurs. Plus de travail est également requis en terme de test et validation.

- **Calibration anatomique :** l'automatisation et la flexibilité en terme de traitement et de géométrie, respectivement, sont deux aspects qui pourraient être encore plus performant concernant notre méthode de calibration. En effet, l'identification de la position des marqueurs sur le scan pourrait être accélérée en utilisant des méthodes de partionnement du corps et des techniques de détection automatique. Notre méthode de calibration est basée sur l'utilisation

de modèles génériques. Pour accroître sa flexibilité, il serait aussi opportun de développer un algorithme plus complet et indépendant de la géométrie des modèles.

- **Algorithme d'estimation du mouvement :** il existe une extension possible. Au lieu de corriger le centre de rotation de la hanche lorsqu'un contact anormal survient entre l'os de la hanche et le fémur, nous pourrions introduire des contraintes dérivées de la mécanique des milieux continus. L'idée serait d'intégrer des forces (charges) afin de trouver l'équilibre dans l'articulation, et par conséquent avoir une approximation plus exacte du centre de rotation de la hanche. Toutefois, ces forces doivent être disponibles, ce qui peut être difficile à mesurer en fonction du mouvement (ex : mouvements de danse).

- **Détection des conflits fémoroacetabulaires :** nous nous sommes concentrés sur l'interprétation géométrique du contact entre les tissus articulaires. Nous pensons que notre simulation pourrait bénéficier de l'utilisation de modèles biomécaniques en tenant compte des propriétés mécaniques des tissus mous et osseux, et ainsi contribuer à une meilleure compréhension de la pathologie.

- **Validation :** en raison de la difficulté à mesurer (ex : pas d'accès à la cinématique des os) et de la complexité du système musculo-squelettique, les modèles fonctionnels sont difficiles à valider. Des tests approfondis et des collectes de données sont obligatoires, ce qui n'a pas pu être exhaustivement réalisé pendant cette thèse. Nous recommandons donc des tests de validation supplémentaires.

Contents

List of Figures

List of Tables

Chapter 1

Introduction

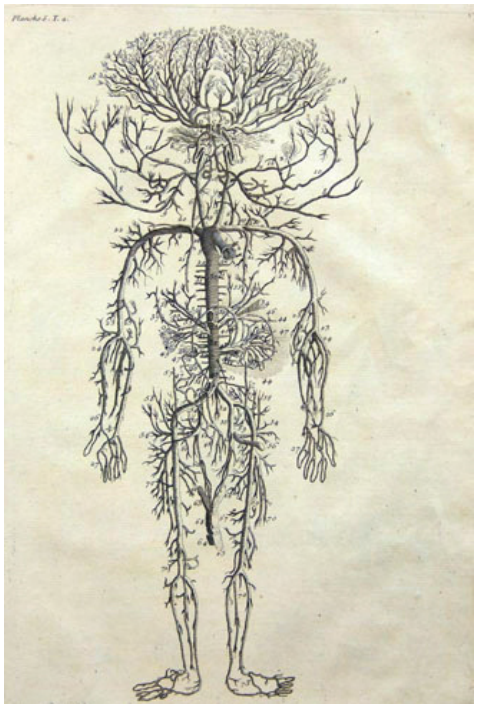

[1] James Robert, 1705-1776. Dictionnaire universel de médecine, de chirurgie, de chimie, de botanique, d'anatomie, de pharmacie, d'histoire naturelle, etc. Précédé d'un discours historique sur l'origine & les progrès de la médecine, Paris: chez Briasson, 1746-1748. Collection Léo-Pariseau. Bibliothèque des livres rares et collections spéciales, Université de Montréal. Image from `http://www.bib.umontreal.ca/CS/livre-savant/renaissances/fiches/encarteres.htm` used by permission.

1.1 Research context

MIRALab at the University of Geneva has a long history of innovations in the field of medical simulation [KBG+95] [BGK+96] [MWMTT98] [YCGMMT04] [KSMT05] [GMMT06]. At the beginning, efforts were primarily direct towards modeling and visualization of 3D generic models of human organ extracted from Computed Tomography (CT). After years of development at MIRALab, clinicians can now obtain a complete 3D view of the hip joint, including bones and soft tissues, reconstructed from innovative segmentation algorithms based on Magnetic Resonance Imaging (MRI) [Gil07], which is not invasive compared to CT. Moreover, the process is almost automatic and the 3D models are patient-specific.

Since most of the pathological cases relate to the joint kinematics (functional level), static 3D models are not sufficient to diagnose abnormalities and to understand the articular physiology. Therefore, substantial research was also conducted at MIRALab in the use of non-invasive techniques to quantify joint kinematics *in vivo* and *in silico*. Information from optical motion capture, MRI and computer was combined. First, methods were proposed to locate the hip joint center (HJC) and to assess the range of motion of the hip joint [Kan05]. This information is important for the surgical planning. However, only patients with a normal range of motion (people not assuming extreme positions such as the dancers for example) were studied. Hence, the behavior of the hip joint while performing extreme postures is still unknown. Second, another work combining dynamic MRI and optical motion capture was carried out [YC06]. The dynamic MRI was used to quantify the markers displacements and to develop a correction algorithm in order to reduce the errors of skin artifact in optical systems. Despite an interesting approach, this method used a virtual skeleton to derive the joints kinematics when using the optical system. This methodology was thus not subject-specific, was simplified in terms of joint structures and was prone to error during the skeleton calibration (error $\approx 2cm$ per segment), which is not accurate for medical applications. Therefore, further research is needed in this area.

Nowadays, a strong focus is being put in the physically-based simulation. Indeed, the analysis of the stress and contact distribution in soft tissues contributes to the understanding of hip biomechanics (e.g., mass-spring [MSBT05] [SMBT05] and Finite-Element method [CBF06] [CBF08]). However, these techniques do not generally simulate complex geometrical 3D meshes (for instance patient-specific models) during sophisticated movements. The movement is typically simplified to simple anatomical angles or to low amplitude motion. Nevertheless, it is crucial to simulate both the real patient's anatomy and kinematics, since large anatomical variations exist among individuals and that all people move differently.

The work presented in this dissertation has been done in the framework of CO-ME (Computer Aided and Image Guided Medical Interventions)[1]. CO-ME is a Swiss National Foundation project, the global objective being "*to develop an interactive clinical visualization for the hip joint examination*". Our contributions to this project within this research context are 1) to provide the required motion input for the simulation, where skin artifacts are effectively reduced and 2) to study the hip joint in extreme and complex postures.

1.2 Motivations

Musculoskeletal disorders (MSDs) are injuries of either muscles, nerves, tendons, ligaments, joints, cartilage, or spinal discs. Most MSDs are not typically the result of an instantaneous or acute event (e.g., a slip, trip, or fall), but reflect a more gradual or chronic development. MSDs include problems such as back pain, joint diseases, osteoporosis and limb trauma due to accidents. Within the framework of this research, a special focus is put in the search of early signs of hip osteoarthritis (OA) and their subsequent treatment. The typical patient with OA is middle-aged or elderly. As ageing of population is growing at a rapid pace, a better knowledge of the pathogenesis is critical. Most often, the patient will suffer pain and stiffness in and around the hip joint, along with some limitation of function and mobility (Table 1.1) [ML00].

Symptoms	**Signs**
Joint pain	Bony enlargement at affected joints
Morning stiffness lasting less than 30 minutes	Limitation of range of motion
Joint instability or buckling	Crepitus on motion
Loss of function	Pain with motion
	Malalignment and/ or joint deformity

Table 1.1: Clinical features of osteoarthritis. Reproduced from [ML00] used by permission.

OA of the hip could be caused by femoroacetabular impingements (FAI) which occur when there is an abnormal contact between the proximal femur and the acetabular rim. Generally, two basic types of impingement can be distinguished (Figure 1.1): 1) the cam FAI caused by a non-spherical femoral head at the femoral head-neck junction [InL$^+$01] [LPB$^+$04] [BKG05] [PMD$^+$06] [TGB$^+$08] and 2) the pincer FAI due to acetabular overcoverage [GPB$^+$03] [LPB$^+$04] [BKG05] [PMD$^+$06] [TGB$^+$08] or acetabular retroversion [RLK99]. These morphological abnormalities induce degenerative lesions of the cartilages and the superior labrum [PMD$^+$06] [TGB$^+$08] [LeG09]. In severe arthritic conditions, and when no improvement with medication is noted, surgical treatments and more commonly, total

[1] `http://www.co-me.ch/`, accessed November 2009

hip replacement is performed. For further information about hip OA, a more detailed description is given in Appendix B.

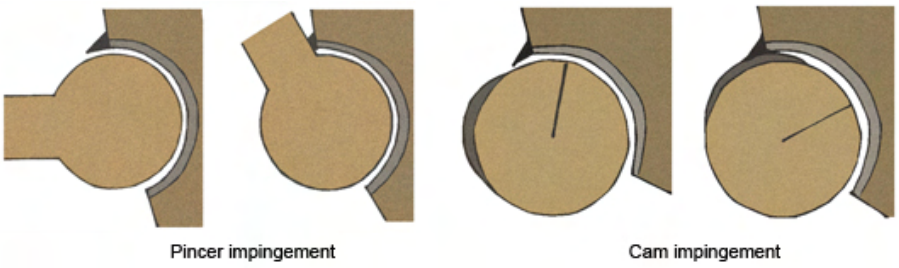

Figure 1.1: Excessive overcoverage of the femoral head by acetabulum in pincer FAI (left), causing abutment against the acetabular rim. Reduced head-neck offset of cam FAI (right): non-spherical head abuts the acetabular rim.

The FAI mechanism also seems to be one of the leading causes of the development of early arthritis in young adults practicing repetitive and extreme movements (e.g., dancers, gymnasts, etc.). Indeed, changes in the movement and alignment of the hip lead to excessive wear and tear on the joint surfaces [Mas01] [Bin03] [LS06]. Recurrent lateral (external) rotation [Mas01] [MNS$^+$01] [MNA$^+$03] [Bin03] [CKH$^+$09] [GH09] or hyperabduction [NV00] [GH09] of the hip also seem to be a critical factor of labral microtrauma. Nevertheless, the arthrogenous movements have not yet been clearly identified. Furthermore, the range of motion of the hip joint of people assuming extreme positions has not yet been determined. It is also unclear whether the femoral head and acetabulum are congruent (Figure 1.2) in extreme positions (e.g., split position). Joint congruency could be another potential cause of early OA, inducing a high-stress on the labrum. Therefore, the purpose of this PhD work is to verify if repetitive extreme movements can be a factor of hip joint degeneration through joint subluxation and excessive labral deformations. This work aims at investigating methods to identify arthrogenous activities, visualize/ locate femoroacetabular conflicts, and prospectively quantify the range of motion and congruence of the hip joint in extreme postures.

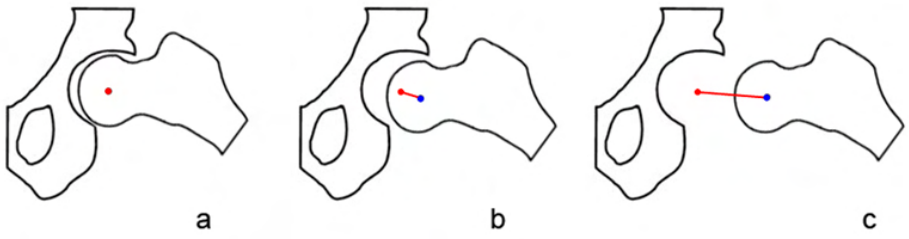

Figure 1.2: Types of alignment of femoral head to acetabular socket: a) normal b) subluxation c) luxation.

To achieve these goals, the motion of the hip joint must be accurately reproduced. To this end, our methodology addresses one main issue: we developed a protocol for joint motion estimation using optical systems, allowing the recording of a large range of motion. Comparing to other devices (see Section 2.2), the optical systems are not invasive, but the internal bone remains inaccessible. Skin deformation and displacement (due to the muscle activity) cause marker movement with respect to the underlying bone (Figure 1.3). This movement represents an artifact which affects the estimation of the skeletal system kinematics and is considered as the most critical source of error in human motion analysis [LCCC05]. Several methods were proposed to reduce these errors (see Section 2.4), but these techniques suffer from the following limitations:

- Mathematical approaches, such as the Point Cluster Technique [AA01], are unstable and do not perform better than traditional bone pose estimators (e.g., Single Value Decomposition algorithm [SB93]). These approaches are thus not efficient to compensate skin artifacts.
- Methods, such as the Multiple anatomical landmark calibration [CSFL05], are based on invalid assumptions (e.g., assuming that the skin motion during a static posture is the same as during the dynamic activities).
- Techniques, such as the Global optimization [LO99], are limited to the use of ball and socket joints (i.e., meaning that no shifts are allowed), which simplifies the joint structures and is not subject-specific.

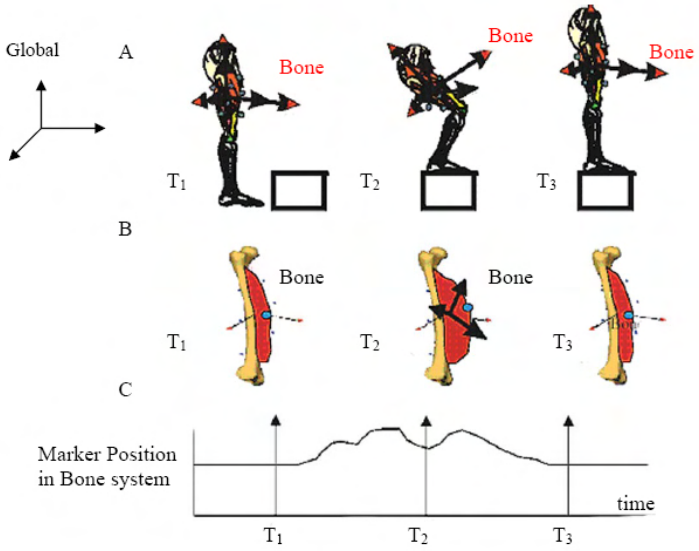

Figure 1.3: The trajectory of an individual marker during a step-up activity. In T2, the marker is displaced in the bone system as the muscle contracts. Image from [AA01] used by permission.

Consequently, correcting skin artifacts is still being investigated, and this is the domain where this work lies in. In this thesis, we propose to extend pre-existing works with a correction method which combines nonlinear optimization and joint motion constraints, and allows some shifts at the joint. Details on our contributions are given in the next section.

Once the motion of the hip joint is precisely estimated, experiments can be carried out. This work includes a case study of the hip motion in professional ballet dancers, a population who is at high-risk of developing OA [Mas01] [Bin03] [LS06] [GH09]. Indeed, characteristic chondrolabral lesions are diagnosed at a very young age in this population (e.g., at the age of 18-25 years old). The following questions are stated:

- Is the OA only the result of cam/ pincer -FAI (i.e., abnormal morphologies)?
- Or, is the OA a consequence of the dancers' activities (i.e., repetitive extreme movements, subluxation)?
- Or, is it the patient's morphology that is not adapted to the movement?
- Who are the patients at risk?
- What are the morphologies at risk?

To answer these questions, we propose to investigate several methods, including morphological measurements (e.g., femoral alpha neck angle, acetabular depth, acetabular version), joint congruency quantification and FAI region detection (e.g., by detecting the collisions between the joint tissues). The recording and studying of professional ballet dancers' hips undergoing extreme postures provide us with an extreme kinematical model of the hip articulation.

1.3 Objectives and contributions

As mentioned in Section 1.2, the fundamental goals of this study are:

- Identification of arthrogenous movements through the hip motion study of professional ballet dancers.
- Visualization and localization of potential FAI, and quantification of the range of motion and congruence of the hip joint in extreme postures.
- Understanding, for hip OA the relation between morphology and kinematics, with reference to recorded data.

- Early diagnosis of hip OA, by supporting orthopedists with reliable tools.

To pursue these objectives, our research is realized in two steps:
First, we set up a motion protocol for estimating bone poses of patient-specific hip joint using an optical motion capture system. To overcome the issue of skin deformation, we propose a correction method based on three components:

- A least-squares minimization for optimizing joint center locations and segment orientations. Due to the non-linear movements of skin markers [CCL93], we use a *sequential quadratic programming algorithm* [LT01] for robustness and fast convergence.

- It was observed [KASS94] that soft tissue artifacts can induce non-physiological joint translation or even dislocation. Hence, *joint constraints* are applied to avoid these unwanted effects.

- Although the HJC can be considered to be fixed during low amplitude movements, this is no longer true for extreme motion [GKCMT$^+$09]. Indeed, a potential subluxation may occur to avoid bone-to-bone penetration. Thus, *collision detections* are performed among the articulating bones and their collision responses are computed to reach the non-penetrating state (i.e., allowing the HJC to slightly shift during movement).

This correction method has the advantage of being fully real-time and applicable to other joints. The validation of the hip kinematics estimation is obtained with marker position data collected from a dynamic MRI protocol. Such acquisitions can provide reliable rigid bone frames, hence the possibility of comparing frame reconstruction techniques, making reference to actual bone data.

Before converting markers trajectories into animation, our work examines another critical issue in human movement analysis: the position of the skin markers with respect to the underlying bone is unknown. A calibration is thus required to establish a correspondence between anatomical and motion frames. This procedure is called *anatomical calibration*. In most kinematic studies, bone segment locations and orientations in the marker cluster technical frames (i.e., the frame determined using marker point coordinates) are established from a number of calibrated, external, palpable anatomical landmarks [CCCL95]. Misplacement of these landmarks is a source of error that affects the determination of anatomical bone-embedded frames and, consequently, the estimation and interpretation of joint kinematics [CLCC05]. To establish the required calibration, our idea is to combine MRI and 3D body scan information to have a better approximation thanks to markers positions on the skin.

The second step is the experimental and analytical phase. The latter consists in studying the motion of professional ballet dancers' hips, since they are subject to extreme ranges of motion during their daily activities. FAI and/ or subluxation could be a potential cause for the development of hip OA in this selected population with potential stigmata of FAI and/ or subluxation in the symptomatic dancers. In this work, these hypotheses are evaluated through:

- The analysis of standard morphological measurements (e.g., femoral alpha neck angle, acetabular depth, acetabular version) that are typically used to diagnose cam/ pincer -FAI. For this purpose, a set of measurement tools are implemented to evaluate the normality of the subject's hip joint, improving the (subjective) reading of medical images.
- The quantification of femoroacetabular translations to access if any joint subluxation occurs, based on the third component of our skin artifacts correction method.
- The detection of the FAI region using collision detection methods and the measure of the cartilages compression using penetration depth methods (physically-based simulations could be also integrated to visualize the cartilages deformation and to compute the contact pressure).

The simulation results are then compared with the clinical study (i.e., the radiological analysis and the clinical examination). If we can understand the relation between morphology and kinematics, we will be able to determine if some morphologies are better adapted to the activities practiced by the dancers. Finally, to implement and test our contributions, all the acquisition's data and processing methods are integrated into a semantic-driven clinical platform. The goal is to provide orthopedists with an interactive visualization/ simulation framework of the individualized hip joint examination.

1.4 Outline

The present manuscript is organized as follows: the first chapter is dedicated to the existing work and broadly reviews the field. Chapter 2 provides a literature review of existing human motion capture devices and human motion analysis techniques. A complete survey of the methodologies used to estimate the human joint kinematics, including both invasive and non-invasive methods is given. State of the art methods for quantifying and reducing soft tissue artifacts are presented and discussed. The three remaining chapters deal with our work: Chapter 3 is dedicated to the hip anatomy and the theory related to the kinematic study of the hip joint. Theoretical foundations of human joint motion are presented and discussed with a special focus on methods adopted in this thesis. In Chapter 4, our approach for estimating the hip joint kinematics and our skin artifacts correction method are exposed.

The methodology is based on a non-invasive system, namely optical motion capture. The use of the 3D body scanner in combination with MR imaging is also described in this chapter. The study of dancers and the results of our proposed contributions are detailed in Chapter 5. We finally conclude with our achievements and perspectives in Chapter 6, followed by Annexes with detailed technical aspects.

Chapter 2

Related work

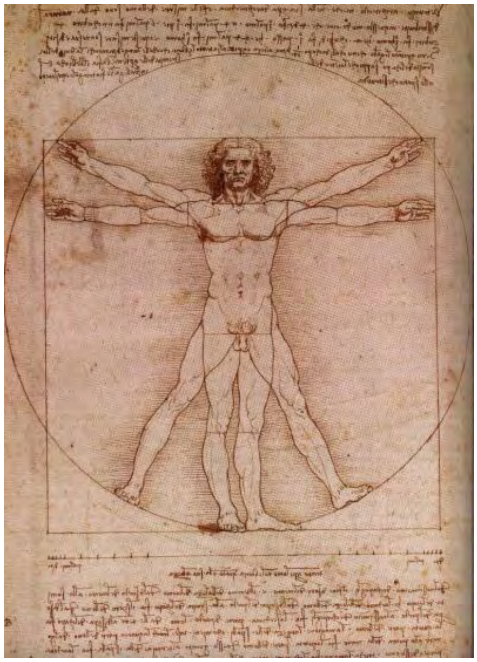

[1]Leonardo da Vinci, 1452-1519. Etude de proportions du corps humain selon Vitruve. Dessin à la plume. Gallerie dell'Accademia, Venise, 1822.

2.1 Introduction

The biomechanics community started to investigate how to estimate human joint kinematics early on [LIB48], first by using invasive motion recording techniques (e.g., intra-cortical pins, external fixators). Due to the health risks related to the invasiveness of these devices and with the development of the stereophotogrammetry, the utilization of the latter technique flourished. Unfortunately, the community had to face an important problem: the soft tissue artifact (STA), which is regarded as the most critical source of error in human motion analysis [LCCC05] [Cro06]. Therefore, numerous studies were conducted to quantify STA *in vivo*. At the same time, researchers concentrated their efforts on devising methods for the compensation and reduction of its effect.

In this chapter, existing techniques and current knowledge for estimating and analyzing human joint motion are presented. We first describe and compare the various instrumentation techniques with emphasis on their strength and weakness. Then, the inherent problem of STA related to skin-based instrumentation is discussed. To understand this problem, we present the most important studies that describe and report the patterns and magnitudes of STA. Finally, state of the art methods for reducing these errors are introduced and discussed, and are divided into two categories: those analyzing skin surface motion and deformation, and those including joint motion constraints. The main purpose of this chapter is to identify the most critical issues and retrieve existing solutions from the literature with their respective advantages and limitations.

2.2 Instrumentation for 3D motion recording

Instrumentation, medical imaging and more recently computer technologies have provided new opportunities for the advancement of the human locomotion study. In the following, we provide an overview of different techniques for skeletal movement measurement and we report the most significant works using those devices. They are classified into bone-based techniques (e.g., intra-cortical pins) and skin-based techniques (e.g., motion capture). Bone-based techniques involve the implantation of pins directly into the bone or the detection of bony landmarks on medical images, while skin-based techniques entail the use of reflective markers or small measurement devices on the skin surface. Tracking systems are then commonly used to record the position of the pins/ landmarks/ markers in 3D.

2.2.1 Bone-based techniques

Intra-cortical pins - a few pioneering studies [LIB48] [Laf84] were conducted using intra-cortical pins to analyze skeletal motion while walking. In 1948, Levens et al. [LIB48] implanted twenty-six

normal subjects with stainless-steel threaded pins of $2.5mm$ of diameter into the iliac crest of the pelvis, in the adductor tubercle and in the tibial tubercle. Targets, each consisting of a light wooden rod with spheres attached at two points, were fastened to the pins. Walking patterns were studied with three cameras operating at 8 frames/s. The goal was to determine the magnitude of transverse (axial plane) rotations of segments of the lower extremity, and their relative transverse rotations with respect to each other. This study was considered as outstanding at this period, even though a complete description of the movements of the joint in 3D was not established (due to insufficient development of close-range photogrammetry techniques at this time).

Figure 2.1: View of one subject with the triad targets attached to the tibial, femoral and patellar pins. Image from [LCS$^+$94] used by permission.

Two later studies by Lafortune et al. [LCSK92] [LCS$^+$94], which used target clusters directly fixed into the bones, reported actual tibio-femoral 3D kinematics during walking. Intra-cortical pins were inserted into the tibia, the femur and the mid-patella (Figure 2.1) of five healthy subjects, and target clusters mounted onto the pins were filmed by four cameras. Radiographs of the lower limb were obtained to compute the anatomical bone reference frames (i.e., the relative position of the target clusters in relation to internal anatomical structures). Later on, numerous studies [KL94] [RvdBL$^+$97b] [RvdBL$^+$97a] [FLMM97] [YHC$^+$00] [WHH$^+$00] [HYC04] [BRL$^+$06] [NJL$^+$07] [vdBRL08] [LNL$^+$08] [WLJ$^+$08] were carried out in a similar way to assess joint kinematics and/ or STA. To quantify the

skin deformation, a combination of skin markers and intra-cortical pins were recorded during walking, running or hip internal-external rotation. It was concluded that the use of skin markers to represent motion of the underlying bones was problematic, particularly for the thigh.

External fixators - another set of studies was performed using external fixators. Experiments were carried out on patients treated for a femur or tibia fracture with unilateral external fixation devices. These devices consist of wires, pins and rods fixed to the bone (Figure 2.2). Through adequate marker mounting, a set of axes rigidly associated with the underlying bone was defined. Segment positioning and orientation can then be computed from recorded markers motion. This approach was primarily used in studies conducted to estimate STA [ACCL92] [ACCL93] [CCL$^+$96]. Despite an accurate bone-representation with such devices, this technique is limited by the fact that the concerned patient is recovering from a leg fracture and therefore does not reveal natural gait pattern. In addition, the study is restricted to a single bone, as no subjects are simultaneously instrumented with fixators on multiple segments.

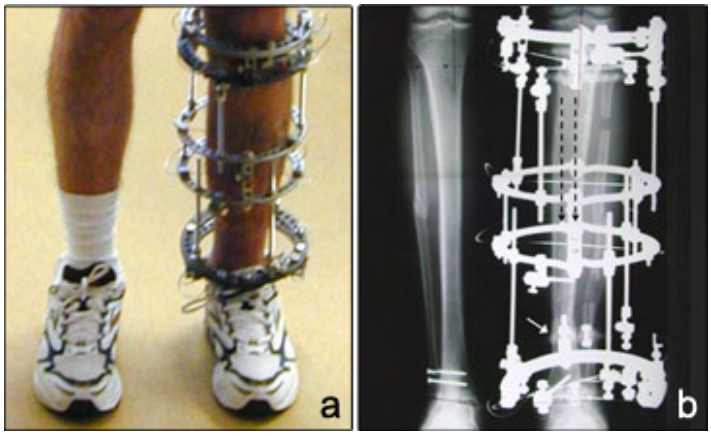

Figure 2.2: a) An Ilizarov fixator, commonly used in the stabilization of bone fracture b) The corresponding X-ray image. Image from [web] used by permission.

Percutaneous trackers - percutaneous trackers are metal devices rigidly attached to bony segments by using a number of halo pins inserted into soft tissues and bone (to a maximum depth of $4mm$) on opposite sides, instrumented with a rigid array of four retroreflective markers (Figure 2.3). In [HOS$^+$97] [MMS$^+$00] [MMR$^+$02], different aspects of STA are investigated by combining the use of skin markers and percutaneous trackers during walking. Similarly to the external fixators, drawbacks are associated with the evident joint motion restrictions and the encumbrance of such devices.

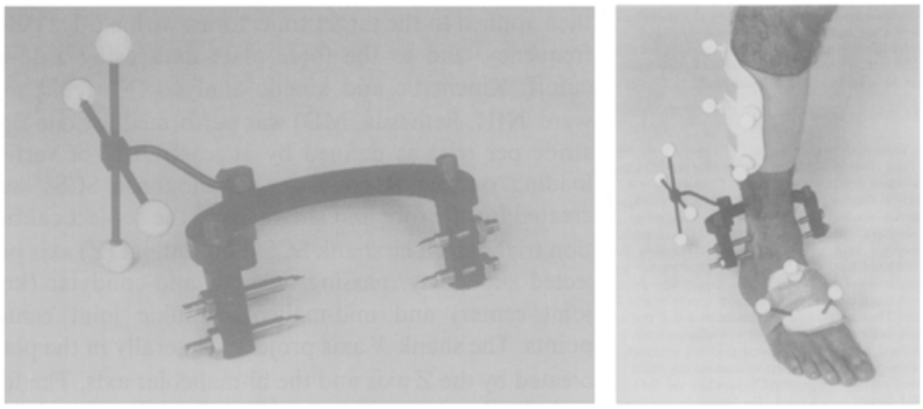

Figure 2.3: Percutaneous tracker including the four halo pins used to mount the device and the four retroreflective targets. Image from [HOS+97] used by permission.

Medical imaging techniques - two synchronized radiographs are used to study bone poses using radiographic markers in two non-parallel planes. This approach is known as Röntgen stereophotogrammetric analysis (RSA) [Sel89] which makes use of conventional X-rays to capture images with large doses of radiation. To accurately measure bone motion in RSA radiographs, bony landmarks are not sufficiently distinctive. In order to obtain well-defined measurement points, tantalum beads are inserted into the bone (Figure 2.4). These beads have a diameter of 0.5, 0.8, or $1mm$. Due to their small size and spherical shape, their projection are not influenced by changes in patient position or Röntgen focus position. Therefore, the position of these markers can be measured with great accuracy (between 0.05 and $0.5mm$ for translations and between 0.15° and 1.15° for rotations) [VNRR02]. However, the use of RSA is restricted to quasi-static movements, because the examination of movements requires multiple static exposures at different joint angles. This method was used in several studies for estimating joint kinematics [ES86], prosthetic fixation [VNRR02] [GJGMSM04], vertebral motions, etc.

Fluoroscopy is another medical imaging modality for the study of human motion. This technique allows the acquisition of X-ray images of motion on video, reducing significantly radiation exposure. 3D positions and orientations of bones are estimated from bony landmarks at each frame with an accuracy of $1mm$ in position. For example, this system was used to analyze the knee kinematics [BH96] [BMH97] [FRB05] [ZGS+06] [LTK+08], the shoulder motion [PHS+02] or to assess STA [SdGLK96] [TA02] [FSC+02] [SFC+02] [GKM+07].

Another imaging modality, which is becoming more and more common for skeletal measurement, is the

MRI. This modality is not invasive (i.e., no ionizing radiation) and motion can be acquired in real-time [GPMTV04] (Figure 2.5). Recent studies have been conducted for STA assessment [YCGMMT04] [YCMMT04] [MB06] [YCMT06] [SMC+06].

Figure 2.4: RSA of a prosthetic knee: a) markers positioning b) the corresponding X-ray image. Image from [VNRR02] used by permission.

Imaging techniques are accurate. However, it should be noted that the confined area of measurement limits the movement possibilities of the subject. Furthermore, extensive image data processing is required and the analysis is restricted, since only a single joint can be measured at the same time.

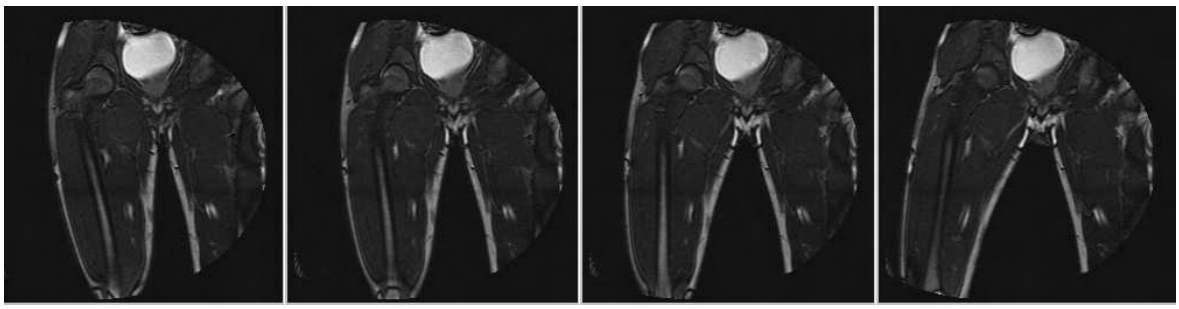

Figure 2.5: Real-time dynamic MRI of the thigh. Image from [GPMTV04] used by permission.

2.2.2 Skin-based techniques

In comparison to other kinematics acquisitions, skin-based techniques offer a larger field of view and range of motion. Such systems are not invasive and provide fast tracking. However, limitations lie

in the lack of accuracy, since only the skin deformation is measured and no direct access to bones is available.

Motion Capture (MoCap) - the MoCap records landmarks attached to the skin. The latter are usually positioned on the articulations, as these are strategic points of interest needed to recreate the subject's movement. In a post-processing phase, landmark positions are reconstructed in 3D, and rigid motions of body segments are evaluated through the landmark trajectories. Three main techniques can be distinguished [Men00] (Figure 2.6):

- *The magnetic system*: it is based on the measurement of a magnetic field generated by a transmitter source with the use of sensors placed on the body (e.g., MotionStar from Ascension Technology Corporation[1]). Sensors are never occluded and these systems do not require any special lighting conditions, but may be confused when metallic objects are present in the environment (i.e., it disturbs the magnetic sensor measurements). The low precision (typically $0.5deg/2mm$) and the encumbrance of cables are the main drawbacks.

- *The mechanical system*: this system directly tracks body joint angles and is often referred to an exoskeleton motion capture system, due to the way the sensors are attached to the body (e.g., ShapeWrap from Measurand[2]). Mechanical motion capture systems are real-time, relatively low-cost, free-of-occlusion and wireless with an unlimited capture volume. Limitations of the system, with regard to optical ones, are the relatively low sampling rate and accuracy (e.g., $90Hz$ and $0.5deg/2mm$ for ShapeWrap).

- *The optical system*: this is the most used technique (e.g., Vicon Motion Systems Ltd[3]). It involves tracking reflective markers (small spheres) with infrared cameras (sampling rate ranges from $30Hz$ to $1000Hz$). The motion reconstruction is accurate ($\sim 0.5mm$), but can be affected by occlusions, resulting in broken trajectories. This occurs when a marker is not seen by at least 2 cameras. To overcome this issue, the capture volume can be adjusted and cameras can be added at will.

MoCap systems can be also combined with electromyography (EMG) and forces plates for assessing musculoskeletal dynamics. These systems were used in several clinical applications including gait analysis and rehabilitation [DBD+04] [SdQD+07] [SBL08] [YOES08], biomechanical research, as well as computer-assisted medical research [YCGMMT04] [YCMMT04].

[1] `http://www.ascension-tech.com/`, accessed November 2009
[2] `http://www.measurand.com/`, accessed November 2009
[3] `http://www.vicon.com/`, accessed November 2009

Video-based systems - instead of MoCap, raw video images or laser scans can be used to assess musculoskeletal kinematics [MG01] [MCA06] [CMA06]. Some systems use passive markers; others use active markers, such as light emitting diodes or reflective prisms. With this technique, the reconstruction of human motion is based on the estimation and tracking of motion in image sequences using computer vision methods. Compared to MoCap, video-based systems have a lower accuracy and frame-rate. In [DHW+04], a dynamic body scanner system ($15Hz$) is used for spine dynamic analysis, where internal anatomical structures are estimated from the skin shape. Commercial products using stereophotogrammetry (e.g., 3dMd[1]) can achieve fast 3D surface imaging (e.g., $\sim 1.5ms$ for the face) of the patient's anatomy for healthcare applications (e.g., measurements, patient evaluation, treatment planning).

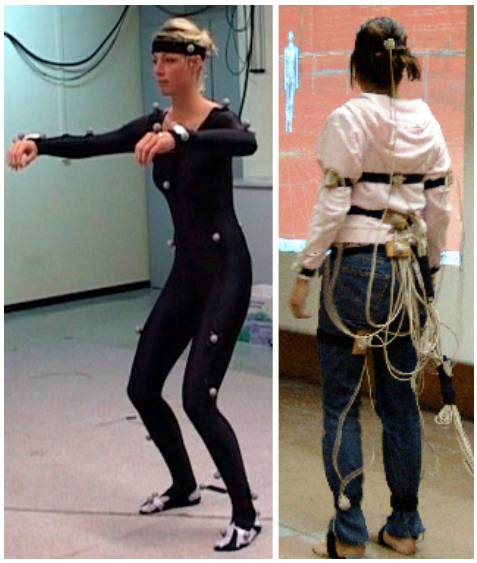

Figure 2.6: The two main motion capture systems: a) optical (Vicon) b) magnetic (Ascension).

Accelerometers and gyroscopes - a recent method to estimate joint kinematics makes use of accelerometers and gyroscopes. Such systems have the advantage of being ambulatory, allowing long term monitoring in the natural environment. In [DJA05] [DJC+06], they propose a minimal sensor configuration with one sensor module (each containing two accelerometers and one gyroscope) mounted on each bone segment. The model is based on estimation of the acceleration of the joint's center of rotation, by placing a pair of virtual sensors on adjacent segments at the rotation center (Figure 2.7). With this technique, joint angles are accurately found with small errors (shank: $RMS = 1.0°$, thigh: $RMS = 1.6°$), and shank and thigh segment orientations are thus estimated for gait analysis.

[1] `http://www.3dmd.com/`, accessed November 2009

In a later paper [FJAA08], this technique is extended to 3D measurements (the previous model was limited to 2D sagittal measurements). However, their current model requires efficient post-processing methods. Additionally, misalignment of the sensors or sensor deviation during movement can be a source of error.

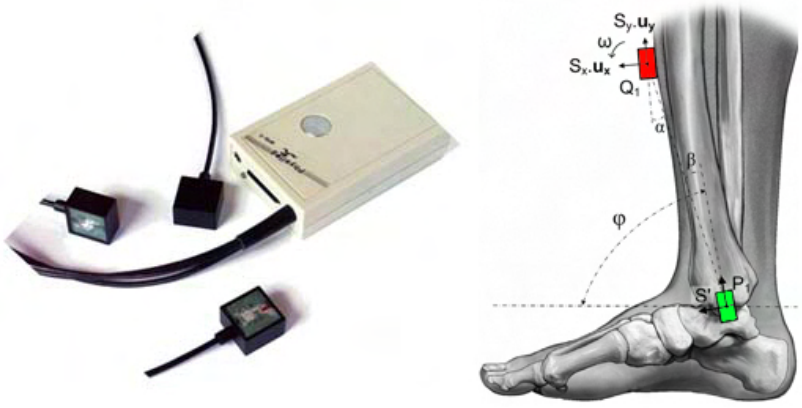

Figure 2.7: a) The Physilog system for recording sensors b) The position of the sensor on shank (red), and its corresponding virtual sensor on ankle (green). Image from [DJC+06] used by permission (©2006 IEEE).

2.2.3 Summary

Table 2.1 summarizes the advantages and drawbacks of the diverse measurement devices for estimating human joint motion. Methods with direct access to the bone are reliable and accurate, but their use is limited, because they are invasive (e.g., large dose of radiation, pins insertion into the bone) and impede natural motion patterns. They are hence not suitable for routine analysis and should be limited for ethical reasons. More recently, skin-based systems have been used. They aim at acquiring more global data in terms of range of motion and number of joints. These systems are not invasive, but do not reflect the exact bone motion due to soft tissue deformations. Since they are widely used by the biomechanics research community, methods to quantify and reduce these errors were investigated. We propose to discuss this issue in the next sections.

2.3 Soft tissue artifact assessment

Since our goal is to develop a correction method for minimizing STA, it is crucial to first understand the phenomena. Therefore, significant numbers of studies that describe patterns and magnitudes of

Method	Accuracy	Invasiveness	Computation complexity	Motion restrictions	Multiple joints evaluation
Intra-cortical pins	+	++	+	+	−
External fixators	+	++	+	+	−
Percutaneous trackers	+	+	+	+	−
RSA	++	++	++	+	− −
Fluoroscopy	++	+	++	+	− −
MRI	+		++	+	− −
MoCap	−		+		++
Video-based	−		++		++
Accelerators/ gyroscopes	−		++		+

Table 2.1: Instrumentation for 3D motion recording. Note: the accuracy is regarded in terms of bone pose estimation and not in terms of instrument's precision.

STA were reported. The most relevant works are described here, organized by techniques used, namely intra-cortical pins, external fixators, percutaneous trackers, Röntgen photogrammetry and MRI. In the following, a summary of results reported from the different studies is provided. From these results, some conclusions can be drawn. When developing a correction method, these conclusions should be taken into account, in order to increase the success of the correction.

2.3.1 Techniques based on intra-cortical pins

The use of intra-cortical pins is an accurate way to represent true bone motion. Nonetheless, sources of error exist: the pins can move in the bone, the marker cluster can move on the pin, the pin can bend and/ or the pins can vibrate. In the event of these occurrences, the subject is generally excluded

from the study.

In 1991, Lafortune and Lake [LL91] used X-ray radiography and intra-cortical pins to estimate knee STA. Three cycles of unloaded flexion/ extension of the knee were analyzed. It was showed that a skin marker fixed to the proximal tibia exhibited a distal displacement of $21mm$ and a posterior displacement of $23mm$, found to be linearly related to knee flexion. The STA magnitude was also reported at heel strike during running. The magnitude of the relative movement between a marker attached to a pin inserted into the tibia and a surface marker stuck over the lateral tibial condyle reached $10mm$.

Karlsson and Lundberg [KL94] compared the knee joint rotations measured with bone anchored and skin anchored markers, when performing hip internal-external rotation with extended knee. A range of 20° was observed with bone anchored markers, while a 50° range was measured with skin markers. The study concluded that the thigh STA was higher than the shank STA.

In two different studies, Reinschmidt et al. investigated both the knee and ankle joints for walking [RvdBL$^+$97b] and running activities [RvdBL$^+$97a]. Intra-cortical bone pins were inserted into the femur, tibia and calcaneus of five and three subjects, respectively. Marker triads were attached to these pins, and additionally six skin markers to the thigh, six to the shank, and three to the shoe. The results showed that the errors in knee rotations were mainly caused by the thigh markers and therefore suggested that external markers could only be used to reliably determine knee flexion/ extension. The skin movement errors were also higher in running than in walking.

Fuller et al. [FLMM97] assessed STA with two arrays of six markers each mounted on skeletal pins inserted into the tibial tubercle and the greater trochanter. Moreover, twenty skin markers were distributed all over the thigh and shank segments. Skin markers showed displacements of up to $20mm$ and STA was found to be task-dependent. It was also concluded that STA could not be removed with any filtering techniques, resulting in loss of information.

Westblad et al. [WHH$^+$00] instrumented three volunteers with Hoffmann pins inserted into the tibia, fibula, talus and calcaneus. Three markers were fixed laterally on each shank, heel, and forefoot to evaluate ankle kinematics. Data were collected during a barefoot walking trial. Their results showed that the mean maximal differences between the skin- and bone-based joint rotations were less than 5°. The smallest absolute difference was found for plantar/ dorsiflexion.

In a more recent study, Taylor et al. [TED+05] considered the relative error between skin and bone pin markers in a function of the soft tissue coverage for each segment, while comparing different methods to compensate STA. They concluded that current techniques were limited in their ability to determine the kinematics of underlying bones based on skin markers, particularly in segments with more pronounced soft tissue coverage.

Benoit et al. [BRL+06] assessed knee kinematics during gait and cutting motions. The kinematics derived from the bone pin markers were compared with that of the skin markers. Average rotational errors of up to 4.4° and 13.1° and translational errors of up to 13 and 16.1mm were noted for the walk and cut, respectively.

Finally, the foot STA was further quantified in [NJL+07] [WLJ+08]. Nester et al. [NJL+07] collected and compared three datasets describing foot kinematics from bone anchored markers, skin markers and plate-mounted markers. Data were acquired in three separate testing sessions and did not provide a clear answer as to whether a skin or plate-mounted markers protocol was preferable (i.e., no general under- or overestimation of bony rotations by surface markers registration was found). In [WLJ+08], tibio-calcaneal rotations during walking were investigated with both intra-cortical pins and surface markers monitored at the same time. The STA was more pronounced at the calcaneus with deviations of up to 4° in planar rotations.

2.3.2 Techniques based on external fixators

External fixators are typically used for patients with fractures for proper healing and were used to study STA. One limitation lies in the fact that the device and the fracture suffered by the subjects may have affected the normal skin movement, walking ability and normal muscle mass of the test subject.

Angeloni et al. [ACCL92] used external fixation devices and digital video fluoroscopy to estimate markers displacements on the femur and tibia. Markers were placed on the skin surface over four anatomical landmarks (ALs): greater trochanter (GT), lateral epicondyle (LE), head of the fibula (HF) and lateral malleolus (LM). Additional skin markers were placed on rigid plates attached to the proximal half of the thigh and the shank. It was concluded that skin-mounted markers are subjected to larger STA than the markers mounted on the rigid plates.

In a later paper, the same authors [CCL+96] reported more detailed results using the same technique. They examined five subjects and compared the measurements of bone positions and orientations be-

tween bone coordinate systems and coordinates systems, determined from skin-based marker systems. Several activities were analyzed: walking, cycling, flexion/ extension of the lower limb joints, hip rotation. They reported a maximum displacement of $40mm$ for a marker over the greater trochanter and $25mm$ for markers away from bony landmarks. The value of the STA associated with the markers located over the ALs was found to be related to the relevant joint angle, irrespective of the motor task performed.

2.3.3 Techniques based on percutaneous trackers

Another set of studies was carried out with percutaneous trackers. Holden et al. [HOS+97] examined three subjects during walking by tracking simultaneously the motion of surface markers at the mid-shank and a percutaneous tracker attached to the distal shank. Surface movement errors in shank kinematics estimates were determined by the relative 3D difference between the skeletal- and the surface-based anatomical frames. A maximum displacement of the origin of the shank coordinates system of $10.5mm$ in the longitudinal axis (Z) direction was reported. The greatest relative rotation occurred in the Z-axis of the shank with a magnitude of $8°$. The results were reproducible within, but not among, subjects.

Manal et al. [MMS+00] obtained similar results, while determining an optimal surface-tracking marker set for tracking motion of the tibia during walking. Eleven different marker sets were evaluated, obtained by combining geometry, location (proximal/ distal) and attachment (underwrap/ overwrap) factors for the array. Best estimates were realized for an underwrapped rigid shell with four markers physically constrained and located distally. However, even when using the best set of markers, rotational deviations of $\pm 2°$ about the medio-lateral and antero-posterior axes and $\pm 4°$ about the longitudinal axis were noted.

2.3.4 Techniques based on Röntgen photogrammetry

To investigate STA at the foot and ankle, Maslen and Ackland [MA94] studied ten subjects using 2D Röntgen photogrammetry during rear foot inversion/ eversion movements. Small steel markers were stuck over the two malleoli, the navicular tuberosity, the sustentaculum tali and the base of the fifth metatarsal. The two malleoli showed the largest artifact. Mean displacement between the skin markers and the underlying bones varied from 2.7 to $14.9mm$.

In an analogous study, Tranberg and Karlsson [TK98] evaluated six volunteers, while performing neutral, $20°$ of ankle dorsiflexion and $30°$ of ankle plantarflexion. Measurements were made with

spherical lead markers of $2mm$ diameter glued on the medial malleolus, the navicular bone, the medial part of calcaneus, the base and the head of the first metatarsal, and the base of the fifth metatarsal. The markers were found to move up to $4.3mm$, with the most proximal markers showing the largest displacement.

Fluoroscopy was first used by Sati et al. [SdGLK96] to examine knee STA. To track the skin movement, $3mm$ diameter stainless steel balls were individually taped onto the medial and lateral part of the distal thigh. Fluoroscopic images were collected during 65° of active knee flexion. Effects of image distortion and 3D femur movement were removed with a mathematical model. It was found that skin-bone movement varied significantly over both medial and lateral femoral condyles from 2 to $17mm$. In particular, the largest artifact was observed for markers located closest to the joint line.

Tibio-femoral kinematics were assessed during impact movement (one-legged forward hopping) using a biplanar radiographic system [TA02]. Two subjects were implanted with three $1.6mm$ tantalum beads in tibia and femur at the time of knee surgery. The peak-to-peak magnitude of the STA ranged from 5 to $31mm$, with the largest artifacts occurring in the proximal/ distal direction.

Quantification of STA at the knee was also performed by combining 3D fluoroscopy and stereophotogrammetry [SFCL05]. Data were collected with two subjects, treated by knee arthroplasty, during stair climbing, step up/ down, sit-to-stand/ stand-to-site, and extension against gravity. Nineteen skin markers were uniformly strapped on the thigh and ten on the lateral aspect of the shank. The reference 3D kinematics of the femur and tibia was reconstructed from fluoroscopy-based tracking of the relevant prosthesis components. The abduction/ adduction and internal-external rotation angles were the most affected by STA propagation, with root mean square (RMS) errors up to 192% and 117% of the corresponding range, respectively. The STA at the thigh was the largest and the magnitude was subject- and task-specific.

In a more recent study, Garling at al. [GKM$^+$07] compared two marker cluster fixation methods by using fluoroscopy of knee motion after total knee arthroplasty during a step-up task. The ten subjects were randomized into a plate-mounted marker group and a strap-mounted marker group. A 3D model fitting technique was used to reconstruct the *in vivo* 3D positions of the markers and the implants representing the bones. The strap-mounted group showed significant more translational errors than the plate-mounted group for both the shank (respectively, 3 ± 2.2 and $0\pm2.0mm$) and the thigh (2 ± 2.0 and $0\pm5.9mm$).

2.3.5 Techniques based on Magnetic Resonance Imaging

During the last decades, the field of MRI technique application has expanded from anatomical imaging to biomechanical kinematic analyses, including research in STA assessment. Yahia-Cherif et al. [YCGMMT04] [YCMMT04] used the MRI technique to determine an optimized skin markers configuration for hip joint motion. Nine reflective markers were injected with a contrast agent and distributed all over the thigh. The bones and the markers were tracked in dynamic MRI during clinical motion patterns (hip internal-external rotation, flexion/ extension, and abduction/ adduction). The trajectories of the visible markers were calculated from the images and their displacements were quantified. The optimized configuration was selected based on the criteria of markers displacements and was then used for recording external movements with an optical motion capture system.

In a later paper, the same authors [YCMT06] quantified and expressed thigh STA as function of hip anatomical angles. A statistical analysis of the estimated STA errors showed that the markers displacements in the Z-direction were correlated with hip internal-external rotation, while the displacements in Y-direction were correlated with the hip flexion/ extension.

In a similar study, Sangueux et al. [SMC+06] used MRI technique to compute the 3D relative movement between bones and surface markers. The measurements were made on eleven volunteers during active loaded knee extension. Thigh marker sets relative movement expressed the same trend for all subjects: an increased of the relative movement distance with the flexion angle in the range of 3-22mm. Distance of shank marker sets was almost stable at around 4.5mm on all subjects and no tendency was observed. The study concluded that the markers relative movements affected the knee kinematic analysis.

2.3.6 Summary

A summary of the studies on STA assessment is provided in Table 2.2, ordered by anatomical location along the lower limb, from most proximal to most distal [LCCC05]. The studies reported provide a large amount of data associated with the magnitude and the effects of STA at the lower extremities. It should be noted that the divergence between the results reported by the different authors may be due to the use of different techniques and protocols. Moreover, the large variability in the subjects and mainly the different locations of the skin-mounted markers also augment discrepancies. However, some conclusions can be drawn:

- The pattern of the STA is task dependent.

- The pattern of the STA is subject dependent.
- The STA is reproducible within, but not among, subjects.
- The STA introduces systematic as well as random errors.
- The magnitude of the STA is bigger in areas closer to the joints.
- The STA associated with the thigh is greater than any other lower limb segment.
- The STA has a frequency content similar to the actual bone movement; it is hence very difficult to distinguish between the two by means of any filtering technique.

The studies on STA assessment are useful to determinate the factors that should be taken into account, when developing a correction method. Indeed, this avoids working in a wrong research direction. These conclusions naturally contribute to motivate our choices, in terms of algorithm and technical setup (e.g., placement of the markers). We will develop and discuss these motivations in Section 2.5, after having reviewed the advantages and limitations of previous works in STA minimization. We prefer to have all the elements at hand, before summarizing the contributions we intend to bring.

AL	**Motor tasks**	**Technique**	**Subjects**	**Reference**	**Year**
Full thigh	Walking	Intra-cortical pins	5	[RvdBL$^+$97b]	1997
Full thigh	Stance of running	Intra-cortical pins	3	[RvdBL$^+$97a]	1997
Full thigh	Leg swing; walking; cycling; squat	Intra-cortical pins	1	[FLMM97]	1997
Full thigh	Stair climbing, step up/down, sit-to-stand/ stand-to-site, and extension	3D fluoroscopy	2	[SFCL05]	2005
Full thigh	Walking; lateral cutting	Intra-cortical pins	8	[BRL$^+$06]	2006
Full thigh	Hip flex/ext, abd/add, in/ex rotation	MRI	10	[YCGMMT04], [YCMMT04], [YCMT06]	2004, 2006

AL	Motor tasks	Technique	Subjects	Reference	Year
GT, LE, mid thigh (plate and skin)	Walking; cycling; active flexion; hip rotation	External fixators	2	[ACCL92], [CCL+96]	1992, 1996
Mid thigh	Active loaded knee extension	MRI	11	[SMC+06]	2006
Distal thigh	Hip in/ex rotation	Intra-cortical pins	2	[KL94]	1994
Distal thigh	Active knee flexion	Röntgen photo.	3	[SdGLK96]	1996
Distal thigh	One-legged forward hopping	Biplane radiographic sys.	2	[TA02]	2002
Distal thigh	Step-up task	3D fluoroscopy	10	[GKM+07]	2007
Full shank	Walking	Intra-cortical pins	5	[RvdBL+97b]	1997
Full shank	Stance of running	Intra-cortical pins	3	[RvdBL+97a]	1997
Full shank	Leg swing; walking; cycling; squat	Intra-cortical pins	1	[FLMM97]	1997
Full shank	Stair climbing, step up/down, sit-to-stand/ stand-to-site, and extension	3D fluoroscopy	2	[SFCL05]	2005
Full shank	Walking; lateral cutting	Intra-cortical pins	8	[BRL+06]	2006
Proximal shank	Active flexion, impact phase of running	Intra-cortical pins	1	[LL91]	1991
Proximal shank	Hip in/ex rotation	Intra-cortical pins	2	[KL94]	1994
Proximal shank	Step-up task	3D fluoroscopy	10	[GKM+07]	2007
HF, LM, mid shank (plate and skin)	Walking; cycling; active flexion; hip rotation	External fixators	5	[ACCL92], [CCL+96]	1992, 1996
Mid shank (plate)	Walking	Percutaneous trackers	3	[HOS+97]	1997

AL	Motor tasks	Technique	Subjects	Reference	Year
Mid shank (several different clusters)	Walking	Percutaneous trackers	7	[MMS+00]	2000
Mid shank	Active loaded knee extension	MRI	11	[SMC+06]	2006
Distal shank	Stance of walking	Intra-cortical pins	3	[WHH+00]	2000
Distal shank (plate and skin)	Walking	Intra-cortical pins	6	[NJL+07]	2007
Distal shank (plate and skin)	Walking	Intra-cortical pins	2	[WLJ+08]	2008
LM, medial malleolus	Ankle complex inversion/ eversion	Röntgen photo.	10	[MA94]	1994
Medial malleolus	Ankle complex dorsi/ plantarflexion	Röntgen photo.	6	[TK98]	1998
Full foot (shoe)	Walking	Intra-cortical pins	5	[RvdBL+97b]	1997
Full foot (plate and skin)	Walking	Intra-cortical pins	6	[NJL+07]	2007
Heel	Stance of walking	Intra-cortical pins	3	[WHH+00]	2000
Heel (plate and skin)	Walking	Intra-cortical pins	2	[WLJ+08]	2008
Rear foot	Ankle complex inversion/ eversion	Röntgen photo.	10	[MA94]	1994
Rear foot	Ankle complex dorsi/ plantarflexion	Röntgen photo.	6	[TK98]	1998
Forefoot	Stance of walking	Intra-cortical pins	3	[WHH+00]	2000

Table 2.2: Summary table of the studies reporting STA measurements. Mostly reproduced from [LCCC05] used by permission.

2.4 Soft tissue artifact minimization and compensation

STA greatly affects joint kinematics. Therefore, the biomechanics research community concentrated their efforts on devising methods for the compensation and reduction of its effect. The proposed techniques can be distinguished into five categories (Figure 2.8):

- The techniques using *rigid supports*, instead of fixing the markers directly on the skin surface (e.g., Rigid skin frames).
- The techniques exploiting *redundant information* from measured data (e.g., Solidification model, Point cluster technique).
- The techniques using *additional data acquisitions* (e.g., Multiple anatomical landmark calibration, Dynamic calibration).
- The techniques *adding a-priori knowledge* into the compensation process, such as the inclusion of mechanical models of skeleton and/ or soft tissues (e.g., Pliant surface modeling, Global optimization).
- The techniques using *additional technologies*, such as the use of imaging techniques (e.g., MRI, CT, fluoroscopy).

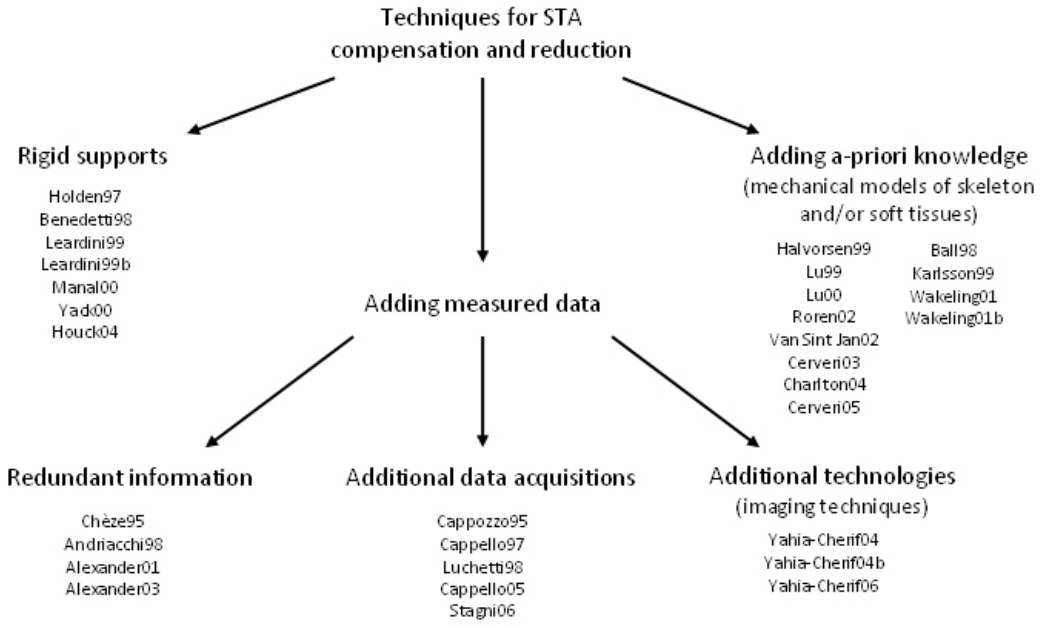

Figure 2.8: The five categories of technique in STA minimization.

These techniques can be also classified in two main groups (Figure 2.9). The first group includes the studies focusing on the optimal estimation of each segment pose individually; irrespective of joint motion and constraints. The second group takes into consideration the physiological motion of the joint. Obviously, the inclusion of joint motion constraints into the overall estimation of segment poses is really appropriate and must be exploited further.

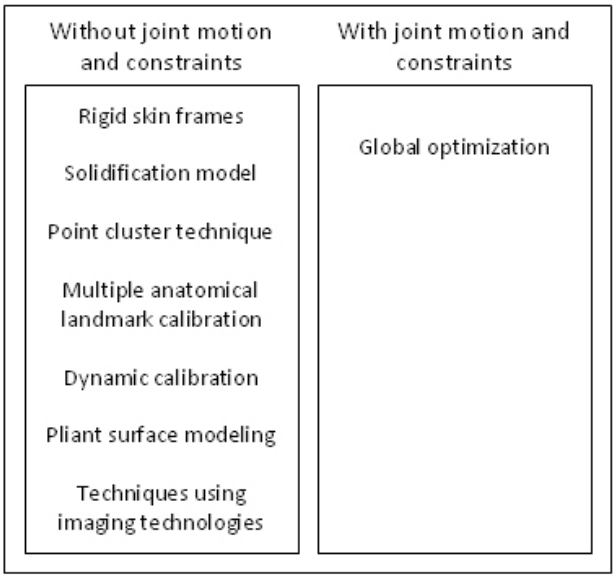

Figure 2.9: The two trends in STA minimization: the first group treats each body segment separately, while the second group includes segment relative motion.

Before reviewing the different techniques, a brief comment on the clusters of markers which are usually employed, is important. The movement of a cluster of markers with respect to the underlying bone can be seen as a sum of an internal cluster deformation (i.e., inter-marker distance changes) plus a rigid displacement. Indeed, internal cluster deformations are generally due to measurements errors when collecting the data, but also due to STA. A cluster of markers also moves rigidly with respect to the underlying bone due almost exclusively to STA. For a complete correction of STA, these two different aspects must be addressed. However, this is not the case of all the proposed techniques, as seen on Figure 2.10.

In the following, we present a state of the art on the existing work aiming to reduce or compensate the contribution of STA. This related work is reviewed per technique and emphasis is put on the benefits and limitations of each technique. We finally conclude this chapter with a discussion on our objectives and contributions, with regard to previous approaches.

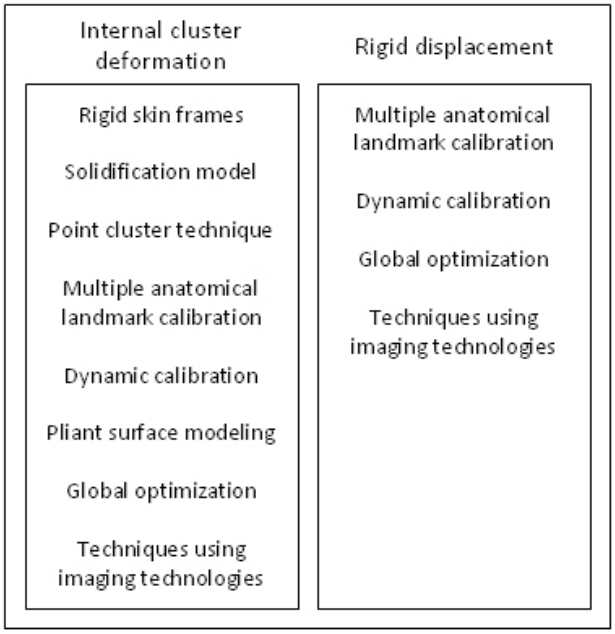

Figure 2.10: The capability of the proposed techniques to cope with the two different movements that a cluster of markers undergoes.

2.4.1 Rigid skin frames

The internal deformation may be reduced by the use of rigid supports [HOS+97] [BCL+98] [LCC+99] [LBC+99] [MMS+00] [YHC+00] [HYC04]. Generally, markers attached to skin frames appeared to provide better results than markers directly attached to the skin. However, the problem still remains, because these skin frames may move relatively to the bone as one unit. Additionally, the latest motion capture technology allows the distribution of a high number of redundant markers all over the body segment surface, which renders in some case the use of rigid support obsolete [CCC06].

2.4.2 Solidification model

Another method to decrease internal deformation was proposed by Chèze et al. [CFD95]. The so-called "solidification" procedure works in two steps. Since only three non-collinear markers are sufficient to determine the segment pose in 3D, the first step consists in the selection of the three markers that define the least-perturbed triangle over the entire motion. The "solid" triangle shape, which best represents this time varying markers configuration, is computed as follows:

- Given m markers on the segment, we seek for the three markers that best represent a rigid triangle. For each possible triangle, we suppose $SD1$, $SD2$ and $SD3$ the standard deviations

in the three vertex angles $\theta 1$, $\theta 2$, $\theta 3$ of the triangle. We compute the sum $\sum_{i=1}^{3} SDi$ and select the triangle with the minimal sum value. This triangle represents the three markers showing the least shape deformation.

- Once the best triad of markers has been determined, the corresponding "solid" shape is defined from the measured triangles using an iterative procedure which calculates the mean value for each vertex angle and eliminates step-by-step the most deformed frame, until 75% of the frames are retained.

In a second step, the best fit of this "solid" shape to the measured triangle is computed at each point in the motion using the standard Single Value Decomposition (SVD) algorithm [SB93], where the function to minimize is:

$$\min \sum_{i=1}^{3} \|\mathbf{R}\mathbf{p_i} + \mathbf{t} - \mathbf{q_i}\|^2$$

with i the number of triangle points, $\mathbf{R}$ the rotation matrix, $\mathbf{t}$ the translation vector, $\mathbf{p_i}$ the initial position vectors and $\mathbf{q_i}$ the target position vectors. Solution of the least-squares problem allows the three measured marker coordinates to be replaced with those corresponding to the "solid" triangle shape.

To evaluate this method, trajectories of markers were generated using experimental data from a swing phase of gait. Artificial noise representing typical skin movement's errors was then introduced to obtain perturbed marker trajectories. Since it was showed [CCL93] that the skin markers move in a systematic rather than random way relative to the bone, the STA were represented as a continuous model of the form:

$$X(t) = A\sin(\omega + \phi)$$

where A is the amplitude of the noise, ω the frequency, t the simulated time and ϕ the phase angle. After evaluation, the results revealed that this iterative method did not reduce the kinematic errors typically obtained with a standard SVD algorithm.

2.4.3 Point cluster technique

A further approach to reduce STA is described in [AAT+98]. This technique considers a cluster of a large number of markers uniformly distributed on the body segment under analysis. Each marker (i) is assigned a mass $m(t)_i$ which may vary at each time frame. The center of mass and the inertia tensor of the cluster points are calculated: at any time t, the location of marker i in the global coordinates

system is denoted by $\mathbf{G}(t)_i$, where

$$\mathbf{G}(t)_i = \begin{bmatrix} g(t)_{i,x} \\ g(t)_{i,y} \\ g(t)_{i,z} \end{bmatrix} \quad i = 1 \dots n$$

The center of mass $\mathbf{C}(t)$ and the inertia tensor $\mathbf{I}(t)$ of the cluster points are given by:

$$\mathbf{C}(t) = \frac{\sum_{i=1} \mathbf{G}(t)_i \, m(t)_i}{\sum_{i=1}^{n} m(t)_i}$$

$$\mathbf{I}(t) = \begin{bmatrix} \sum_{i=1}^{n} \left[(p_{i,y})^2 + (p_{i,z})^2 \right] & \sum p_{i,x} \, p_{i,y} \left[-m(t)_i \right] & \sum p_{i,x} \, p_{i,z} \left[-m(t)_i \right] \\ p_{i,x} \, p_{i,y} \left[-m(t)_i \right] & \sum_{i=1}^{n} \left[(p_{i,z})^2 + (p_{i,x})^2 \right] m(t)_i & \sum p_{i,y} \, p_{i,z} \left[-m(t)_i \right] \\ \sum p_{i,x} \, p_{i,z} \left[-m(t)_i \right] & \sum p_{i,y} \, p_{i,z} \left[-m(t)_i \right] & \sum_{i=1}^{n} \left[(p_{i,x})^2 + (p_{i,y})^2 \right] m(t)_i \end{bmatrix}$$

where

$$\mathbf{P}(t)_i = \mathbf{G}(t)_i - \mathbf{C}(t) \quad i = 1 \dots n$$

Finally, the eigenvalues and eigenvectors of the inertia tensor are used to define coordinates systems in the cluster and to provide a basis to address soft tissues' movements. Indeed, the eigenvalues of the inertia tensor remain invariant if the segment is behaving as a rigid body. Therefore, the basic idea is to adjust the mass of each marker at each step to minimize changes of eigenvalues.

This method was tested in a simulation model, where systematic and random errors were applied to a fixed cluster of points. The error due to non-rigid body movements could be significantly reduced. The method was also tested with ten subjects during walking and provided comparable results to intra-cortical bone pins derived motion applied for the knee (data obtained from a previously reported study [LCSK92]). The technique was expanded in [AA01] [ABA03] by imposing a functional form on marker motion relative to the underlying bone. Techniques for modeling and subsequently estimating general cases of segment deformation were developed. This further method was tested *in vivo* on a patient wearing an Ilizarov device at the shank. Errors in limb segment pose decreased by 25% and 33% in position and orientation, though the numerous pins of the device likely reduced the natural skin movement.

Drawback of the point cluster technique is associated with the overabundance of markers which can lead to difficulties in tracking and marker's labeling (occlusion problems). Furthermore, a recent study [CCC06] has shown that this method is unstable and that it does not perform better than traditional

bone pose estimators (e.g., SVD algorithm).

2.4.4 Multiple anatomical landmark calibration

As previously mentioned in the introduction (see Section 1.3), an anatomical calibration is necessary to establish a correspondence between the markers setup and the bone segments (i.e., movement/ morphology data registration). Cappozzo et al. [CCCL95] proposed a single static calibration of a number of ALs for the determination of their local coordinates in the relevant marker cluster technical frame (CTF). The location of an AL in the CTF is identified by placing a marker on it or by using a pointer mounting two markers in known position. Technical markers (i.e., markers not placed on ALs) are also placed on the subject. Then, at least one frame is recorded and this procedure is repeated for each AL. Moreover, through obvious geometric calculations and by using the reconstructed positions of the ALs, the relevant anatomical frames (AF) are determined. This technique is referred to as the "Calibrated Anatomical System Technique" (CAST) and is nowadays used as the standard anatomical calibration technique. In a later study [CCP+97], this technique is enhanced with a double calibration performed at the two extremes of the expected range of motion of a specific motor task. With the hypothesis that the skin moves linearly with respect to the underlying bone between the two extremes of the range of motion, a time-varying model is computed through linear interpolation between the two calibrations. This time-varying model along with the calibration parameters are then used to compensate the skin sliding effect during the intermediate postures.

The validation of this technique was performed with a subject wearing a femoral external fixator during a cycling exercise. The first calibration (E) was collected at maximum hip/ knee extension and the second one (F) at maximum flexion (Figure 2.11). The RMS reconstruction error for an AL (greater trochanter) decreased from $15mm$ to less than $10mm$, while the RMS of femur orientation and position decreased respectively from approximately 5° and $7mm$ to less than 4° and $4.5mm$. Nevertheless, the linearity assumption limits the applicability of this technique.

To overcome this, the technique is expanded in [CSFL05]. Instead of considering a linear time interpolation, the new method is based on a knee flexion/ extension angle interpolation of two AL calibrations taken at the extremes of motion. The evolution of this method comes from the observation that the propagation of STA to the knee kinematics depends on the flexion/ extension range [CCCL97]. The validation of this double calibration was assessed on two subjects during several motor tasks (step up/ down, sit-to-stand/ stand-to-sit, and flexion against gravity), where the performance on knee rotation and translations was tested on a kinematics dataset obtained by the synchronous combination of

stereophotogrammetry and 3D fluoroscopy. Knee rotations and translations were found to be reliable compared to the fluoroscopy-based gold standard. The residual mean values of the RMS error were 1.5°, 1.4°, and 1.6° for flexion/ extension, abduction/ adduction and internal-external rotation, and 2.0, 2.8, and 2.1mm for anterior/ posterior, vertical, and medio/ lateral translations, respectively. Later on, the effectiveness of the double calibration in reducing the effects of STA on knee kinematics, when AL misplacement is present on the thigh and shank, was also determined in [SFC06]. The results showed that the double calibration was still effective even with large misplacement errors.

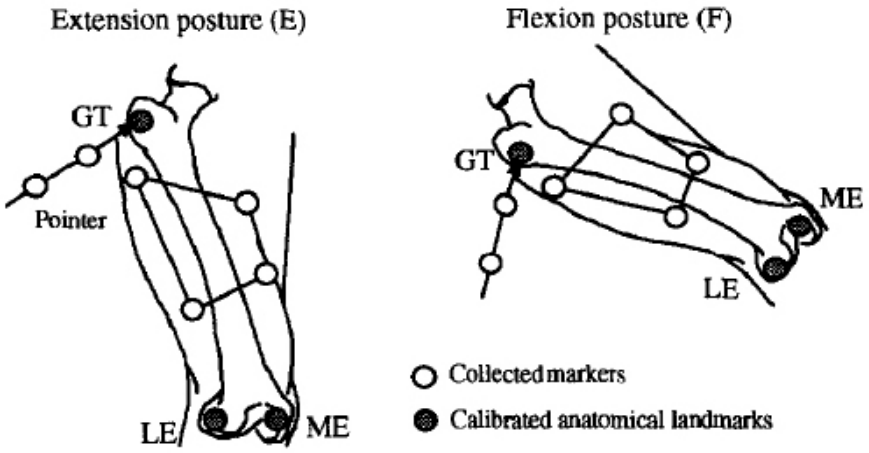

Figure 2.11: Technical markers and ALs in the double static calibration for cycling: a) extension posture and b) flexion posture. Image from [CCP+97] used by permission.

The double calibration provides promising results, but the assumption that the dynamic deformation, which will be recorded during an actual activity, is equivalent to the static deformation is a limiting factor. In addition, the performance of the double calibration was tested when considering knee joint kinematics only and during motion involving knee flexion/ extension exclusively. Therefore, the technique should be experimented with other joints and with more complex movements (i.e., combining motion in the three anatomical axes), before attesting its real efficiency. The main drawback is the increased number of data acquisitions required, which is clinically problematic.

2.4.5 Dynamic calibration

Lucchetti et al. [LCCC98] presented an experimental and analytical procedure which estimates the skin movement's artifacts at the knee joint. Three subjects participated in the study, where one of them was wearing a prosthetic knee for validation purpose. Four markers were located on the

pelvis through a rigid plate, and five and four markers were fixed on the thigh and shank segment surfaces, respectively. A reference frame was associated with the pelvis, thigh, and shank segments, and another to the thigh-shank segment. Several motor tasks were recorded: a) upright posture b) hip flexion/ extension followed by abduction/ adduction with hyperextended knee c) hip and pelvis 3D rotation with hyperextended knee simulating the walking swing phase d) level walking. Since STA is less important at the shank than at the thigh in a knee-locked leg, in both upright posture and gait-simulated hip rotation, medial and lateral femur epicondyle positions were estimated on the basis of the rigid thigh-shank frame defined by markers on the shank. A discrete function, the "artifact table", was then computed based on the displacement of these ALs in the thigh reference frame as functions of hip angles. This table was used to compensate STA during walking. With this technique, they reported a decrease in RMS errors for femur and tibia pose from $14mm$ to $4mm$ and from $6°$ to $3°$. The correlation between STA and hip rotations was thus successfully removed. However, this approach is limited, because it assumes that the skin motion during the artifact assessment movements is the same as during the dynamic activities. This procedure was also tested for the knee joint only. Thus, its effectiveness must be reconsidered after evaluation with other joints. Moreover, as for the double calibration, this technique is time consuming due to the additional data acquisitions required.

2.4.6 Soft tissue modeling

Adding soft tissue knowledge into the compensation process was investigated. Ball and Pierrynowski [BP98] introduced the pliant surface modeling. This method provides for simultaneous quantification of rigid rotations and translations, plus "pliant" (scales and shears) motion to describe soft tissue changes. Deformations were described with affine transformation matrices (12 DOFs) accounting for translation, rotation, scaling and shearing. To validate the method, three subjects were instrumented with bone pins inserted into the femur and tibia over the greater trochanter and Gerdy's tubercle. Clusters of skin markers were also stuck on the thigh and on the shank. Walking trials at three different speeds were recorded. The results showed an error reduction in femur and tibia segment position of 45% and 56%, with respect to techniques not taking into account the cluster deformation. The improvement in segment orientation was negligible ($< 0.5°$). The rigid cluster displacement is also not accounted in this method.

Further studies were conducted for assessing soft tissue stiffness and vibrations in the leg. Even though these studies are not directly related to STA minimization, their concepts and approaches are relevant here. In [KT99], soft tissue measurements were performed to determinate whether certain skin portions provide a more rigid base for markers than others. Two parameters were investigated:

the local stiffness of different attachment sites along the leg and the resonant frequencies of wand marker systems. The stiffness k (N/m) was calculated from the equation:

$$k = \frac{F}{\Delta}$$

where F is the load (N) and Δ is the measured deflection (m). The deflection of the skin when subject to a force of 2.5N varied between 1.3 and 7.5mm. The largest stiffness values were found at the knee joint. For oscillations measured after a sudden release from an initial displacement, all tests (with relaxed or activated muscles) demonstrated an under-damped vibration response. When the muscles were tensed, the main resonant frequency generally increased (Figure 2.12). The study concluded that the markers should be placed away from areas close to joints, as previously recommended in [CCL+96]. Furthermore, it was showed that increased muscle tension provided a more stable base, producing increased stiffness.

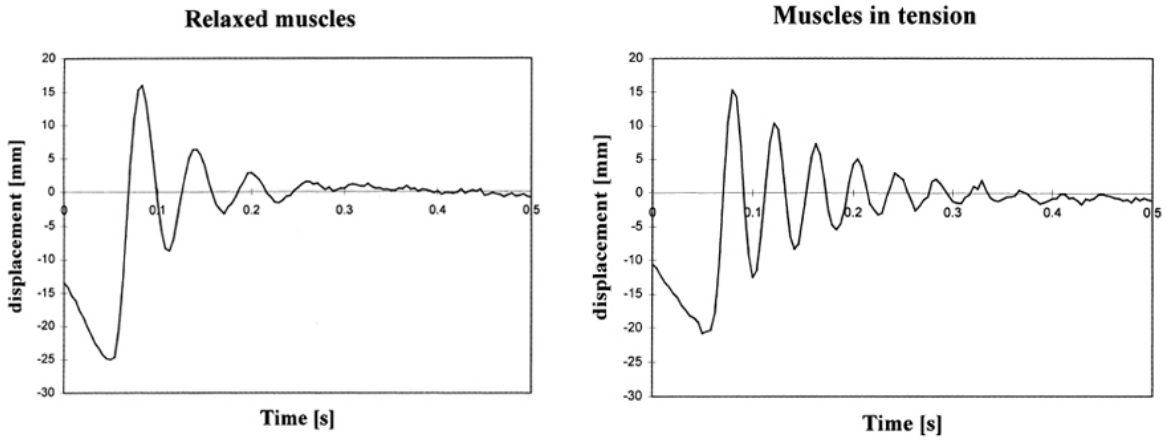

Figure 2.12: Vibration response of a 30mm wand marker after release with relaxed muscles and muscles in tension. Image from [KT99] used by permission.

Two later studies [WN01a] [WN01b] proposed methods to characterize the frequency and damping of vibrations in the soft tissues of the leg. These vibrations were measured with an accelerometer, while isometric and isotonic contractions of the leg were performed at different joint angles. To determine the frequency and damping coefficient, each vibration signal was analyzed. These coefficients were calculated using a least-squares minimization (Levenberg-Marquardt) method of the following equation:

$$s = a\mathrm{e}^{-ct}\sin(2\pi ft + \varphi)$$

where s is the measured signal, a is the amplitude of the vibration, c is the damping coefficient, f is the damped natural frequency, and φ is a phase coefficient. The measured vibrations were all under-damped and the results revealed that vibration characteristics changed with the muscle length (i.e., joint angle) and between tested individuals.

In conclusion, the studies measuring soft tissue deformations provide interesting results and could be employed for the development of new STA minimization methods, but soft tissue mechanical models are difficult to implement given the high variability of the subjects and marker positioning.

2.4.7 Global optimization

Previous techniques present a similitude: no joint constraints are imposed. It was observed [KASS94] that STA can induce non-physiological joint translation or even dislocation. Therefore, Lu and O'Connor [LO99] [LO00] proposed a method that iteratively and globally optimize joint center locations and segment orientations at the system level. Rather than estimating skeletal pose of each segment individually, this method models the articulations as ball and socket joints and uses a multi-link musculoskeletal model with joint constraints (Figure 2.13).

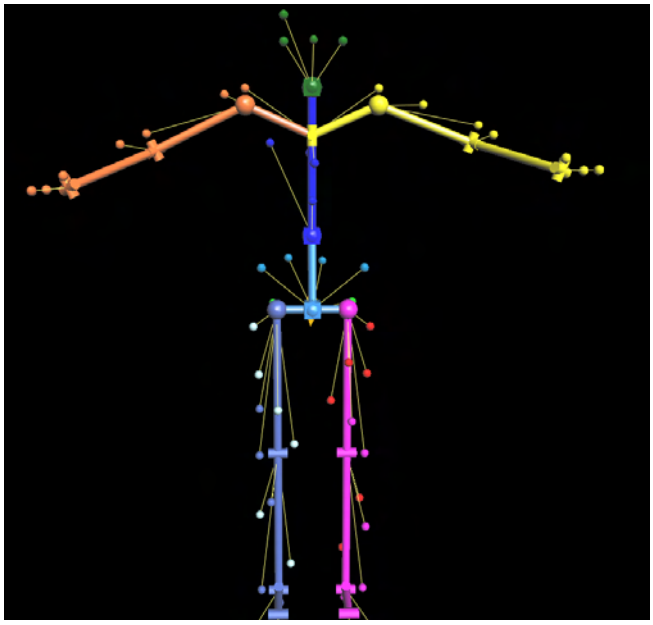

Figure 2.13: Typical representation of a multi-link model with ball and socket joints. The small spheres linked to each segment correspond to the skin markers.

Segmental optimization methods estimate the segment pose in terms of its transformation matrix by

minimizing marker array deformation from its reference shape. In a traditional least-squares sense, this results in solving the following objective function:

$$\min \ f = \sum_{i=1}^{m} (\mathbf{R}\mathbf{x_i} + \mathbf{v} - \mathbf{y_i})^{\mathrm{T}} (\mathbf{R}\mathbf{x_i} + \mathbf{v} - \mathbf{y_i})$$

with

$$\mathbf{R}^T\mathbf{R} = \mathbf{I}$$

where $\mathbf{x_i}$ and $\mathbf{y_i}$ are position vectors of marker i in the marker array at the reference and current positions, respectively, $\mathbf{R}$ is the rotation matrix, $\mathbf{v}$ is the translation vector and m is the number of markers. The constraint $\mathbf{R}^T\mathbf{R} = \mathbf{I}$ ensures that the transformation is orthogonal, corresponding to a rigid body motion.

To better account for STA, the previous function is modified so that the estimations of the skeletal positions and orientations are based on a global optimization aiming at minimizing the sum of squared distances between actual and model-determined marker positions, throughout all the body segments. This is done as follows: each marker array is used to define a segment-embedded reference frame and marker position vectors are represented in their local reference frames, denoted together as $P^* = [P_1^*, P_2^*, \ldots, P_n^*]$, where $P_i^* = [P_1^*, P_2^*, \ldots, P_m^*]_i$ are the local marker position vectors on segment i. Given a set of measured marker coordinates P on a data frame, the global optimization at the system level is to find a set of generalized coordinates ξ such that the following error function

$$f(\xi) = [P - P'(\xi)]^T \mathbf{W} [P - P'(\xi)]$$

is minimized. $P'(\xi)$ is the corresponding set of marker coordinates calculated by the following transformation:

$$P'(\xi) = \mathbf{T}(\xi)P^*$$

where $\mathbf{T}(\xi)$ is the combined transformation matrix from segment-embedded frames to laboratory frame and is calculated by the model for a given ξ. $\mathbf{W}$ is a positive-definite weighting matrix of the form:

$$\mathbf{W} = \begin{bmatrix} W_0 & 0 & 0 & 0 \\ 0 & W_1 & 0 & 0 \\ 0 & 0 & \ddots & \\ 0 & 0 & 0 & W_n \end{bmatrix}$$

where W_i is a $(3m_i \times 3m_i)$ weighting matrix assigned to the i^{th} segment to reflect the error distribution among the m_i markers. Thus, a different weighting factor reflecting its average degree of STA is given to each segment. However, all markers of a segment are equally affected by STA.

This method was tested with 20 simulated gait trials, where artificial noise (same formulation as in Chèze et al. [CFD95]) was added to obtain perturbed marker trajectories. The authors reported errors in joint rotations (mainly in axial rotation and abduction/ adduction) to be significantly reduced compared to the traditional one. Moreover, joint dislocations were eliminated. The performance of this method was only assessed on simulated data.

This global optimization method is at the basis of a series of similar STA compensation methods [HLL99] [RT02] [JSH+02] [CPF03] [CTR04] [CPF05], which have also been implemented in some commercial software tools for the elaboration of motion analysis data. Thanks to mechanical models of skeleton, the repeatability of kinematic measurements was demonstrated [RT02] [CTR04], but the main limitation of these methods are due to the assumption of ball and socket joints. Indeed, joints structures are simplified and are no more subject-specific, since the segments are complied to behave as idealized joints (i.e., no shifts are allowed). Therefore, the results could hide abnormal joint behaviors, which is not suited for the study of joint pathologies [SFC08].

2.4.8 Techniques using imaging technologies

In different papers, Yahia-Cherif et al. [YCGMMT04] [YCMMT04] [YCMT06] presented a completed methodology for the estimation of the hip joint kinematics by combining MRI and optical motion capture. In a first step, MRI was used to quantify the markers displacements and to select the best markers configuration to be used with the optical system. Then, a correction algorithm was developed based on the markers movements, in order to reduce the STA errors.

To determine the optimized skin markers configuration, nine reflective markers were injected with a contrast agent and distributed all over the thigh. The bones and the markers were tracked in dynamic MRI during clinical motion patterns (hip internal-external rotation, flexion/ extension, and abduction/ adduction). The MR series were processed and the trajectories of the visible markers were calculated using the tracking method. Each marker m_i was associated with an error r_i corresponding to the sum of its displacements from frame to frame, as follows:

For each marker m_i

For each frame t

Calculate the marker's sum of displacements $\sum d_i$

Assign to m_i the error $r_i = \sum d_i$

For each triplet of marker (m_i, m_j, m_k)

If (Check_colinearity(m_i, m_j, m_k))

Calculate the distance $d_{ijk} = d(m_i, m_j) + d(m_j, m_k) + d(m_k, m_i)$

Calculate the error $r_{ijk} = r_i + r_j + r_k$

Check_colinearity(m_i, m_j, m_k): return yes if the 3 markers are non-collinear and no otherwise

The best markers m_i, m_j, m_k were chosen as the most distant ones (maximum value of d_{ijk}) with the less relative motion (minimum value of r_{ijk}). Thus, the best three markers were determined by minimizing the fraction d_{ijk}/r_{ijk} using an exhaustive search. This optimized configuration (Figure 2.14) was then used for recording external movements with an optical motion capture system.

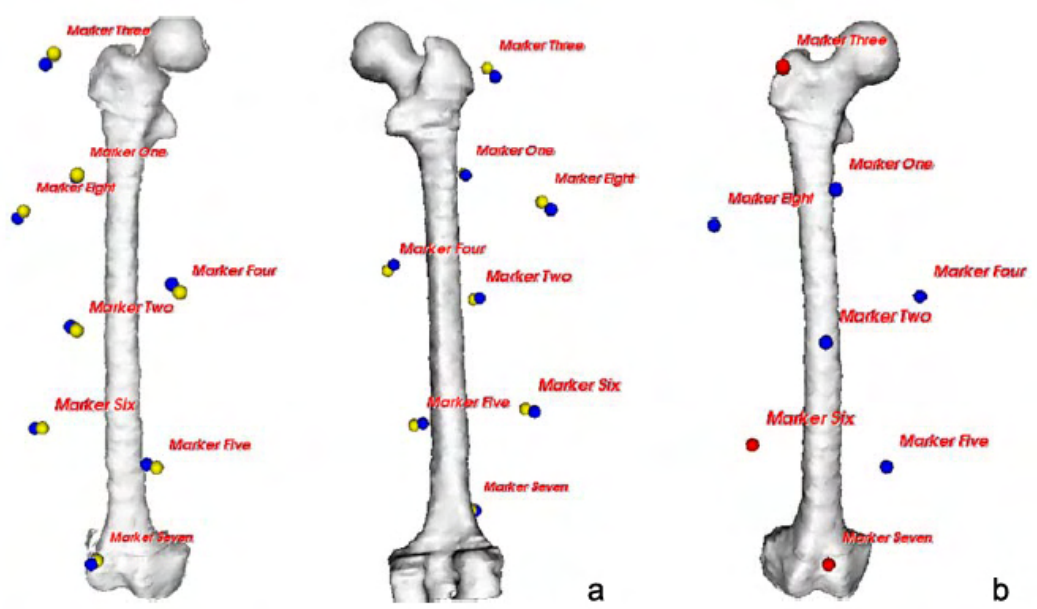

Figure 2.14: a) Markers displacements: yellow = real markers positions, blue = calculated positions b) Best markers selection (in red). Image from [YCGMMT04] used by permission.

Having the markers displacements values, the next step was to analyze the data, in order to infer a correlation between the displacements values and the movements performed. A Principal Component

Analysis (PCA) [Jol86] and a Common Factor Analysis (CFA) [Mor99] were used for this purpose. The statistical analysis showed that the markers displacements in the Z-direction were correlated with hip internal-external rotation, while the displacements in Y-direction were correlated with the hip flexion/ extension. To correct STA, these markers displacements were modeled as a quadratic function for evaluating the displacements in the Z-direction as function of internal-external rotation angle, whereas the displacements in Y-direction as a function of flexion/ extension angle were approximated with a cubic modeling. With this correction procedure, the authors claim a significant reduction in thigh STA error, but the tests and validation were only performed analytically (i.e., not on experimental data).

The optical motion capture system was finally used to record larger ranges of motion than those available with the MRI scanner. Clinical motion patterns and conical motion were recorded to assess possible femoroacetabular impingements. To derive the hip joint kinematics from the markers trajectories, a virtual skeleton was used. The use of this skeleton hence limits the applicability of this methodology, since the model is not subject-specific. Moreover, the subject calibration (i.e., to fit the skeleton to the subject) performed before the motion recording was prone to error (error $\approx 2cm$ per segment), which is not accurate for medical applications.

2.5 Discussion

In the previous sections, we have seen that many techniques have been addressed to minimize the effect of STA. Each technique has its own advantages and drawbacks, but the solutions developed comprise limitations. The most critical source of error is the rigid motion of the cluster with respect to the underlying bone, rather than the relative deformation of the cluster itself. Thus, the compensation techniques [CFD95] [BP98] [AA01] taking into account only the deformation of the cluster are not expected to perform significantly better than a simple least-squares minimization algorithm. Beside STA errors, additional errors are the consequence of an inaccurate anatomical calibration. Indeed, most kinematic studies use the CAST protocol [CCCL95] (see Section 2.4.4) to perform the calibration, but this technique lacks accuracy and precision in the determination of ALs (e.g., error up to $18mm$ for the great trochanter [CCK99]), due to the overlying soft tissues or to AL misplacement [CLCC05]. This affects AF position and orientation precision and, consequently, the estimation and interpretation of joint kinematics. Although methods [DCVC07] [DCVC08] [SJC$^+$09] were proposed to enhance the CAST protocol, this calibration is still an open issue. In conclusion, improvements in the reconstruction of human skeletal system 3D kinematics are expected and needed.

The methods we propose in the coming chapters are meant to reduce the calibration and STA errors in all steps of the motion estimation process, namely in the motion recording phase, in the anatomical calibration phase and in the bone pose computation phase. Our methodology is applied to the hip joint, but could be also *applicable to other joints* (i.e., the methods we propose are quite generic). For each step, the following actions are taken:

- Motion recording phase: the studies quantifying the effect of STA show that STA depend on the marker location variability. Indeed, markers placed close to the joints undergo more movements. Non redundant markers also increase the effect of STA. Therefore, our strategy is to use a markers configuration including a *high number* of *redundant* markers all over the segment surface and located *far* from the joints.

- Anatomical calibration phase: this phase entails the localization of the bone segments in the CTF and the determination of the relevant AFs. As opposed to the CAST protocol, our intent is to compute joint coordinate systems from ALs defined *on the reconstructed 3D surface of the bones* from MRI, in order to cope with the inaccuracies in the determination of ALs. Furthermore, our idea is to digitalize the subject's body with the skin markers, using a *3D body scanner*. In this manner, markers positions can be easily identified on the resulting body scan mesh. Then, this mesh can be registered with the skin generated from MR images, performing the *required calibration*.

- Bone pose computation phase: the studies assessing STA show that STA introduces systematic errors as well as random ones. Thus, our bone pose estimation algorithm should be robust and accurate enough to deal with nonlinear markers movements. In contrast to previous bone pose estimators and global optimization methods that generally solve the optimization problem linearly, we propose to use a more powerful optimization algorithm, a *sequential quadratic programming algorithm* [LT01], to minimize the cluster deformation. We will demonstrate that this *nonlinear* optimization algorithm is *robust*, *more accurate*, and converges *faster* than the classical methods. To cope with the rigid motion of the cluster, our approach is not meant to impose strong kinematic constraints, as this was addressed in [LO99]. We rather aim at applying *little* joint constraints, allowing some *shifts* at the joint. This is actually done in two phases:

  - To avoid non-physiological joint translation or even dislocation, the HJC is kept fixed during the first phase.
  - Although the HJC can be considered to be fixed during low amplitude movements, this is no longer true for extreme motion [GKCMT$^+$09]. Indeed, a potential subluxation may

occur to avoid bone-to-bone penetration. Thus, our algorithm adjusts the HJC by *detecting collisions* among the articulating bones, the goal being to reach the non-penetrating state.

Our bone pose estimation algorithm can be run in *real-time*, which depicts a fast method given the complexity of the task.

Compared to other compensation methods [LCCC98] [CSFL05], our methodology requires *only one* additional data acquisition that is a 15 seconds scan of the subject's body surface. Our protocol is thus clinically much *more feasible*. Finally, the validation of our methodology is obtained using marker position data collected during clinical motion patterns from volunteers scanned in a dynamic MRI protocol. Such acquisitions can provide reliable rigid bone frames, hence the possibility of comparing the kinematics derived from the marker position data with that of the dynamic MRI-based gold standard.

Chapter 3

Motion study of the hip joint

[1]Pietro da Cortona, 1596-1669. Tabulae anatomicae a celeberrimo pictore Petro Berrettino, Romae: Impensis Fausti Amidei, Ex typographia Antonii de Rubeis, p. 32, pl. XII, 1741. Collection Léo-Pariseau. Bibliothèque des livres rares et collections spéciales, Université de Montréal. Image from `http://www.bib.umontreal.ca/CS/livre-savant/renaissances/fiches/cortone02.htm` used by permission.

3.1 Introduction

Human movement analysis aims at gathering quantitative information about the movement of the skeleton. In particular, information is sought concerning the relative movement between the adjacent bones (i.e., joint kinematics). This is either measured or estimated using mathematical models of the musculoskeletal system. Generally, each portion of the skeleton is referred to as bone segment. Those segments are considered non-deformable and are thus represented by using rigid bodies, according to Classical Mechanics. In fact, the estimation of joint kinematics in the 3D space requires the determination of the instantaneous position and orientation of the segments under investigation. Then, through mathematical calculations, the relative motion between articulating bones can be derived.

This chapter is dedicated to the theory related to the kinematic study of the hip joint. Theoretical foundations of human joint motion are presented and discussed with a special focus on methods adopted in this thesis. Since morphological information plays an important role both for the 3D realistic reconstruction of the hip joint and for the numerical description of kinematics, we first provide a general overview of the hip joint anatomy. Then, conceptual and analytical bases that are necessary for the analysis of hip joint motion are described. We introduce the bones and joint coordinate systems (set of axes, joint center) used in this thesis to report joint motion in a repeatable way. We present the clinical movements of the hip joint with their respective ranges of motion. Eventually, we demonstrate the mathematical formulas for describing joint kinematics.

3.2 Anatomy of the hip joint

This section presents the gross anatomy of the hip joint. To gather this description, web-available information was used such as the Gray's anatomy[1], and medical illustrations were taken from *The Atlas of Human Anatomy* [Net06] by Frank H. Netter, MD[2].

3.2.1 Osteology

The hip joint or coxal articulation links the hip bone and the femur. The hip bone is large, flattened and irregularly shaped. It consists of three bones: the ilium, ischium and pubis, which meet at a large cup-shaped articular cavity known as the acetabulum (Figure 3.1). In a young subject, these three bones are distant from one another, but are fused in the adult. The superior margin of the ilium is easily palpable and is called the iliac crest. The crest is thinner at the center than at the extremities,

[1] `http://en.wikipedia.org/wiki/Gray's_Anatomy`, accessed November 2009
[2] `http://www.netterimages.com/artist/netter.htm`, accessed November 2009

and ends in the anterior and posterior superior iliac spines.

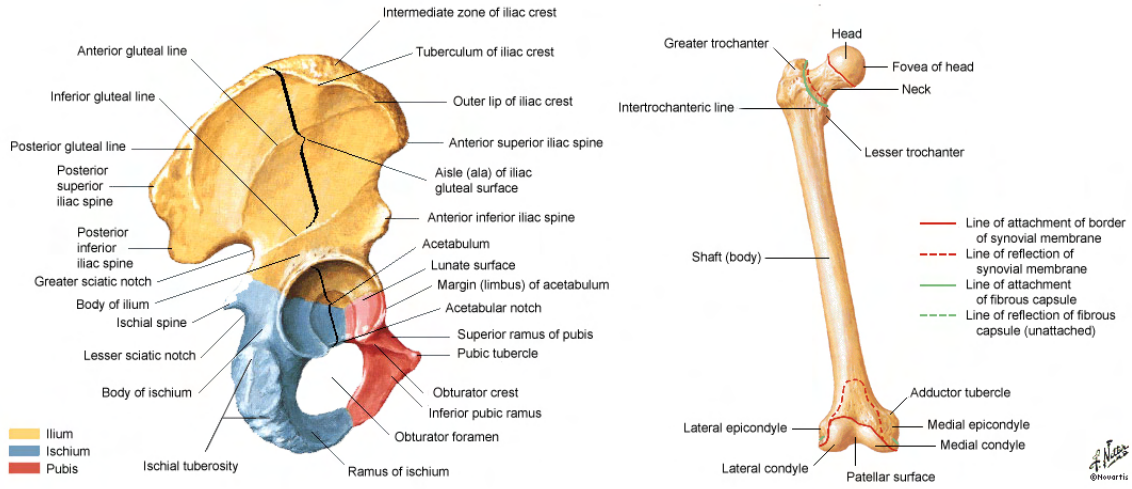

Figure 3.1: The hip bone (lateral view) and the femur (anterior view). Netter illustration from `www.netterimages.com` ©Elsevier Inc. All rights reserved.

The femur is the longest and strongest bone in the skeleton. It is divisible into a body and two extremities (Figure 3.1). The body is called the shaft of the femur. The proximal extremity includes the head, the neck, and the greater and lesser trochanters. The femoral head has a conchoid shape [Men97] and its angular value is 240 degrees. In the middle part, the head is deepened by the cavity of the teresfemoris ligament (or round ligament) ensuring its vascularization. The acetabulum curvature is perfectly adapted to the femoral head curvature, but its angular value is 180 degrees only. This partial covering allows the movement [Kap96]. The neck of the femur connects the head to the shaft and is limited by the greater trochanter. The distal extremity of the femur is larger than the proximal extremity and consists of two condyles, the medial and lateral. They are easily palpable during knee flexion/ extension. Each condyle is surmounted by an elevation, the epicondyle (medial and lateral), that is also palpable.

3.2.2 Syndesmology

The joints are classified structurally or functionally [TA75]. Structural classification is determined by how the bones connect to each one another (e.g., fibrous, cartilaginous or synovial joints), while functional classification is determined by the degree of movement between the articulating bones. The synovial joints are the most common and most movable joint in the human body. The articulating bones are separated by a fluid-containing joint cavity. The ends of the bone are covered with articular

cartilage and the bones are interconnected by ligaments lined with synovial membrane. There exist six categories of synovial joints: hinge (1 DOF), pivot (1 DOF), condyloid (2 DOFs), saddle (2 DOFs), ball and socket (3 DOFs) and gliding (6 DOFs). The hip joint is an enarthrodial or ball and socket joint, formed by the reception of the head of the femur into the cup-shaped cavity of the acetabulum. This articulation is at the same time very stable and very mobile. It ensures the junction trunk-lower limb and supports half of the weight of the bust, head, upper limbs and the pelvis in an upright position. In reality, it supports quite higher constraints when the body is in motion.

The articular surface is entirely recovered by hyaline cartilage. The articular cartilage is slightly elastic and compressible making it able to absorb large compressive and shear forces. The thickness varies from 5 to $7mm$ in young healthy joints, whereas it becomes thinner and less regular with increasing age. The acetabular labrum is a fibrocartilaginous rim attached to the margin of the acetabulum, by which the cavity is rendered deeper. At the same time, the labrum protects the edge of the bone, and fills up the inequalities of its surface (Figure 3.2). The labrum bridges over the notch as the transverse ligament, and thus forms a complete circle which closely surrounds the head of the femur, and assists by holding the latter into place.

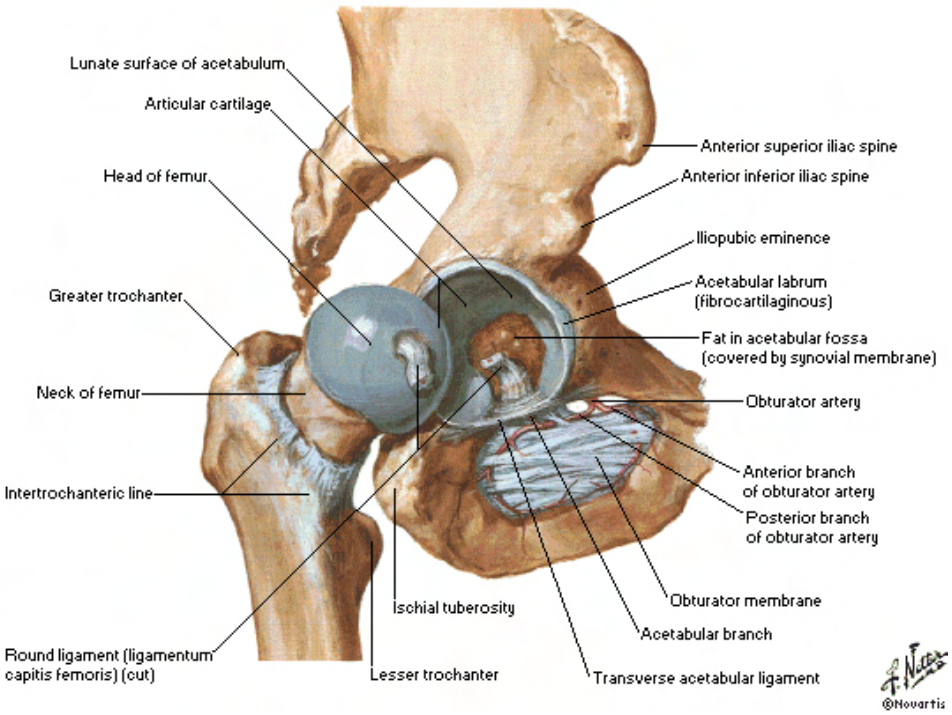

Figure 3.2: The hip joint (lateral view). Netter illustration from `www.netterimages.com` ©Elsevier Inc. All rights reserved.

The articulation is firmly wrapped by the articular capsule. The synovium is a membrane that covers all the non-cartilaginous surfaces within the articular capsule. It secretes synovial fluid into the joint, which nourishes and lubricates the articular cartilages. To ensure joint stability, the bones are connected by three ligaments: the iliofemoral, the ischiofemoral and the pubofemoral ligaments (Figure 3.3).

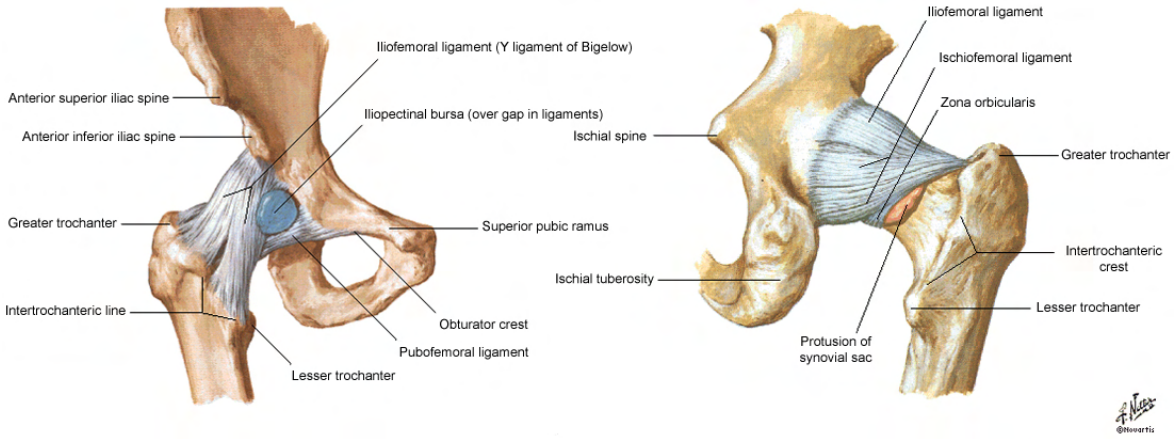

Figure 3.3: The ligaments of the hip (anterior and posterior views). Netter illustration from `www.netterimages.com` ©Elsevier Inc. All rights reserved.

3.2.3 Myology

The muscles are responsible for posture and movement, and are connected with the bones, cartilages, ligaments, and skin, either directly, or through the intervention of fibrous structures, called tendons or aponeuroses. They are arranged in opposing groups around the joints and are bundles of contractile fibers that are organized in a regular pattern. Figure 3.4 shows the muscles of the hip and thigh. The muscles which flex the femur on the pelvis are the Psoas major, Iliacus, Rectus femoris, Sartorius, Pectineus, Adductores longus and brevis, and the anterior fibers of the Gluteus medius and minimus. Extension is mainly performed by the Gluteus maximus, assisted by the hamstring muscles and the ischial head of the Adductor magnus. The thigh is adducted by the Adductores magnus, longus, and brevis, the Pectineus, the Gracilis, and lower part of the Gluteus maximus, and abducted by the Gluteus medius and minimus, and by the upper part of the Gluteus maximus. The muscles which rotate the thigh inward are the Gluteus minimus and the anterior fibers of the Gluteus medius, the Tensor fasciae latae and the Iliacus and Psoas major; while those which rotate the thigh outward are the posterior fibers of the Gluteus medius, the Piriformis, Obturatores externus and internus, Gemelli superior and inferior, Quadratus femoris, Gluteus maximus, the Adductores longus, brevis,

and magnus, the Pectineus, and the Sartorius.

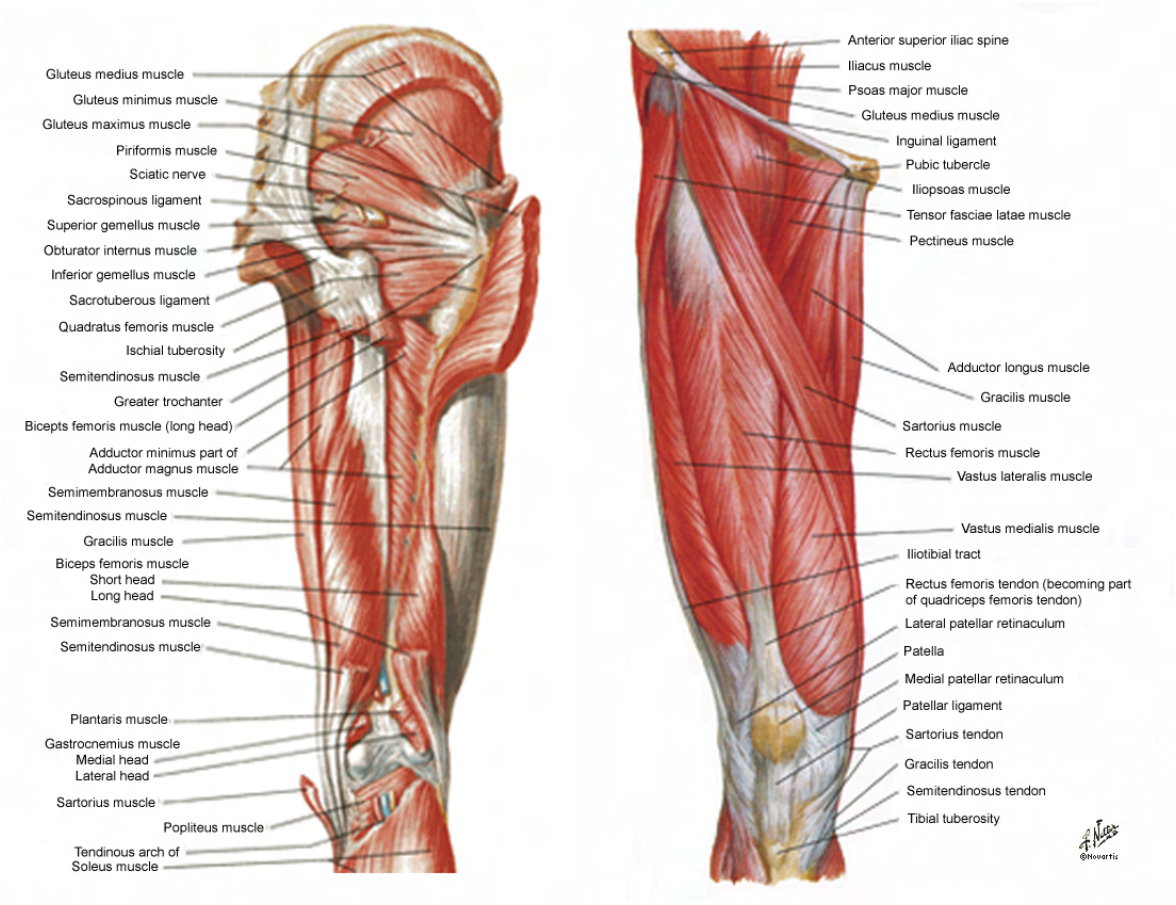

Figure 3.4: The muscles of the hip and thigh (posterior and anterior views). Netter illustration from `www.netterimages.com` ©Elsevier Inc. All rights reserved.

3.3 Segmental kinematics

In human movement analysis, each portion of the skeleton is referred to as bone segment. Those segments are considered non-deformable and are thus represented by using rigid bodies, according to Classical Mechanics. The objective of segmental kinematics is to gather necessary numerical information for the reconstruction of a segment in space in each sampled time instant, during the execution of a motor task. To this end, information related to geometry and motion is required.

In 3D graphics, a bone segment is represented by a set of vertices, where the position vector of each

vertex relative to an orthogonal set of axes (local frame) is denoted by:

$$^{l}\mathbf{p} = \begin{bmatrix} ^{l}p_x & ^{l}p_y & ^{l}p_z \end{bmatrix} \tag{3.1}$$

Obviously, with more vertices used, the description of the segment will be more detailed. Since the bone segment is non-deformable, the vertex position vectors are invariant with respect to time and are therefore measured only once during the experiment. The same principle applies to the inertial parameters (e.g., location of the centre of mass, mass moments of inertia) of the segment involved.

The geometry of a segment may be represented with respect to any arbitrary frame, that is, with respect to any observer. Given a local and a global frame, the position vectors of the segment vertices ($^{l}\mathbf{p}$) can be defined in the global frame ($^{g}\mathbf{p}$), through to the following equation (Figure 3.5):

$$^{g}\mathbf{p} = {}^{g}\mathbf{R}_{l}\,{}^{l}\mathbf{p} + {}^{g}\mathbf{o} \tag{3.2}$$

where

$$^{g}\mathbf{R}_{l} = \begin{bmatrix} \cos\theta_{x_g x_l} & \cos\theta_{x_g y_l} & \cos\theta_{x_g z_l} \\ \cos\theta_{y_g x_l} & \cos\theta_{y_g y_l} & \cos\theta_{y_g z_l} \\ \cos\theta_{z_g x_l} & \cos\theta_{z_g y_l} & \cos\theta_{z_g z_l} \end{bmatrix} \tag{3.3}$$

defines the orientation of the local, relative to the global, frame and is referred to as the orientation matrix, and $^{g}\mathbf{o}$ is the position vector of the origin of the local frame relative to the global frame. The column elements of the orientation matrix are the direction cosines, or the unit vector components, defining the orientation of each local frame axis relative to the global frame. Since the frame axes are mutually orthogonal and that triplets of them represent unit vectors, six scalar equations may be written that reduce the number of independent elements to three. In summary, three scalar independent quantities define the relative orientation and three the relative position. The segment can thus be viewed from any other global perspective using only six numerical values.

The same formula may be used to describe segment motion as well, since the description of motion is characterize by the relative position of a local frame and its changes through time. In fact, if the pose of the local frame is described in each sampled instant of time during movement relative to a global frame by giving the six independent scalar quantities implied in $^{g}\mathbf{R}_{l}$ and $^{g}\mathbf{o}$, then the segment geometry ($^{l}\mathbf{p}$) can be reconstructed in its instantaneous location ($^{g}\mathbf{p}$) through Equation (3.2).

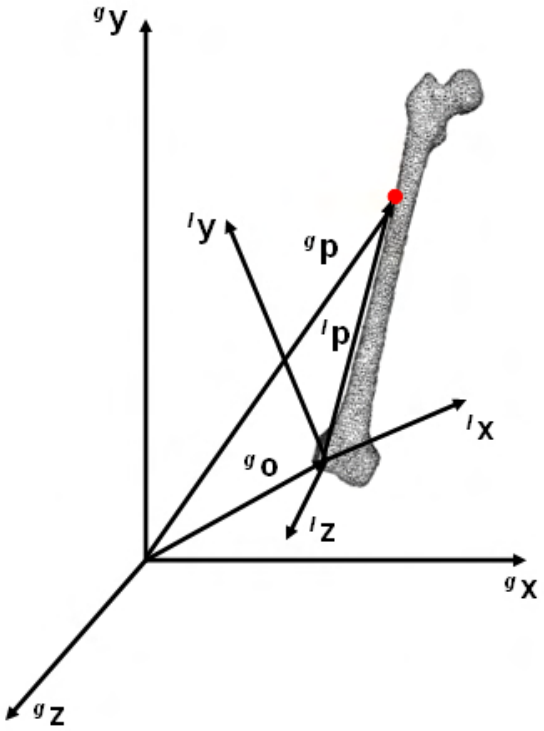

Figure 3.5: The position vector of a vertex represented in a global (${}^{g}x$, ${}^{g}y$, ${}^{g}z$) and a local frame (${}^{l}x$, ${}^{l}y$, ${}^{l}z$), indicated as ${}^{g}\mathbf{p}$ and ${}^{l}\mathbf{p}$, respectively.

3.4 Coordinate systems

As previously explained, the description of skeletal system movement involves the definition of specific sets of axes or local frames for each bone segment. These local frames are called anatomical frames (AF) and are designed specifically to meet the requirements of intra- and inter-subject repeatability. Moreover, their planes approximate the frontal, transverse and sagittal anatomical planes. This latter approximation permits a description of motion in clinical relevant terms (i.e., flexion/ extension, abduction/ adduction, internal/ external rotation), and makes the comparisons among researchers easier.

For the hip joint, we use definitions proposed by the Standardisation and Terminology Committee (STC) of the International Society of Biomechanics (ISB) [WSA+02]. The local axis system of each articulating bone is initially generated. This is achieved by setting a geometric rule that constructs the AF using selected anatomical landmarks (ALs) defined on the hip and femur bones [GS83] [WSA+02]. These axes then standardize the joint coordinate system. This procedure is detailed in the following sections:

3.4.1 Anatomical landmarks

In a human movement analysis using stereophotogrammetric measurements, ALs are located by external palpation [CCCL95] (CAST protocol, see Section 2.4.4). Then, the relevant AFs are computed through obvious geometric calculations and by using reconstructed positions of the ALs. This procedure raises a problem. Indeed, the ALs cannot be precisely determined because of overlying soft tissues or their mislocation [CLCC05] (i.e., no direct access to the bone is available).

Bones	**Right side**	**Left side**
Hip bone	• $\mathbf{ASIS_R}$: right anterior superior iliac spine • $\mathbf{PSIS_R}$: right posterior superior iliac spine • $\mathbf{HJC_R}$: right hip center of rotation (attached to the pelvis)	• $\mathbf{ASIS_L}$: left anterior superior iliac spine • $\mathbf{PSIS_L}$: left posterior superior iliac spine • $\mathbf{HJC_L}$: left hip center of rotation (attached to the pelvis)
	$\mathbf{midPSIS} = (\mathbf{PSIS_R} + \mathbf{PSIS_L})/2$: mid posterior superior iliac spine	
Femur	• $\mathbf{FE_{LR}}$: right femoral lateral epicondyle • $\mathbf{FE_{MR}}$: right femoral medial epicondyle • $\mathbf{FE_R} = (\mathbf{FE_{LR}} + \mathbf{FE_{MR}})/2$: midpoint of the right femoral epicondyle	• $\mathbf{FE_{LL}}$: left femoral lateral epicondyle • $\mathbf{FE_{ML}}$: left femoral medial epicondyle • $\mathbf{FE_L} = (\mathbf{FE_{LL}} + \mathbf{FE_{ML}})/2$: midpoint of the left femoral epicondyle

Table 3.1: Anatomical landmarks definition.

In this thesis, patient-specific 3D models of the hip joint are used and obtained from a segmentation's software developed at MIRALab [GMMT06] [Gil07] [SMT08]. They are reconstructed from a static MRI protocol as follows: from a MRI dataset of a healthy subject, an interactive segmentation was performed (this step was executed only once). The result of this segmentation is a collection of generic models of various soft (e.g., cartilages, muscles) and bony structures. For individualization, an automatic segmentation procedure is applied, equivalent to a Model to Image Registration. Generic models are deformed to match patients' unique anatomies. More details on the reconstruction method are given in [GMMT06] [Gil07] [SMT08]. The advantage of having such models is that we can define ALs directly on the 3D surfaces of the bones. The issue in the determination of ALs is thus solved. Moreover, when registering a generic model, shape constraints are applied to derive anatomical correspondences, in order for ALs to be automatically found from the generic ones. Hence, with the exception of the hip joint center (see Section 3.4.5), all parameters needed for bone coordinate system

computation are automatically obtained by storing generic AL positions on surfaces of the generic bone (barycentric coordinates).

Table 3.1 lists the ALs used for the AFs definition and Figure 3.6 shows the location of hip and femur bones ALs. All ALs and AFs are expressed in the global coordinate system (MRI scanner frame).

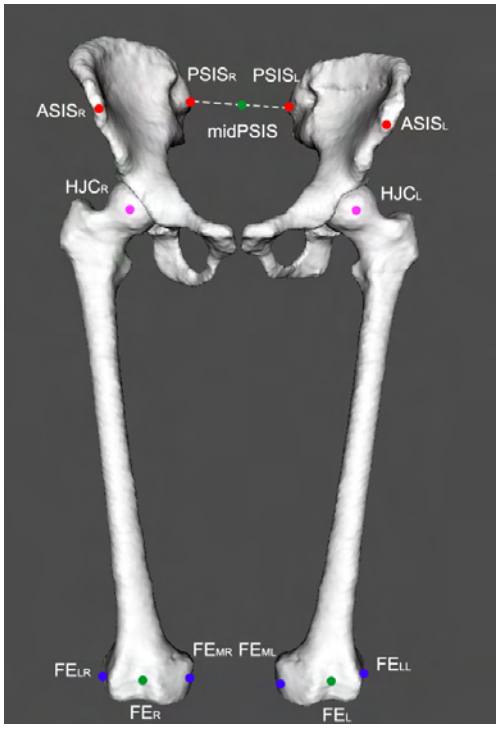

Figure 3.6: Location of hip and femur bones ALs.

3.4.2 Pelvic coordinate system

Using the definition of ALs in Section 3.4.1, we build the pelvic coordinate systems $\mathbf{SH_R}$ (right) and $\mathbf{SH_L}$ (left) accordingly (Table 3.2 and Figure 3.7):

- **O**: The origin coincident with the right (or left) hip center of rotation.
- **Z**: The line parallel to a line connecting the right and left ASISs, and pointing to the right.
- **X**: The line parallel to a line lying in the plane defined by the two ASISs and the midpoint of the two PSISs, orthogonal to the Z-axis, and pointing anteriorly.
- **Y**: The line perpendicular to both X and Z, pointing cranially.

Right side	Left side
$\mathbf{SH_R}$: • $\mathbf{O = HJC_R}$ • $\mathbf{Z} = \frac{\mathbf{ASIS_L ASIS_R}}{\|\mathbf{ASIS_L ASIS_R}\|}$ • $\mathbf{Y} = \frac{\mathbf{midPSISASIS_R \wedge midPSISASIS_L}}{\|\mathbf{midPSISASIS_R \wedge midPSISASIS_L}\|}$ • $\mathbf{X = Y \wedge Z}$	$\mathbf{SH_L}$: • $\mathbf{O = HJC_L}$ • $\mathbf{Z} = \frac{\mathbf{ASIS_L ASIS_R}}{\|\mathbf{ASIS_L ASIS_R}\|}$ • $\mathbf{Y} = \frac{\mathbf{midPSISASIS_R \wedge midPSISASIS_L}}{\|\mathbf{midPSISASIS_R \wedge midPSISASIS_L}\|}$ • $\mathbf{X = Y \wedge Z}$

Table 3.2: Pelvic coordinate system definition.

3.4.3 Femoral coordinate system

Using the definition of ALs in Section 3.4.1, we build the femoral coordinate systems $\mathbf{SF_R}$ (right) and $\mathbf{SF_L}$ (left) accordingly (Table 3.3 and Figure 3.7):

- **o**: The origin coincident with the right (or left) hip center of rotation, coincident with that of the pelvic coordinate system (**O**) in the neutral configuration.
- **y**: The line joining the midpoint between the medial and lateral FEs and the origin, and pointing cranially.
- **z**: The line perpendicular to the y-axis, lying in the plane defined by the origin and the two FEs, pointing to the right.
- **x**: The line perpendicular to both y- and z-axis, pointing anteriorly.

Right side	Left side
$\mathbf{SF_R}$: • $\mathbf{o = HJC_R}$ in neutral position • $\mathbf{x} = \frac{\mathbf{HJC_R FE_{LR} \wedge HJC_R FE_{MR}}}{\|\mathbf{HJC_R FE_{LR} \wedge HJC_R FE_{MR}}\|}$ • $\mathbf{y} = \frac{\mathbf{FE_R HJC_R}}{\|\mathbf{FE_R HJC_R}\|}$ • $\mathbf{z = x \wedge y}$	$\mathbf{SF_L}$: • $\mathbf{o = HJC_L}$ in neutral position • $\mathbf{x} = \frac{\mathbf{HJC_L FE_{ML} \wedge HJC_L FE_{LL}}}{\|\mathbf{HJC_L FE_{ML} \wedge HJC_L FE_{LL}}\|}$ • $\mathbf{y} = \frac{\mathbf{FE_L HJC_L}}{\|\mathbf{FE_L HJC_L}\|}$ • $\mathbf{z = x \wedge y}$

Table 3.3: Femoral coordinate system definition.

3.4.4 Joint coordinate system

The pelvic and femoral coordinate systems standardize the joint coordinate system as follows:

- $\mathbf{e_1}$: The axis fixed to the pelvis and coincident with the Z-axis of the pelvic coordinate system.
- $\mathbf{e_3}$: The axis fixed to the femur and coincident with the y-axis of the right (or left) femur coordinate system.
- $\mathbf{e_2}$: The floating axis, the common axis perpendicular to $\mathbf{e_1}$ and $\mathbf{e_3}$.

Joint angles are defined by rotations occurring about the three joint coordinate axes. Flexion/ extension is about the pelvic body fixed axis ($\mathbf{e_1}$). Internal/ external rotation is about the femoral body fixed axis ($\mathbf{e_3}$) and abduction/ adduction is about the floating axis ($\mathbf{e_2}$). Figure 3.7 and Table 3.4 illustrate and summarize for the reader the application of the joint coordinate system to the human hip.

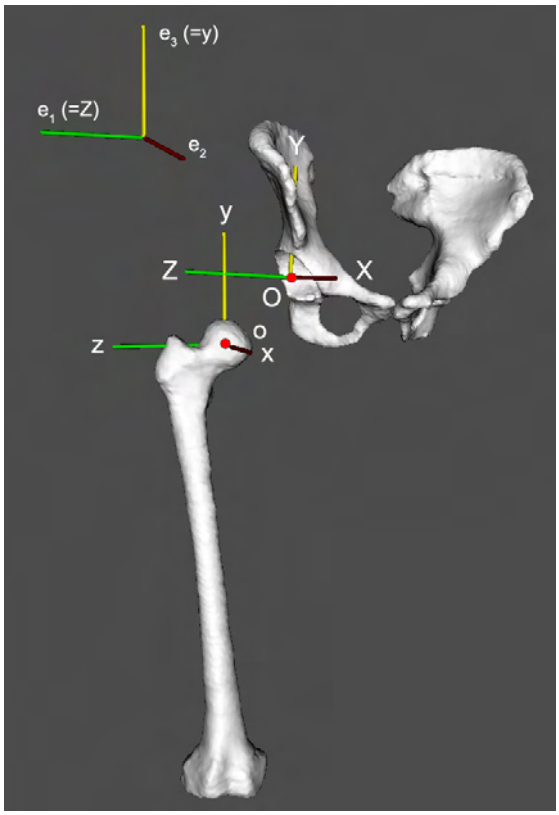

Figure 3.7: The pelvic coordinate system (XYZ), the femoral coordinate system (xyz), and the joint coordinate system ($e_1e_2e_3$) for the right hip joint.

$\mathbf{e_1} = \mathbf{Z_{pelvis}}$:

- Flexion/ extension $\alpha = \widehat{\mathbf{X_{pelvis}}\mathbf{e_2}}$: rotation around $\mathbf{e_1}$
- Mediolateral translation $\mathbf{q_1} = \mathbf{O_{pelvis}o_{femur}}.\mathbf{e_1}$: translation along $\mathbf{e_1}$

$\mathbf{e_3} = \mathbf{y_{femur}}$:

- Internal/ external rotation $\gamma = \widehat{\mathbf{x_{femur}}\mathbf{e_2}}$: rotation around $\mathbf{e_3}$
- Proximo-distal translation $\mathbf{q_3} = \mathbf{O_{pelvis}o_{femur}}.\mathbf{e_3}$: translation along $\mathbf{e_3}$

$\mathbf{e_2} = \mathbf{e_3} \wedge \mathbf{e_1}$:

- Adduction/ abduction $\beta = \pi/2 - \widehat{\mathbf{e_3}\mathbf{e_1}}$: rotation around $\mathbf{e_2}$
- Antero-posterior translation $\mathbf{q_2} = \mathbf{O_{pelvis}o_{femur}}.\mathbf{e_2}$: translation along $\mathbf{e_2}$

Table 3.4: Clinical rotations and translations in the human hip.

3.4.5 Hip joint center

The location of the hip joint center (HJC) is required to compute the joint coordinate system and to estimate hip joint rotations. In human movement analysis, the femoral head and acetabulum surface areas are assumed to have spherical shapes and a common center; therefore the hip is assumed to be a ball and socket joint. The HJC location can be estimated using two main approaches:

- The predictive approach [BPB90] [DOTG91] estimates the HJC as a relative position of ALs (static).
- The functional approach estimates the HJC from recorded [Cap84] [SD06] or simulated [KSMMT03] movements of the joint.

It has been reported that the functional approach is more accurate, since it accounts for joint dynamics [WSA+02]. However, hip ranges of motion are acquired using motion capture data, resulting in HJC estimation errors due to photogrammetric noise and soft tissue artifacts [CDC+09]. In this thesis, we compute the HJC based on a functional method, initially developed by [KSMMT03] and extended in [GKCMT+09]. The method entails the simulation of sole hip joint 3D models, reconstructed from MRI (see Section 3.4.1). An interesting idea in using patient-specific 3D models instead of generic rigid bodies ideally articulated, is that the hip joint is not considered as a perfect ball and socket any longer. Indeed, it has been reported that both the femoral head and the acetabulum are not strictly spherical [Men97]. The HJC is computed in two steps:

1. *Initialization*: The HJC is initialized with a geometrical approach (Figure 3.8a): the femoral head and the acetabulum are fitted with a sphere, where the points of interest (acetabulum/

femoral head) on the generic bones are manually selected to be automatically obtained from any individual models. Assuming a constant inter-articular distance (perfect ball and socket), the best estimate of the HJC is provided by extending the fitting process, which centers the two spheres on the same point [GKCMT+09].

2. *Functional approach*: The hip joint is simulated using a circumduction motion pattern (Figure 3.8b), while enforcing a constant inter-articular distance corresponding to the reference distance in the neutral posture. This type of motion was chosen, because it involves all types of rotations [KSMMT03]. Given the initialized HJC, an algorithm adjusts the center of rotation by testing points around the initial guess, the goal being to minimize hip/ femur bones collisions during the circumduction. The HJC is figured out as being the less moving femoral point in the pelvic frame.

The full description and validation of the method can be found in [Gil07] [GKCMT+09].

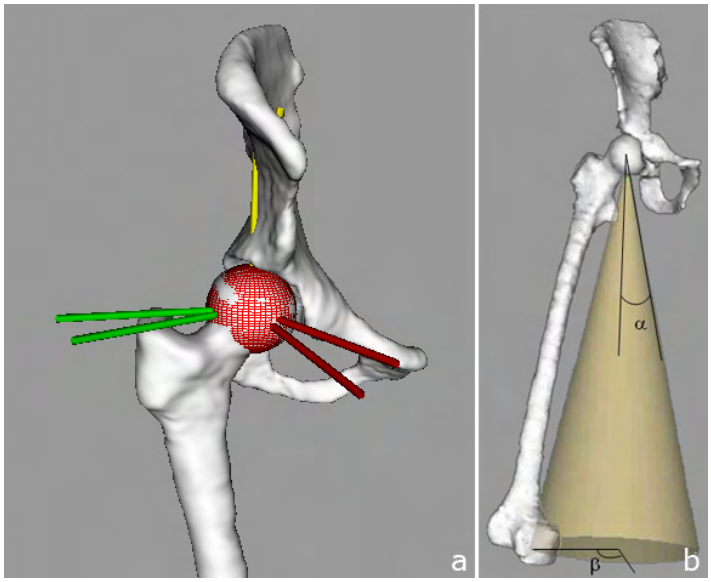

Figure 3.8: a) HJC initialization through spherical approximation b) Circumduction motion pattern of the hip, defined by the elevation α and the angle $0 \leq \beta < 2\pi$.

3.5 Clinical movements and range of motion of the hip joint

We have seen that hip joint angles are defined by rotations occurring about the three joint coordinate axes in the three anatomical planes (see Section 3.4.4). The flexibility of the hip joint is defined

by its range of motion (ROM). A joint's ROM is usually measured by the number of degrees from the neutral position of a segment to its position at the end of its full range of movement. In the clinical environment, the most common way to measure a joint's ROM is to use a double-armed goniometer. A stationary arm holding a protractor is placed parallel with a stationary body segment and a movable arm moves along a movable body segment. When anatomical landmarks are well palpable, the accuracy of measurement is greater. If there is more soft tissue surrounding the joint area, measurement errors are frequent. In the following sections, the hip ROMs have been gathered from [Kap96] and are given for a "normal" and untrained subject. Indeed, the hip ROM can be considerably increased with exercises and training.

3.5.1 Flexion/ extension

Flexion/ extension occurs in the sagittal plane about the mediolateral axis. The range of flexion varies according to different factors. Globally, the active flexion is smaller than the passive flexion. When the knee is extended, the flexion reaches 90°, while the flexion can reach or exceed 120° when the knee is bent. In the passive flexion, the range always exceeds 120°, but the knee again plays an important role: when it is bent, the flexion is much larger than when it is extended and can exceed 140°. The range of extension is notably smaller than for the flexion. The range varies from 10° to 20° for an active extension and from 20° to 30° for a passive extension. Both flexion and extension can be increased by training. For instance, dancers can easily perform the grand écart latéral (Figure 3.9a), regardless of ground support, thanks to the relaxation of their iliofemoral ligament.

Figure 3.9: a) Grand écart latéral b) Evaluation of the maximum hip flexion c) Evaluation of the maximum hip extension.

In order to evaluate the maximum flexion, the subject lays in supine position with the hip in neutral abduction/ adduction and rotation (Figure 3.9b). The maximum flexion is taken when the pelvis starts to rotate. For evaluating the maximum extension, the subject lays on the side with the hip in neutral abduction/ adduction and rotation (Figure 3.9c). Similarly to the flexion, the maximum

extension is reached when the pelvis rotates.

3.5.2 Abduction/ adduction

Abduction/ adduction occurs in the coronal plane about the antero-posterior axis. The range of active abduction is approximately 45°, while it reaches only 30° for adduction. Through training, it is possible to increase the maximum abduction. This is the case for dancers who can reach 60° or 65° of active abduction (i.e., with no support). For the passive abduction, they can reach 90° while being in grand écart facial (Figure 3.10a). However, this position is no longer a "pure" abduction, since the pelvis needs to tilt forward in order to relax the iliofemoral ligament. The hip is hence in abduction-flexion.

The maximum abduction/ adduction is evaluated with the subject in supine position, the hip being in neutral flexion/ extension and rotation (Figure 3.10b). The hip is abducted/ adducted and the maximum abduction/ adduction is reached when the pelvis starts to tilt or when there is a lateral flexion of the spine.

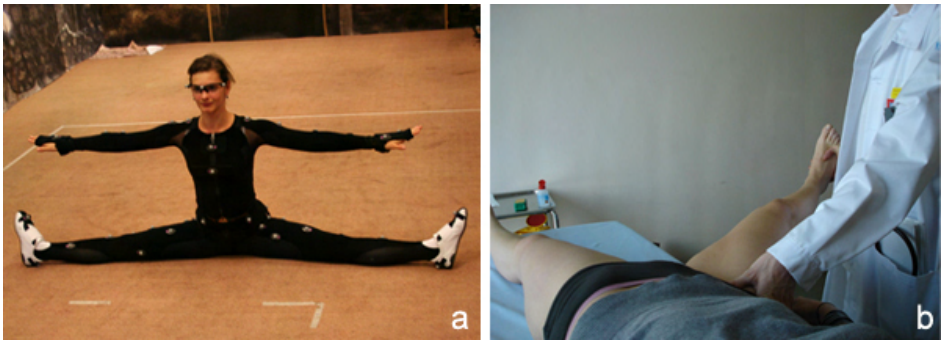

Figure 3.10: a) Grand écart facial b) Evaluation of the maximum hip abduction.

3.5.3 Internal/ external rotation

Internal/ external rotation occurs in the axial plane about the proximo-distal axis. When the knee is fully extended, external rotation is the movement that rotates the foot outward, while the internal rotation rotates the foot inward. The ROM is between 30° to 40° for internal rotation and 60° for external rotation. The rotation is freer when the hip is flexed rather than extended.

The maximum rotation is evaluated when the subject is sitting or lays in prone or supine position, with the knee bent at 90°. In supine position, the hip must be in neutral adduction/ abduction with

90° of flexion. The internal rotation is measured by rotating the foot outward (Figure 3.11a), while the external rotation is measured by rotating the foot inward (Figure 3.11b).

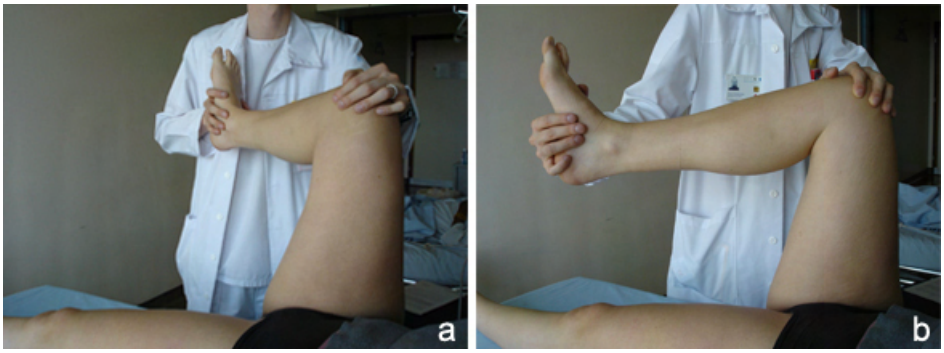

Figure 3.11: a) Evaluation of the maximum hip internal rotation b) Evaluation of the maximum hip external rotation.

3.6 Joint kinematics

In Section 3.3, we have demonstrated how to compute the instantaneous position and orientation of a bone segment and in Section 3.4, how to determine the respective local frames (or AFs) of the hip and femur bones. Now, we are interested in the description of the relative movement between these two contiguous bones. We consider the hip (H) and the femur (F) bones as being defined by a set of vertices $H = \{p_h \in \mathbb{R}^3\}$ and $F = \{p_f \in \mathbb{R}^3\}$, respectively. According to Equation (3.2), the position vectors of the hip and femur vertices, defined in their local frame, can be transformed in the global frame as:

$$ {}^{g}\mathbf{p}_h = {}^{g}\mathbf{R}_H \, {}^{l}\mathbf{p}_h + {}^{g}\mathbf{o}_H \tag{3.4} $$

$$ {}^{g}\mathbf{p}_f = {}^{g}\mathbf{R}_F \, {}^{l}\mathbf{p}_f + {}^{g}\mathbf{o}_F \tag{3.5} $$

Given the orientation matrices ${}^{g}\mathbf{R}_H$ and ${}^{g}\mathbf{R}_F$, and the position vectors ${}^{g}\mathbf{o}_H$ and ${}^{g}\mathbf{o}_F$ of the local frames associated with the two segments with respect to the global frame, the following expressions can be obtained:

$$ \mathbf{R}_{HF} = {}^{g}\mathbf{R}_H^T \, {}^{g}\mathbf{R}_F \tag{3.6} $$

$$ \mathbf{t}_{HF} = {}^{g}\mathbf{R}_H^T \, ({}^{g}\mathbf{o}_F - {}^{g}\mathbf{o}_H), \tag{3.7} $$

where $\mathbf{R}_{HF}$ referred to the joint orientation matrix, and $\mathbf{t}_{HF}$ to the position vector. These two quantities carry the full set of data for orientation and position (pose) of the femur relative to the hip bone and, thus, about joint kinematics. $\mathbf{R}_{HF}$ describes the joint orientation, taking as reference the

neutral orientation when the pelvic and femoral frames are aligned. In that case, $\mathbf{R}_{HF} = \mathbf{I}$ where $\mathbf{I}$ is the identity matrix.

The value of the scalar quantities in $\mathbf{R}_{HF}$ and $\mathbf{t}_{HF}$ depend on the pose of the pelvic and femoral frames used to derive them. Moreover, these quantities must be repeatable and expressed in clinical relevant terms. Thus, for each bone segment, a frame must be used that can be identified in a repeatable fashion. The AFs defined in Section 3.4 comply with this requirement. As a result, the joint position vector and orientation matrix should be calculated using Equation (3.6) and (3.7) and the relevant pelvic and femoral AFs.

In the following sections, we discuss about the nature of $\mathbf{t}_{HF}$ and $\mathbf{R}_{HF}$. Then, we describe how rigid body motion and AFs can be formulated with 4×4 homogeneous transformation matrices and thus, how the joint kinematics can be calculated through a succession of matrix transformations.

3.6.1 Translational degrees of freedom

The relative position between the hip and femur bones is described by making reference to the vector $\mathbf{t}_{HF}$ joining a point defined in each of the pelvic (Q_h) and the femoral frames (Q_f) (Figure 3.12). For the sake of the already-mentioned repeatability issue, these reference points are chosen so as to coincide with the origins of the two frames, namely the hip joint center (HJC). The vector $\mathbf{t}_{HF}$ thus provides numerical information about joint subluxation.

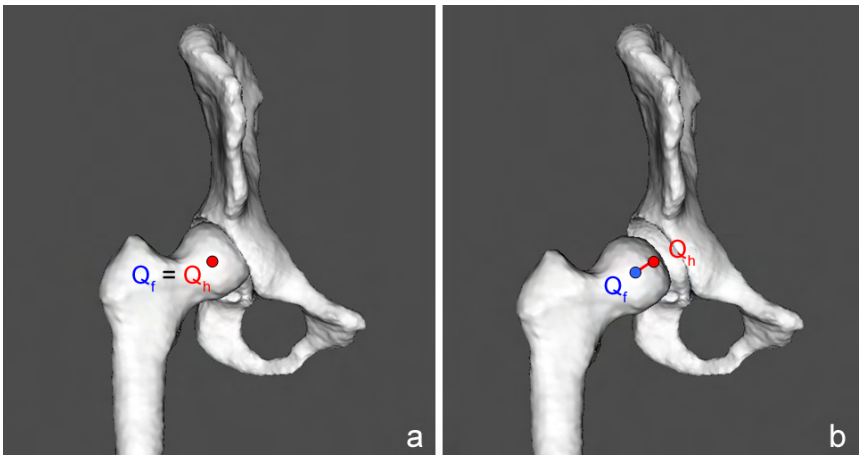

Figure 3.12: The points defined in the pelvic (Q_h) and in the femoral frames (Q_f) used to describe the joint translational degrees of freedom: a) the translation is null and the two points coincide b) the translation denotes a subluxation.

3.6.2 Rotational degrees of freedom

The relative orientation between the hip and femur bones, expressed in clinical relevant terms, can be deduced by the decomposition of the joint orientation matrix ($\mathbf{R}_{HF}$) into three successive rotations. Assuming that the pelvic coordinate system is denoted by $\{XYZ\}$ and that the femoral coordinate system is denoted by $\{xyz\}$ according to the ISB notations [WSA+02], if the femur is rotated by an angle α about the X or x axis, then the relevant orientation matrix is:

$$\mathbf{R}_{HF\alpha} = \begin{bmatrix} 1 & 0 & 0 \\ 0 & \cos\alpha & -\sin\alpha \\ 0 & \sin\alpha & \cos\alpha \end{bmatrix} \tag{3.8}$$

Similarly, the orientation matrices obtained from rotations about the Y or y axis (β) and about the Z or z axis (γ) are given respectively by:

$$\mathbf{R}_{HF\beta} = \begin{bmatrix} \cos\beta & 0 & \sin\beta \\ 0 & 1 & 0 \\ -\sin\beta & 0 & \cos\beta \end{bmatrix} \tag{3.9}$$

$$\mathbf{R}_{HF\gamma} = \begin{bmatrix} \cos\gamma & -\sin\gamma & 0 \\ \sin\gamma & \cos\gamma & 0 \\ 0 & 0 & 1 \end{bmatrix} \tag{3.10}$$

These matrices are referred to as basic rotation matrices [KLL83] [FGL88] and could be performed with different axes sequences. Several conventions exist in the literature to define the sequence order. In this thesis, we follow the ISB recommendations [WSA+02] in our investigations for the hip joint. The chosen sequence of basic rotations is consistent with the so-named Grood and Suntay's convention [GS83] and rotations occurs, first, around the Z axis, second, around the floating axis e_2 (the axis orthogonal to both the Z and the y axis, see Section 3.4.4), and third, around the y axis. It is worth mentioning that when the second rotation occurs, the floating axis e_2 coincides with the x axis.

Using this sequence of basic rotations, the joint orientation matrix may be obtained based on the following rules [FGL88]:

- If a rotation occurs about an axis of the *proximal* frame, the previous orientation matrix must be *pre-multiplied* with the appropriate basic rotation matrix.
- If a rotation occurs about an axis of the *distal* frame, the previous orientation matrix must be

post-multiplied with the appropriate basic rotation matrix.

Hence, the joint orientation matrix is:

$$\mathbf{R}_{HF} = \{[(\mathbf{R}_{HF\gamma}\mathbf{I})\mathbf{R}_{HF\alpha}]\,\mathbf{R}_{HF\beta}\} \tag{3.11}$$

which can be written as:

$$\begin{bmatrix} r_{11} & r_{12} & r_{13} \\ r_{21} & r_{22} & r_{23} \\ r_{31} & r_{32} & r_{33} \end{bmatrix} = \begin{bmatrix} \cos\gamma\cos\beta - \sin\gamma\sin\alpha\sin\beta & -\sin\gamma\cos\alpha & \cos\gamma\sin\beta + \sin\gamma\sin\alpha\cos\beta \\ \sin\gamma\cos\beta + \cos\gamma\sin\alpha\sin\beta & \cos\gamma\cos\alpha & \sin\gamma\sin\beta - \cos\gamma\sin\alpha\cos\beta \\ -\cos\alpha\sin\beta & \sin\alpha & \cos\alpha\cos\beta \end{bmatrix} \tag{3.12}$$

From this system of equations the angles α, β and γ can be obtained as:

$$\alpha = \arcsin r_{32}, \tag{3.13}$$

$$\beta = \arcsin\left(\frac{-r_{31}}{\cos\alpha}\right), \tag{3.14}$$

$$\gamma = \arcsin\left(\frac{-r_{12}}{\cos\alpha}\right). \tag{3.15}$$

The angles α, β and γ represent the amount to which the hip is abducted or adducted, internally or externally rotated, and flexed or extended, respectively, relative to the reference aligned orientation.

3.6.3 Homogeneous transformation matrices

Standard 3D geometric transformations can be formulated with 4×4 homogeneous transformation matrices. These matrices are computed from the minimal set of transformation parameters, through successive basic transformations (e.g., rotation around one axis, shift in one direction, etc.). A homogeneous transformation matrix is given by the generic equation:

$$\mathbf{M} = \begin{bmatrix} & \mathbf{R}_{3\times3} & & \mathbf{T}_{3\times1} \\ 0 & 0 & 0 & 1 \end{bmatrix} \tag{3.16}$$

where $\mathbf{R}_{3\times3}$ is the rotation submatrix and $\mathbf{T}_{3\times1}$ is the translation vector. For example, the position vectors $\mathbf{p}$ of the vertices of a bone segment can undergo a transformation $\mathbf{M}$ as: $\mathbf{p}' = \mathbf{M}\mathbf{p}$, with $\mathbf{M}^T\mathbf{M} = \mathbf{I}$. This latter constraint ensures that the transformation is orthogonal, corresponding to a rigid body motion.

Homogeneous matrices offer certain computational advantages. First, they treat both translations and rotations in a uniform way. Second, they can be concatenated, such that complex kinematic relationships can be modeled. Finally, they are easily invertible as in:

$$\mathbf{M}^{-1} = \begin{bmatrix} & \mathbf{R}^T & & -\mathbf{R}^T \cdot \mathbf{T} \\ 0 & 0 & 0 & 1 \end{bmatrix} \tag{3.17}$$

Orthonormal bone systems (AFs) can also be converted into 4×4 homogeneous transformation matrices. Indeed, the three unit vectors **i**, **j** and **k** which form the basis for the bone coordinate system each consists of 3 coordinates, yielding a total of 9 parameters. These parameters can be written as the elements of a 3×3 submatrix **DCM**, called the direction cosine matrix. The origin (o) of the bone coordinate system completes the 4×4 matrix **S** as:

$$\mathbf{S} = \begin{bmatrix} & \mathbf{DCM}_{3\times3} & & o_x \\ & & & o_y \\ & & & o_z \\ 0 & 0 & 0 & 1 \end{bmatrix} = \begin{bmatrix} i_x & j_x & k_x & o_x \\ i_y & j_y & k_y & o_y \\ i_z & j_z & k_z & o_z \\ 0 & 0 & 0 & 1 \end{bmatrix} \tag{3.18}$$

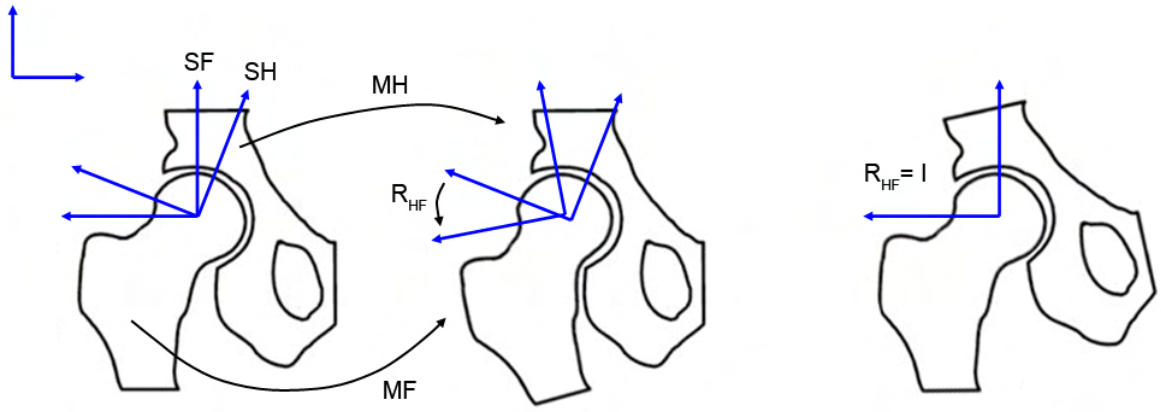

Figure 3.13: Bone and joint transforms in the reference (MRI acquisition) pose (left), in a user pose (middle) and in the neutral pose (right).

Using the above matrix expressions, the orientation and position of the femur relative to the hip bone can be calculated through a succession of matrix transformations. By linking the different transforms

in the global frame (in our case, the MRI scanner frame), here are the different relationships:

$$\mathbf{R}_{HF} = \left\{ \mathbf{SH}^{-1} \left[\mathbf{MH}^{-1} (\mathbf{MF}\,\mathbf{SF}) \right] \right\} \tag{3.19}$$

$$\mathbf{R}_{HF} = \mathbf{R}_{HF}^{-1} \tag{3.20}$$

Bone global transforms are denoted by $\mathbf{M}$, bone systems by $\mathbf{S}$ and joint relative transform by $\mathbf{R}_{HF}$, as shown in Figure 3.13. Standard medical angles and shifts can then be easily determined from $\mathbf{R}_{HF}$.

3.6.4 Global vs. relative transformations

The movement of a bone segment is defined by the computation of its successive poses for each sampled time instant. This computation can be performed in two different manners (Figure 3.14):

- *Global transformations*: The bone segment is transformed for each sampled time instant by the global homogeneous transform $\mathbf{M}$, corresponding to the transformation from the reference (MRI acquisition) pose t_0 to the current pose t_i.
- *Relative transformations*: The bone segment is transformed for each sampled time instant by the relative homogeneous transform $\mathbf{Mrel}$, corresponding to the transformation from the pose t_{i-1} to the current pose t_i.

The global transforms of a bone segment being known, its relative transform at time t_i can be obtained as:

$$\mathbf{Mrel}_{t_i} = \mathbf{M}_{t_{i-1}}^{-1} \mathbf{M}_{t_i} \tag{3.21}$$

Conversely, the relative transforms of a bone segment are known, its global transform at time t_i can be computed recursively as:

$$\mathbf{M}_{t_i} = \mathbf{Mrel}_{t_1} \mathbf{Mrel}_{t_2} \ldots \mathbf{Mrel}_{t_i} \tag{3.22}$$

Figure 3.14 illustrates these relationships. It is important to note that the two computation methods are equivalent. In this thesis, the motion of the hip and femur bones are estimated using relative transformations. However, bone global transforms are necessary to compute the joint kinematics, according to Equation (3.19).

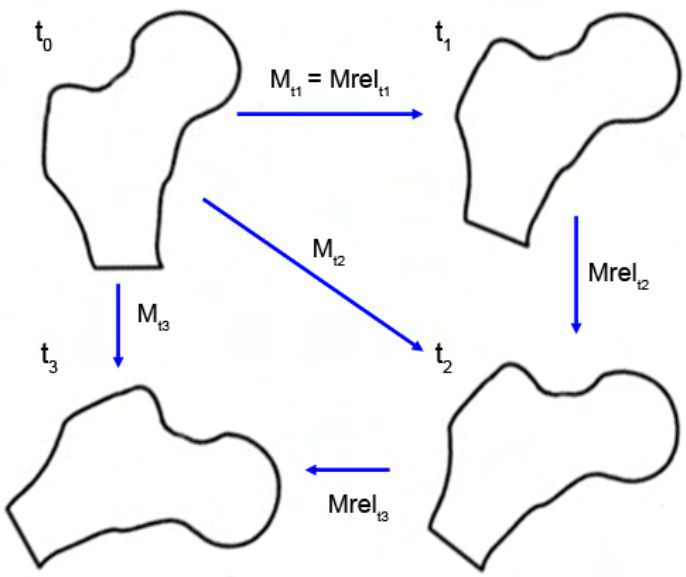

Figure 3.14: Global vs. relative bone transforms: t_0 refers to the reference (MRI acquisition) pose, t_1, t_2 and t_3 to successive user poses.

3.7 Conclusion

In this chapter, we have reviewed the theoretical foundations related to the motion study of the hip joint. We have presented the methods (localization of anatomical landmarks, construction of bones and joint coordinate systems, and computation of hip joint center) adopted in this thesis to report joint motion in an intra- and inter-subject repeatable way, and we have described the anatomy of the hip joint and its physiology (clinical movements, ROMs). Before studying and analyzing the hip joint, it is essential to understand the theory behind joint kinematics. We have seen that to proceed to the description of hip joint kinematics during the execution of a motor task, the following procedure must be implemented:

- Determination of the anatomical landmarks positions used for defining the pelvic and femoral coordinate systems.
- Identification of the hip joint center used for the numerical interpretation of translational degrees of freedom.
- Computation of the femur and hip bone individual motion (segmental kinematics).
- Computation of the orientation and position of the femur relative to the hip bone:
  - Either by determining the joint position vector $\mathbf{t}_{HF}$ and orientation matrix $\mathbf{R}_{HF}$ using Equation (3.6) and (3.7),

– or by determining the homogeneous transformation matrix $\mathbf{R}_{HF}$ using Equation (3.19).

With reference to this procedure, the main issue remains the determination of bone poses for each sampled instant of time. In this work, this is actually done by estimating the movement of the hip and femur bones from motion capture data where soft tissue artifacts must be reduced, in order to compute the best rigid transforms of each bone segment. This matter will be dealt with in the coming chapter.

Chapter 4

Hip joint kinematics estimation

[1]Pietro da Cortona, 1596-1669. Tabulae anatomicae a celeberrimo pictore Petro Berrettino, Romae: Impensis Fausti Amidei, Ex typographia Antonii de Rubeis, p. 81, pl. XXVI, 1741. Collection Léo-Pariseau. Bibliothèque des livres rares et collections spéciales, Université de Montréal. Image from `http://www.bib.umontreal.ca/CS/livre-savant/renaissances/fiches/cortone05.htm` used by permission.

4.1 Introduction

In this chapter, we expose our methodology to estimate the movement of the hip and femur bones using optical motion capture and 3D body scanning, while minimizing the effect of soft tissue artifacts (STA) and the errors of calibration. This embraces the different steps of the process: the motion recording phase where an appropriate markers protocol is defined, the anatomical calibration phase where the correspondence between anatomical and motion frames is established, and the bone pose computation phase where the best rigid transforms of each bone segment are computed. The sections in this chapter are organized to reflect these different phases: first, we explain how a typical motion capture session takes place. In this phase, many inaccuracies can occur such as errors in system calibration, the choice of an inappropriate markers configuration or post-processing failures. Thus, special attention is devoted to avoid these errors during and after the motion capture session. Second, we present our method [MTCS08] [CAVMT09] to calibrate the anatomy. To perform this step, we use the 3D body scanning technology and we exploit geometric features of the 3D models to automate most of the process. Third, we introduce our bone pose estimation technique [CLMT08] [CAVMT09] [CSKC$^+$09]. Thanks to our optimized fitting algorithm which accounts for STA and anatomical constraints, the motion of the hip is accurately and robustly estimated from the skin markers. Eventually, we introduce some additional developments made during this thesis work.

4.2 Motion capture

Our optical motion capture system is a Vicon[1] MX 13i from Oxford Metrics (UK), composed of 8 wall-mounted infrared cameras. Vicon is an optical detection system, which means that information is transferred to the computer without the need of any cabling. The only limitation is the area in which the subject can move. The cameras can only "see" a certain amount of space. Of course, this depends on the size of the room, the placement and the number of cameras used. Our current capture volume is $45.3m^3$ (3.6 x 4.2 x $3m$).

For body motion capture, the system tracks reflectors placed on the subject's body. These markers are small spheres covered with a reflective tape. They act as mirrors and appear much brighter to the cameras than the rest of the scene. Each camera emits infrared light. This light wave hits the reflector, which sends it back to the camera. The camera records the information about its position in the 2D image and sends it to the computer. The 2D data from each camera are combined with the camera coordinates and other camera's views to obtain the 3D coordinates of each marker for each

[1] `http://www.vicon.com/`, accessed November 2009

instant frame.

The typical production pipeline for optical motion capture begins with the definition of the markers configuration. Then, the system and subject need to be calibrated. Finally, motion recording can start. These different steps are detailed in the following sections.

4.2.1 Markers configuration

The choice of the markers configuration is important, since STA depends on the marker location variability (e.g., location in segment, number) [CLCC05] [LCCC05]. The studies assessing STA show that the magnitude of the STA is bigger in areas closer to the joints (see Section 2.3). Non redundant markers also increase its effect. Therefore, our strategy is to define a markers protocol including redundant markers distributed all over the pelvic and femoral surfaces and located as far as possible from the joint line. However, overabundance of markers can lead to difficulties in tracking and marker's labeling. Hence, a trade-off between the number of markers and technical constraints has been done.

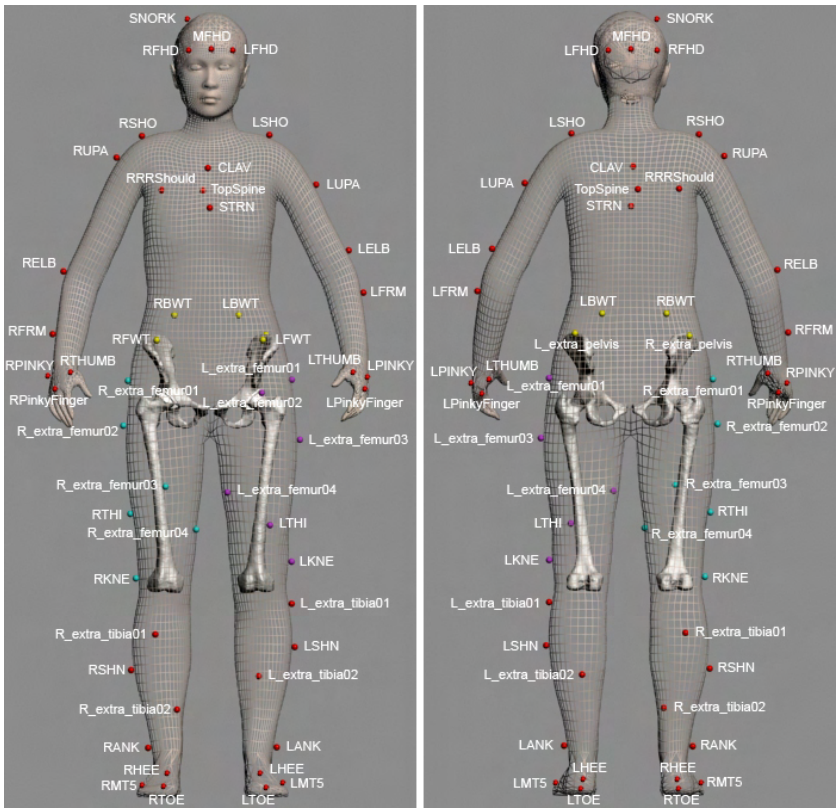

Figure 4.1: Markers position on the subject's body (front and back views).

To capture the hip joint kinematics, we use two clusters of six $7mm$ spherical markers affixed onto the lateral and frontal parts of both thighs and six markers onto the pelvis. As our plan is to record dancers while performing extreme movements that sometimes require the ground support (e.g., split), these skin markers are arranged to ensure their visibility to the cameras throughout the range of motion. Moreover, both legs have an asymmetric markers setup to avoid marker's recognition errors by the system. Additional reflective markers are distributed over the body to confer a more complete visualization from general to detailed. To this end, the marker set utilized here is the one traditionally used for motion capture in the animation field, except for the shanks where two additional markers are attached to each segment (L_extra_tibia01, L_extra_tibia02, R_extra_tibia01, R_extra_tibia02). The markers configuration defined in this thesis is illustrated in Figure 4.1 and detailed in Table 4.1.

No.	**Name**	**Segment**	**Setup**
1	SNORK	Head	Animation
2	RFHD	Head	Animation
3	MFHD	Head	Animation
4	LFHD	Head	Animation
5	TopSpine	Thorax	Animation
6	STRN	Thorax	Animation
7	CLAV	Thorax	Animation
8	RRRShould	Thorax	Animation
9	LSHO	Left clavicle	Animation
10	LUPA	Left humerus	Animation
11	LELB	Left humerus	Animation
12	LFRM	Left cubitus/radius	Animation
13	LTHUMB	Left hand	Animation
14	LPINKY	Left hand	Animation
15	LPinkyFinger	Left hand	Animation
16	RSHO	Right clavicle	Animation
17	RUPA	Right humerus	Animation
18	RELB	Right humerus	Animation
19	RFRM	Right cubitus/radius	Animation
20	RTHUMB	Right hand	Animation

No.	Name	Segment	Setup
21	RPINKY	Right hand	Animation
22	RPinkyFinger	Right hand	Animation
23	RFWT	Pelvis	Medical (own setup)
24	LFWT	Pelvis	Medical (own setup)
25	RBWT	Pelvis	Medical (own setup)
26	LBWT	Pelvis	Medical (own setup)
27	L_extra_pelvis	Pelvis	Medical (own setup)
28	R_extra_pelvis	Pelvis	Medical (own setup)
29	L_extra_femur01	Left femur	Medical (own setup)
30	L_extra_femur02	Left femur	Medical (own setup)
31	L_extra_femur03	Left femur	Medical (own setup)
32	L_extra_femur04	Left femur	Medical (own setup)
33	LTHI	Left femur	Medical (own setup)
34	LKNE	Left femur	Medical (own setup)
35	L_extra_tibia01	Left tibia	Medical (own setup)
36	LSHN	Left tibia	Animation
37	L_extra_tibia02	Left tibia	Medical (own setup)
38	LANK	Left tibia	Animation
39	LHEE	Left foot	Animation
40	LTOE	Left toes	Animation
41	LMT5	Left foot	Animation
42	R_extra_femur01	Right femur	Medical (own setup)
43	R_extra_femur02	Right femur	Medical (own setup)
44	R_extra_femur03	Right femur	Medical (own setup)
45	RTHI	Right femur	Medical (own setup)
46	R_extra_femur04	Right femur	Medical (own setup)
47	RKNE	Right femur	Medical (own setup)
48	RSHN	Right tibia	Animation
49	R_extra_tibia01	Right tibia	Medical (own setup)
50	R_extra_tibia02	Right tibia	Medical (own setup)

No.	Name	Segment	Setup
51	RANK	Right tibia	Animation
52	RHEE	Right foot	Animation
53	RTOE	Right toes	Animation
54	RMT5	Right foot	Animation

Table 4.1: Markers configuration used in this thesis.

4.2.2 Calibration of the system

Before starting any movement recording, the system needs to be calibrated. This is an essential step, as it plays a considerable role in minimizing instrumental errors in the resulting data. It measures the position and orientation of the capture volume and the location of each camera relative to the others. This information is used by the Vicon software when recreating the 3D coordinates with the 2D data sent by the different cameras.

System calibration involves two steps. First, the static calibration sets and locates the origin and the directions of the global axes of the motion capture space. To this end, a L-FRAME made of four markers is used to materialize the motion capture coordinates system (Figure 4.2a). Second, the dynamic calibration allows the system to calculate the relative positions and orientations of the cameras. A WAND with three markers is used to record a dynamic sequence while it is waved around by the operator to cover the whole volume (Figure 4.2b).

4.2.3 Calibration of the subject

It is necessary to introduce the subject to the Vicon system. For this calibration, the subject is positioned in a T-posture and the system records the associated markers positions. Then, a dynamic sequence is recorded while the subject performs a range of motion. Those two sequences are used by the operator to label all the markers and build a subject marker calibration file that comprises geometrical and statistical data about markers positions. The information gathered at this stage is used by the system to label the trajectories automatically during the post-processing of dynamic movements.

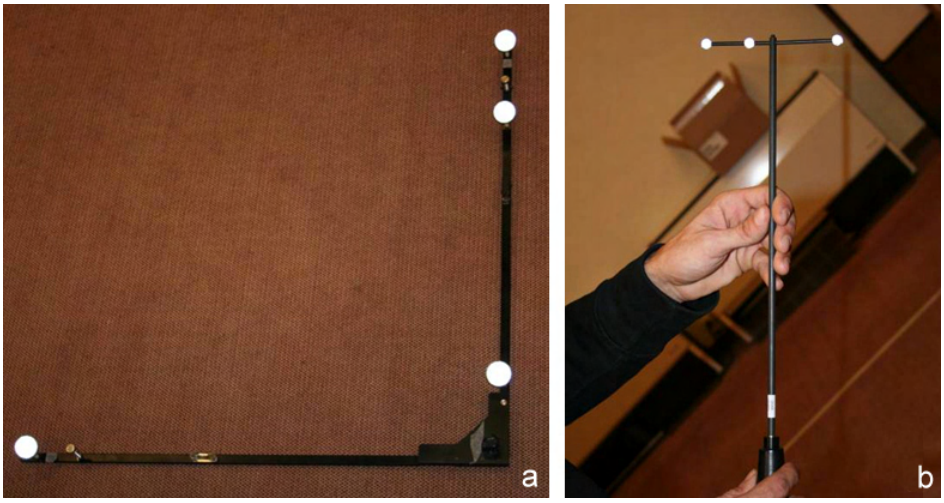

Figure 4.2: Calibration of the Vicon system: a) L-FRAME b) WAND.

4.2.4 Motion tracking and post-processing

Once all the calibrations have been done, movements can be captured. Data are acquired with a sampling of $120Hz$. During the post-processing phase, an automated labeling procedure is performed, followed by manual labeling corrections when needed. For the automated labeling procedure, the Vicon software relies on the information that exists in the calibrated model (see previous Section). Data are also filtered (Butterworth filtering) to remove unwanted high frequency noise of vibrations, whilst keeping all the original nuances and subtleties of the captured motion. No interpolation models are used to fill gaps in the trajectories. The markers motion reconstruction has an accuracy of less than $0.5mm$. Eventually, the markers trajectories are exported to a standard *.csm* file to be used in our application.

4.3 Anatomical calibration

The relative position of the skin markers with respect to the underlying bones is unknown. Before converting markers trajectories into animation, an anatomical calibration is therefore required to put in correspondence anatomical and motion frames (i.e., movement/ morphology data registration). This calibration entails the localization of the bone segments in the marker cluster technical frame (CTF). To perform this step, most kinematic studies use a number of calibrated external anatomical landmarks (ALs) identified in the CTF by placing a marker on them or by using a pointer mounting two markers in known position [CCCL95] (CAST protocol, see Section 2.4.4). However, this protocol lacks accuracy and precision in the determination of ALs, due to the overlying soft tissues or to AL

misplacement [CLCC05]. Therefore, our idea is to combine MRI and 3D body scan information to have a better approximation thanks to markers positions on the skin. Our calibration process [MTCS08] [CAVMT09] is summarized as follows:

1. After motion recordings, the subject undergoes a 3D body scan with the markers still in place to retrieve his/ her exact external body surface.
2. The positions of the skin markers are identified on the resulting body scan data.
3. A registration method is used to conform the body scan mesh and the extracted markers positions to the patient-specific skin segmented from MR images. This pose determines a calibration frame.

We propose to detail this calibration procedure in the next sections. In Section 4.3.6, we will also validate it.

4.3.1 3D body scanning

The first step of our calibration procedure consists in digitalizing an accurate skin model of the complete subject's body. This acquisition is achieved with a Vitus Pro[1] scanner from Vitronic (Germany). The subject is scanned with the same skin markers used for motion capture (Figure 4.3a).

The Vitus system uses the laser light stripe method (or laser triangulation method) for 3D profile scanning and surface reconstruction [D'A06]. The light source used within this process comprises a laser light source in combination with a cylindrical lens. A video camera is positioned at a defined angle to the light source. The light line, imaged on the body, is located in the view field of the camera and is offset and deflected in accordance with the different heights of the body. The angle between the camera and the light source (triangulation angle W) determines the magnitude of the offset and the deflection. As angle W is given, the shape of the body at the respective line position can be determined by means of a simple measurement and a profile section can be generated. If the sensor (the diode laser and the CCD matrix video camera) is moved over the body and profile sections are generated simultaneously, a point cloud of the outer contour of the body is produced (Figure 4.3b). The scanner has an accuracy of $\sim 1mm$. One scan of the complete body lasts ~ 15 seconds.

[1] `http://www.vitronic.de/en/bodyscannen/complete-body-scanning/`, accessed November 2009

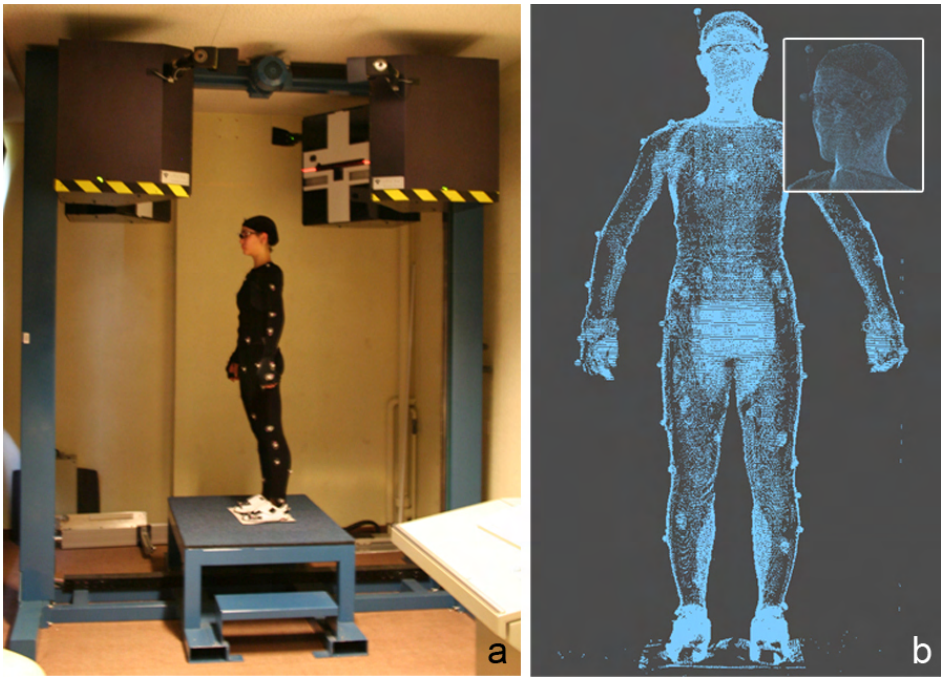

Figure 4.3: 3D body scanning: a) subject scanned with the skin markers b) resulting point cloud.

4.3.2 Markers extraction

The second step of our calibration procedure involves the identification and determination of the markers positions on the resulting point cloud from the 3D body scanner. The objective is to extract spherical patterns from a very high number of points ($\sim$ 250 K points). This process is challenging because the data are noisy (see Figure 4.3b). Moreover, the point cloud is unstructured, so that there exists no meaningful relationship between points. To extract the position of these markers, we have developed the following semi-automatic procedure:

It is possible to find the best sphere fitting to a set of points by least-squares fitting of data [SE03]. First, we manually select from the raw dataset a point which belongs to the surface of the marker (Figure 4.4a). The points of interest are then automatically selected within an area of $2R$, considering the picked point as the center of a sphere and R as the radius (Figure 4.4b). In practice, $R = 0.007$ because the marker has a radius of $7mm$. Given these points of interest $\{P_i \in \mathbb{R}^3\}$, the goal is now to fit them with a sphere (Figure 4.4c). The function to minimize is given by:

$$\sum_{i<n} (\|\mathbf{P_i C}\| - r)^2 \tag{4.1}$$

where $\mathbf{C}$ is the center of the marker and r its radius. Setting the function derivatives with regards to

$\mathbf{C}$ and r, we obtain the following iterative process that quickly converges:

$$r_j = \frac{1}{n} \sum_i \|\mathbf{P_i C_j}\| \tag{4.2}$$

$$\mathbf{C_{j+1}} = \mathbf{C_0} + \frac{r_j}{n} \sum_i \frac{\mathbf{P_i C_j}}{\|\mathbf{P_i C_j}\|} \tag{4.3}$$

with

$$\mathbf{C_0} = < \mathbf{P_i} >_i = \frac{1}{n} \sum_i \mathbf{P_i} \tag{4.4}$$

Finally, the farthest points from $\mathbf{C}$ are considered as outliers and are removed during a refinement process.

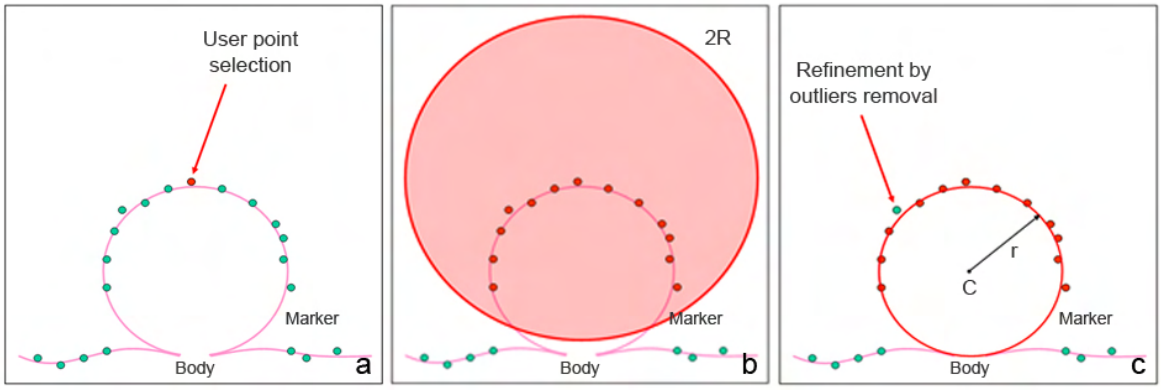

Figure 4.4: Markers extraction procedure: a) user point selection b) automatic selection of the points of interest c) sphere fitting and outliers removal.

This procedure is repeated for each marker. They are selected according to the labeling's order used for motion capture. As a result, markers are labeled (Figure 4.5) and their positions are stored for the next calibration step.

4.3.3 Body scan model post-processing

Before registration (third step of our calibration procedure, see Section 4.3.5), the scan data need to be post-processed. First, disturbing noise is removed from the space around the scan (purification) and from the scan surface (smoothing). Then, the point cloud is triangulated. These operations are achieved using the scanner's software (ScanWorx 2.7). The generated scan model contains a large number of polygons ($\sim$ 500 K polygons), which is unacceptable for a real-time application (indeed,

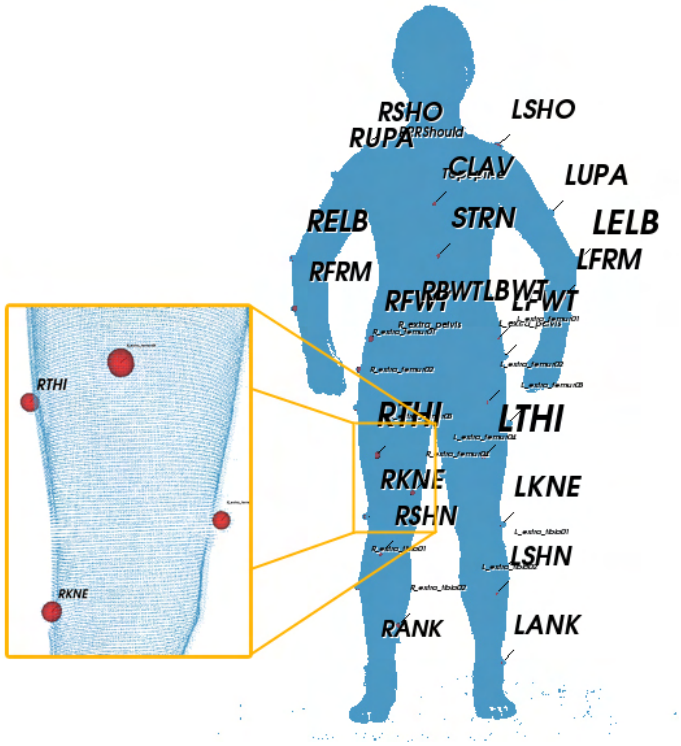

Figure 4.5: Markers extraction results.

we wish to animate the mesh during motion, see Section 4.5). Hence, the model must be simplified to reduce the computational burden.

In order to simplify the mesh and to establish correspondences among the models, the scan model is accurately fitted to a generic body model [SMT03] (Figure 4.6). After this fitting process, each model includes the same number of vertices (10'724 vertices, 21'215 polygons) and connectivity in the mesh. Using the same generic model to generate all the scan data makes the feature correspondence among the scan data trivial. Feature correspondence is later used for registration.

4.3.4 MRI skin model pre-processing

Using the MRI scans of the subject, a patient-specific 3D model of the skin is generated [Gil07]. As mentioned in Section 3.4.1, these 3D models are reconstructed using a segmentation method that deforms a generic model to match the patient's unique anatomy (i.e., Model to Image Registration). The power of using and registering generic shapes lies in the obtention of exact geometric correspondences, and thus morphological features have the same vertex indexes across individual models. The

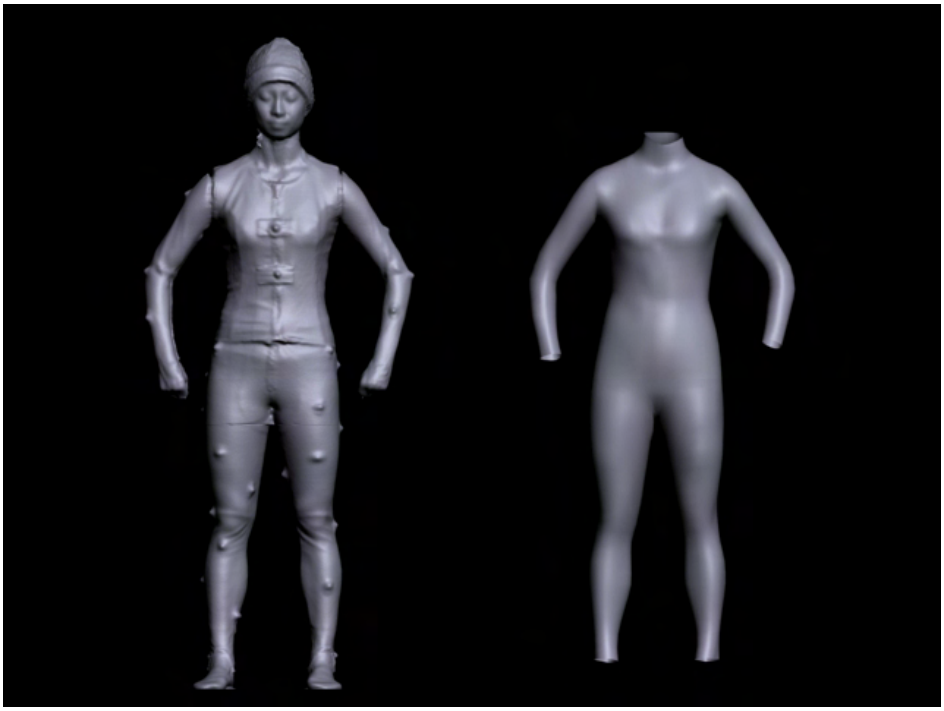

Figure 4.6: Original scan model (left) and corresponding generic body model after fitting (right).

part of the skin modeled includes the pelvis and the femur, because we are limited by the MRI volume boundaries. This skin model is a closed surface generated for each leg (Figure 4.7).

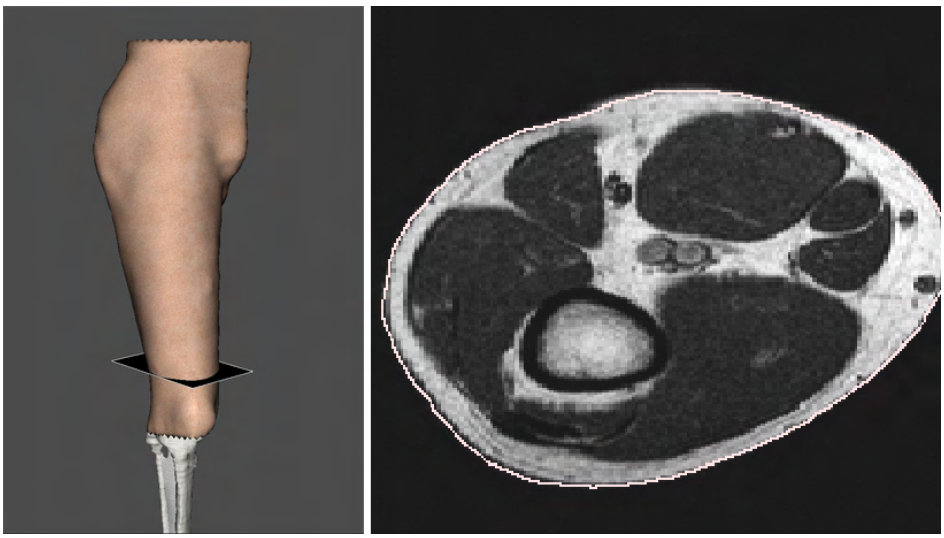

Figure 4.7: Skin model generated from MRI.

As for the body scan model, we need to prepare the skin model before registration. If we merge the skin models of each leg, we obtain a single mesh with overlapping surfaces and internal body points (Figure 4.8a). This will disturb our registration algorithm, which will be detailed in the next section. The goal of this pre-processing phase is hence to produce a mesh without these undesirable points. We select them on the generic skin to automatically obtain them from any individual models (Figure 4.8b). Using the points as input, a clipping filter is then applied to the skin model (Figure 4.8c). This filter allows us to "cut" through the cells of the model, the input points being the points to be removed by the cutting algorithm. Finally, the two skin models are merged together (Figure 4.8d). This pre-processing phase runs fully automatically while loading the skin models in our application.

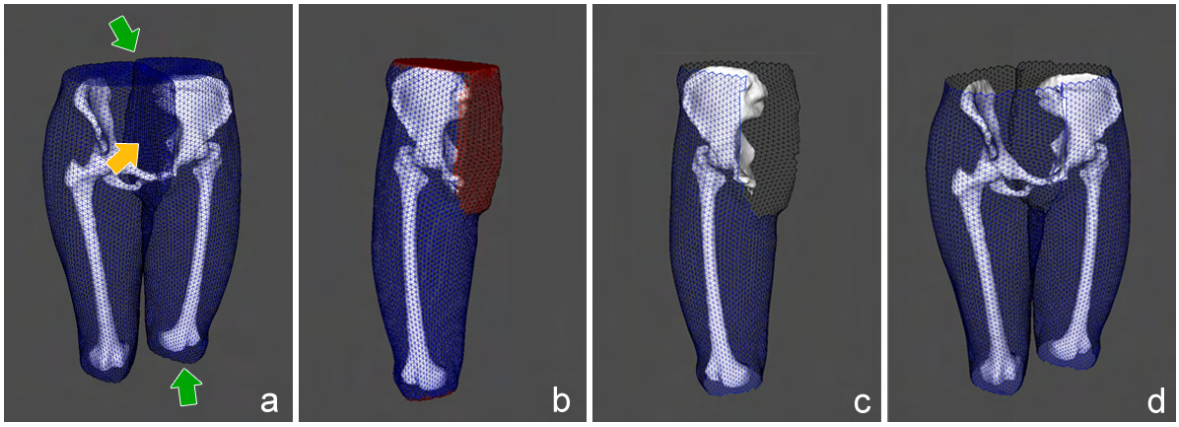

Figure 4.8: a) Merged skin models without pre-processing: the orange arrow shows the overlapping surfaces, the green arrows the internal body points b,c,d) Skin model pre-processing: the undesirable points (in red) are first selected (b) and then removed using the clipping filter (c). The two skin models are finally merged together (d).

4.3.5 Registration

The skin markers need to be repositioned in the 3D space according to the position of the bones, reconstructed from MRI. The third step of our calibration procedure thus consists in registering the body scan model and the extracted markers positions with the MRI skin model. As previously stated, the two models (the body scan model and the MRI skin model) are both patient-specific, but most importantly their meshes are generic, meaning that the morphological features have the same vertex indexes and connectivity across individual models. We will therefore exploit these geometric feature correspondences in our registration algorithm.

Since the MRI skin model is limited to the pelvis and the femur, our registration method [MTCS08]

[CAVMT09] works in two phases (Figure 4.9):

1. The body scan model surface from the pelvis to the knee is conformed to the MRI skin model using geometric correspondences.

2. The other body parts (i.e., the two shanks and the torso) are rigidly registered using a least-squares minimization.

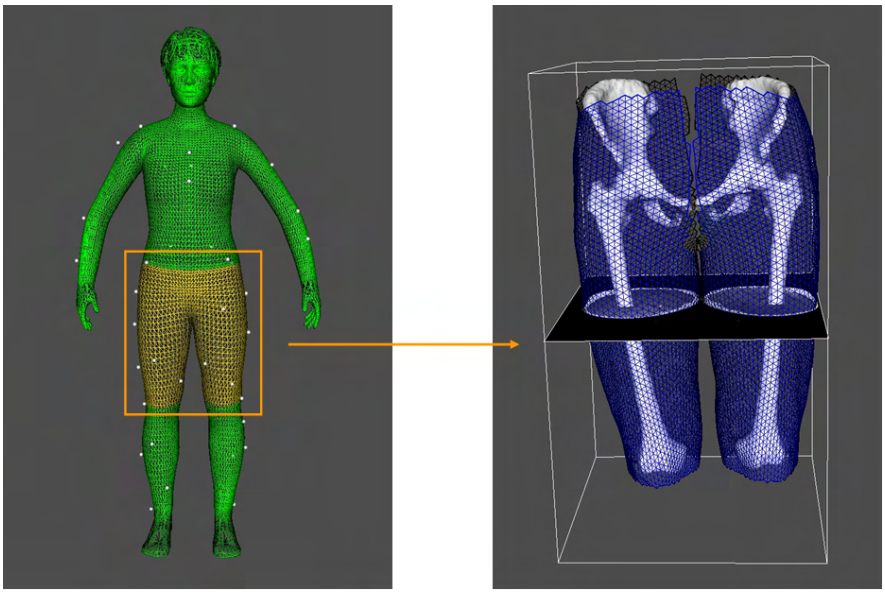

Figure 4.9: The markers and the body scan model segmented into two parts (left): the yellow part is conformed to the MRI skin model (right) and the green parts are rigidly registered.

Phase 1: Registration of the pelvis and the thighs

The objective is to compute a "deformation map" that stores geometric correspondences between the body scan model and the MRI skin model. To obtain this map, we manually register the two models for a single subject. Both meshes are now perfectly aligned and anatomical skin landmarks (e.g., the skin above the iliac crest, the femoral condyles, etc.) coincide (Figure 4.10). Let us consider Φ being the body scan model and Γ the MRI skin model. The two meshes are defined by a set of points $\Phi = \{P_i \in \mathbb{R}^3\}_{i=1}^{n}$ and $\Gamma = \{Q_i \in \mathbb{R}^3\}_{i=1}^{n}$, respectively. We project each point P_i onto Γ, yielding the projected point $P_{i\perp}$. The coordinates of $P_{i\perp}$ can be expressed with respect to the triangle on which $P_{i\perp}$ is projected. If $\mathbf{A}$, $\mathbf{B}$, and $\mathbf{C}$ are the vectors representing the vertices of the triangle, then the point $P_{i\perp}$ located on this triangle may be written as a weighted sum of these three vertices (Figure

4.11):

$$\mathbf{P_{i\perp}} = \mathbf{A}w_a + \mathbf{B}w_b + \mathbf{C}w_c \tag{4.5}$$

This is what we call the barycentric coordinates at point $P_{i\perp}$. They are normalized so that:

$$w_a + w_b + w_c = 1 \tag{4.6}$$

Since barycentric coordinates are a linear transformation of Cartesian coordinates, it follows that they vary linearly along the edges and over the area of the triangle. If a point lies inside the triangle, all the barycentric coordinates lie in the open interval $(0, 1)$. If a point lies on an edge of the triangle, at least one of the area coordinates $w_{a...c}$ is zero, while the rest lie in the closed interval $[0, 1]$.

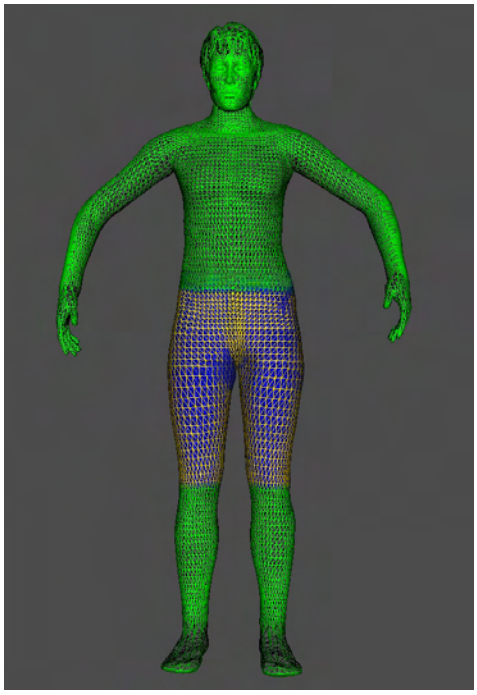

Figure 4.10: Manual registration: the body scan model and the MRI skin model are perfectly aligned.

During the pre-processing phase of the MRI skin model (see previous Section), overlapping points were removed for the skin models of each leg. Once the models are merged, a small hole at the crotch is left (Figure 4.12). The points P_i above this hole must be projected in the 3D space between the two surfaces and not on their boundaries. To ensure this, our algorithm is slightly modified to take into account this special case: the two closest points from P_i, Q_1 and Q_2 lying on each surface's boundaries, are first found. Then, $P_{i\perp}$ is calculated by linear interpolation, such as its coordinates

can be defined with respect to Q_1 and Q_2:

$$\mathbf{P_{i\perp}} = \mathbf{Q_1} w_1 + \mathbf{Q_2} w_2 \tag{4.7}$$

with

$$w_1 + w_2 = 1 \tag{4.8}$$

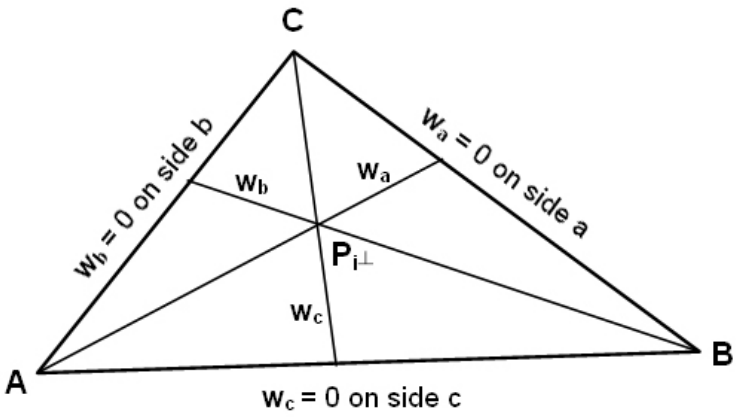

Figure 4.11: Barycentric coordinates at point $P_{i\perp}$.

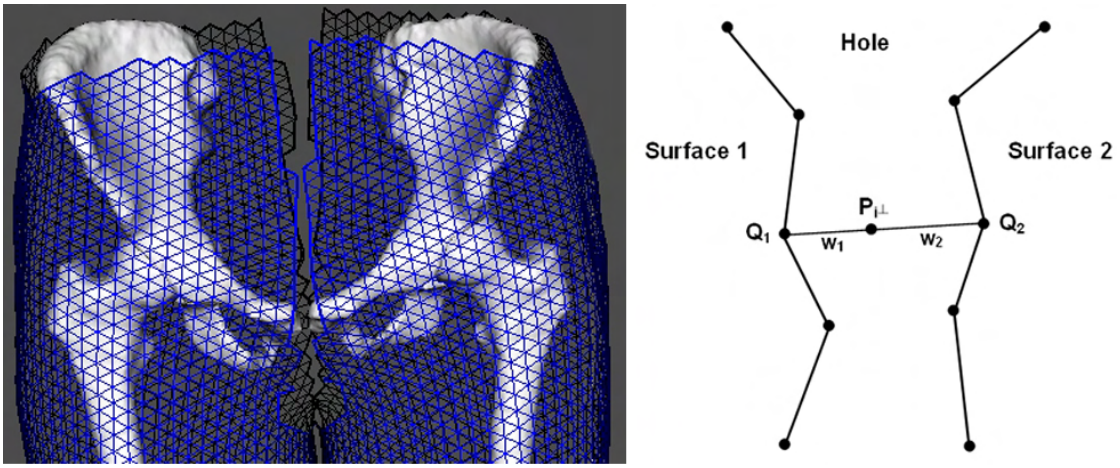

Figure 4.12: The MRI skin model with the hole at the crotch (left) and the corresponding schematic view (right) illustrating our projection method.

Finally, the deformation map is computed by storing the barycentric coordinates of each point $P_{i\perp}$. As a result, the body scan model can be automatically conformed to the MRI skin model for all

individuals, using this deformation map. To evaluate the registration accuracy, the contours of the two surfaces are drawn on the MRI slices (Figure 4.14b). The registration is considered as accurate, when the two contours are perfectly aligned for the entire MRI volume. We did not validate our algorithm as no significant nor systematic error was noticed visually.

Phase 2: Registration of the torso and the shanks

The two shanks and the torso are rigidly registered using a least-squares minimization [Hor87]. For each part, the following algorithm is executed. Let us consider a set of points $\{x_i \in \mathbb{R}^3\}_{i=1}^n$ belonging to the body scan model surface from the pelvis to the knee, at the junction of the part to be registered (Figure 4.13). These points are transformed in *Phase 1* and their new positions are denoted by $\{y_i \in \mathbb{R}^3\}_{i=1}^n$. We seek the best rigid transform $\mathbf{Rt}$ that minimizes the function:

$$\min \sum_{i=1}^{n} ||\mathbf{R}\mathbf{x_i} + \mathbf{t} - \mathbf{y_i}||^2 \tag{4.9}$$

with $\mathbf{R}$ the rotation matrix and $\mathbf{t}$ the translation vector. The resulting rigid transform is used to register the respective body part. For all parts, these appropriate points are selected on the generic body model to automatically obtain them from any individual models (Figure 4.13). Since our focus is on the hip joint, simple approximations for these parts are satisfactory.

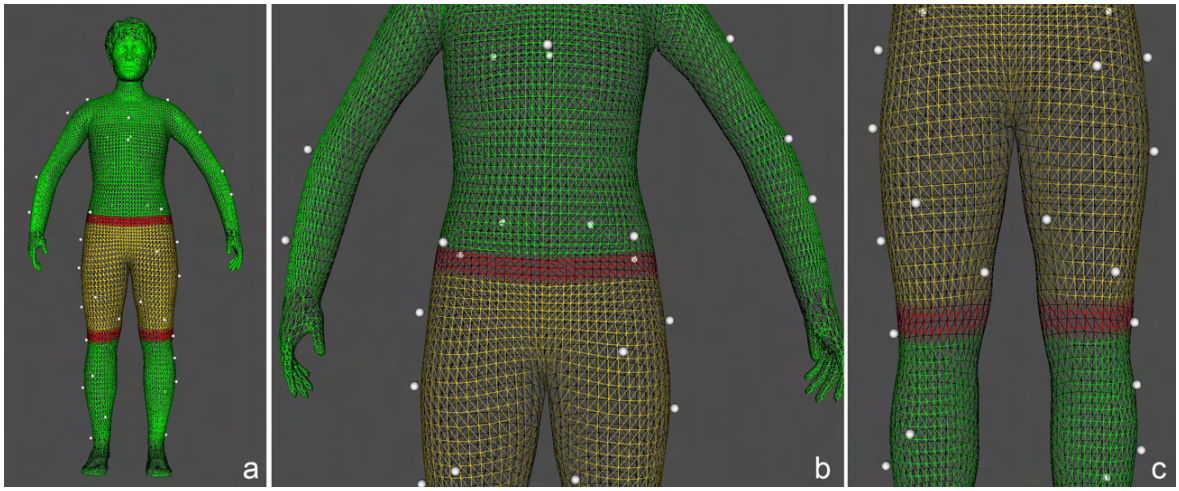

Figure 4.13: a,b,c) Rigid registration: for each part, appropriate points are selected (in red) on the generic body model surface from the pelvis to the knee, at the junction of the part of to be registered. Each set of points are used to compute the rigid transform of the torso (b) and the two shanks (c), respectively.

Registration result

Since the markers are linked to the body model surface, they follow the transformation of the body scan model. Consequently, the body scan model is repositioned in the MRI space. A calibration frame is also obtained where the relative position of the skin markers, with respect to the underlying bones, is now established. The overall registration requires ~ 2 seconds on a standard PC. Figure 4.14 shows the final registration result.

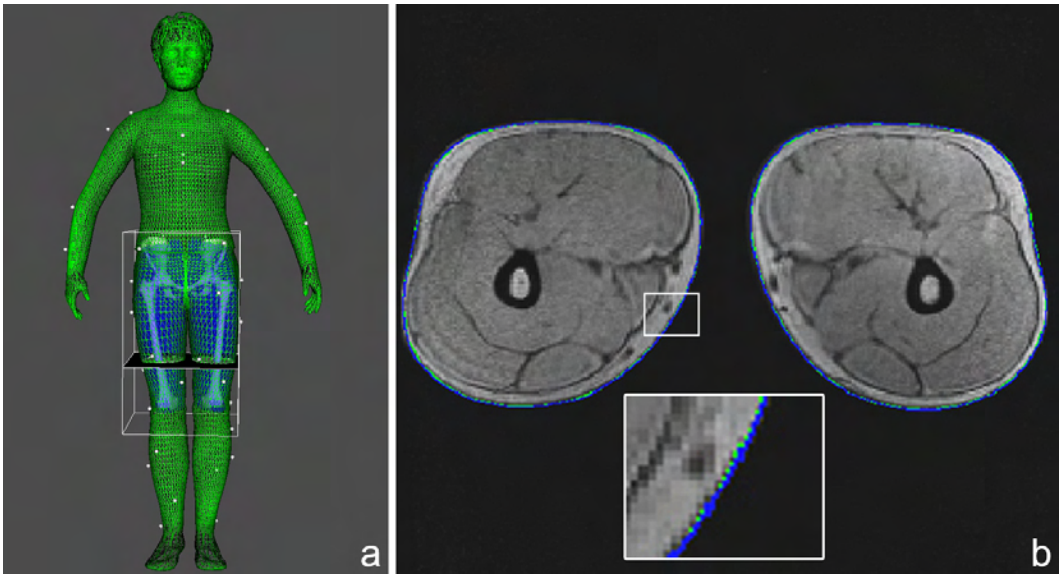

Figure 4.14: a) Registration result b) The surface contours drawn in a MRI slice: the green (body scan model) and blue (MRI skin model) contours are perfectly aligned.

4.3.6 Validation

To validate our calibration procedure, a MRI study was conducted. The study was carried out on a 27 year old female volunteer with a mass of $67kg$ and a height of $180cm$. Unfortunately, only one subject could participate in this validation test, because the MRI scanner was not available during our investigation period (due to clinical burden). For this test, the subject underwent two successive acquisitions:

- A 3D body scan with the skin markers used for motion capture.
- A static MRI scan in supine position with external MRI-compatible markers injected with contrast agent (Figure 4.15a).

It is important to note that the same markers configuration was used within the 3D body scanner and the MRI scanner.

Using the acquisition data, an anatomical calibration is performed. The MR images are also processed and the true positions of the visible markers are calculated. To verify if the skin markers are accurately repositioned in the MRI space using our calibration procedure, the positions of the markers are compared with those identified on the MR images. For our test, the average ± std. Dev. error made on the pelvic markers was $9.01mm \pm 1.07mm$ and on the femoral markers was $7.98mm \pm 1.22mm$, as shown in Figure 4.15b. From these results, our calibration procedure is thus successfully validated. Indeed, errors in the determination of ALs of up to $18mm$ are generally considered using the CAST protocol [CCK99] [RBF$^+$02] [CLCC05]. We can hence conclude that our calibration procedure performs better than this standard anatomical calibration technique.

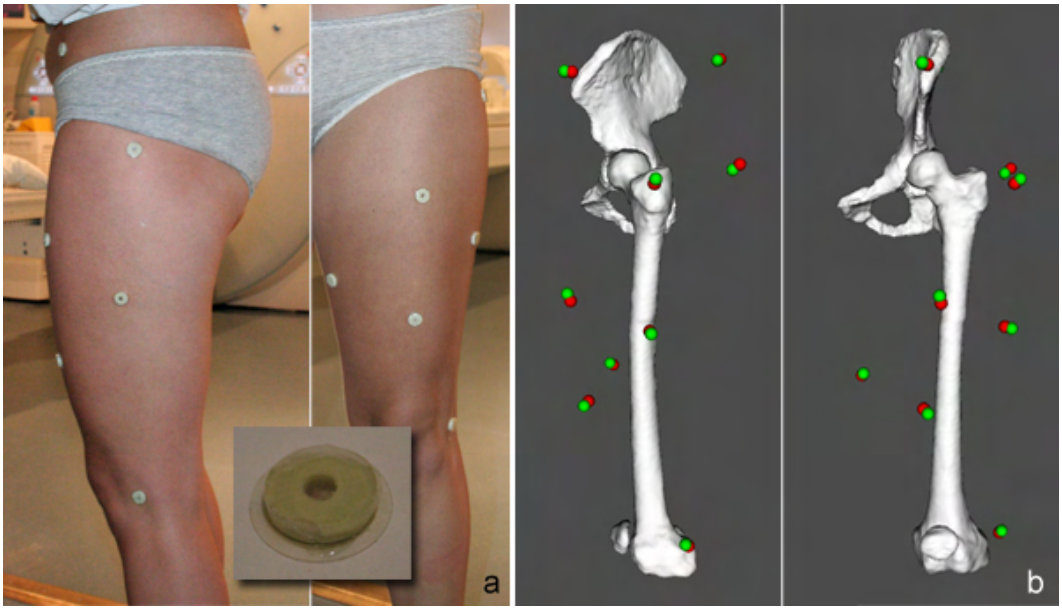

Figure 4.15: a) MRI-compatible markers setup b) Error made on the skin markers after anatomical calibration: green = real markers positions (MRI-compatible markers), red = registered skin markers.

4.4 Soft tissue artifact minimization

When human motion is measured using optical motion capture system, the skin moves with respect to the underlying bone. If a reflective marker is stuck on the body surface, it will also be affected by the skin's relative movement (e.g., $20mm$ for a marker stuck on the thigh [CCL$^+$96]). The resulting

estimations are thus embedded with STA. The rigid motion of the bone segment can therefore not be robustly estimated from the markers trajectories, unless the STA is small. This "shifting" effect is very critical particularly when precise analyses of the joint motion are needed.

In Section 2.4, we have seen that the movement of a cluster of markers with respect to the underlying bone can be interpreted as a sum of an internal cluster deformation plus a rigid displacement. For a complete correction of STA, these two different aspects must be addressed:

- To minimize the cluster deformation, we perform a nonlinear optimization [CLMT08] [CAVMT09] [CSKC$^+$09] to find, for each segment and for each instant frame, the best rigid transformation that minimizes the error made globally on all the markers.
- The rigid displacement of the cluster results in non-physiological joint translation and dislocation. To cope with this issue, joint constraints allowing some shifts at the joint are applied [CAVMT09] [CSKC$^+$09]. This is actually done in two phases:
  - First, the hip joint center (HJC) is kept fixed to avoid the dislocation.
  - Then, our algorithm adjusts the HJC by detecting collisions among the articular bones, the goal being to reach the non-penetrating state. Indeed, although the HJC can be considered to be fixed during low amplitude movements, this is no longer true for extreme motion [GKCMT$^+$09]. Thus, a potential subluxation may occur to avoid bones penetration.

Our algorithm only requires a *.csm* file as input and runs in real-time, which depicts a fast method given the complexity of the task. More details about our correction method are given in the coming sections. The validation of our proposed algorithm is also discussed in Section 4.4.4.

4.4.1 Nonlinear optimization

STA introduces systematic as well as random errors (see Section 2.3). Thus, our bone pose estimation algorithm should be robust and accurate enough to deal with nonlinear markers movements. Instead of trying to figure out the skin motion for each of the markers, we propose to find for each segment and for each instant frame the rotation and translation that minimize the error made globally on all the markers.

Previous bone pose estimators generally solve the optimization problem linearly. For instance, typical resolution methods include the quaternion method [Hor87] or the Single Value Decomposition (SVD) algorithm [SB93]. By their nature, the optimized solutions are not accurate, since these methods do

not account for the nonlinearity of the markers motion. We therefore use a more powerful optimization algorithm, a sequential quadratic programming algorithm, to minimize the cluster deformation. From our data, we will demonstrate that this nonlinear optimization algorithm is robust and more accurate than the classical methods. First, let us introduce the nonlinear problem:

Six unknowns (3 for the rotation and 3 for the translation) must be estimated to determine the segmental motion parameters. From the markers motion, the objective function to minimize, for each bone and for each instant frame, is defined as follows:

$$\min \sum_{i=1}^{n} (\mathbf{p_i} - \mathbf{p'_i})^2 \tag{4.10}$$

where

$$\mathbf{p'_i} = \mathbf{R}\mathbf{q_i} + \mathbf{t} \tag{4.11}$$

with n the number of markers attached to the bone segment, $\mathbf{p_i}$ the current position of the i^{th} marker, $\mathbf{p'_i}$ its estimated position, and $\mathbf{q_i}$ its reference (or previous) position. The best rigid transform is denoted by $\mathbf{Rt}$, where $\mathbf{R}$ is the rotation matrix and $\mathbf{t}$ the translation vector. This is basically a least-squares minimization for which we use the RFSQP optimizer [LT01], after having implemented it, tuned its parameters and constraints, and given the appropriate objective function. Since the skin markers move nonlinearly, the solution converges faster thanks to this sequential quadratic programming (SQP) algorithm. Indeed, SQP algorithms are widely acknowledged to be among the most successful algorithms available for solving this kind of nonlinear problem. As it is out of the scope of this thesis to develop the theory behind SQP algorithms, the interested reader can refer to [BT95] for an excellent survey. However, we will evaluate the robustness of the RFSQP optimizer, while its accuracy will be discussed in Section 4.4.4.

To evaluate the robustness of this algorithm, numerical experiments are performed. We have 6 different dancing movements recorded for 11 subjects at our disposal (see Chapter 5 for more details about the data of our study). For each movement and for each instant frame, we compute the sum of squared distances between the measured and model-determined marker coordinates, according to Equation 4.10. These values $\{x_1, x_2, \ldots, x_n\}$ represent the error made globally on all the markers. Then, the root mean square (RMS) error is calculated for each movement and for each subject as:

$$x_{rms} = \sqrt{\frac{1}{n}\sum_{i=1}^{n} x_i^2} = \sqrt{\frac{x_1^2 + x_2^2 + \cdots + x_n^2}{n}} \tag{4.12}$$

with n the number of observations. Table 4.2 reports by movement the results obtained by averaging RMS values for the 11 subjects' trials. Moreover, Figure 4.16 shows a visual example of the estimated vs. recorded markers positions. Since no significant error was detected from these results, we can infer that the RFSQP optimizer is robust for all subjects and for all movements.

Movements	**RMS**
Arabesque	0.61
Développé devant	0.8
Développé à la seconde	0.81
Grand écart facial	1.09
Grand écart latéral	0.79
Grand plié	0.72

Table 4.2: RMS errors by movement, obtained by averaging RMS values for the 11 subjects' trials. Values are reported in mm.

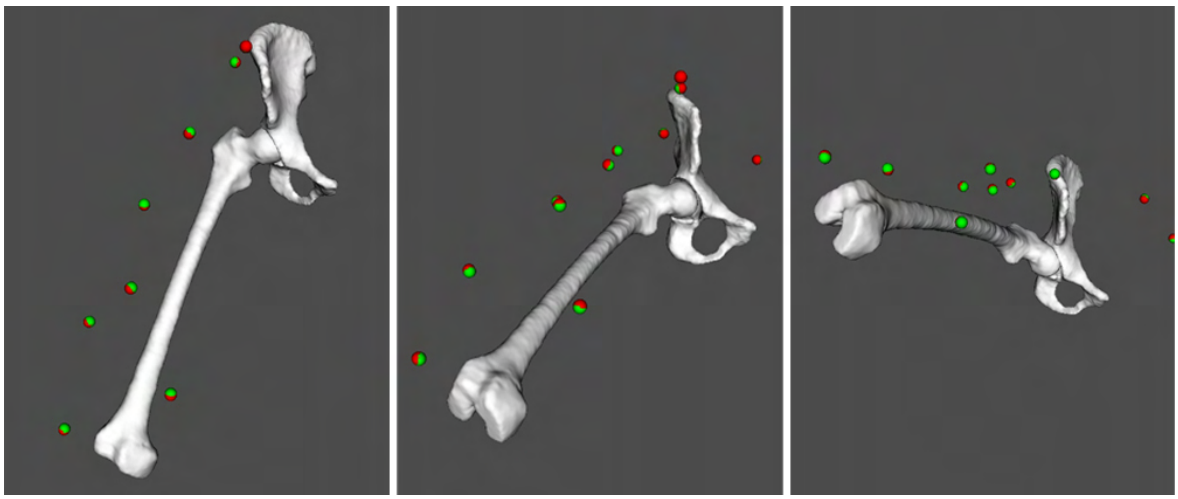

Figure 4.16: Visualization of the error made on the markers during motion (3 different postures): the red spheres are the recorded markers positions ($\mathbf{p_i}$), while the green spheres are their estimated positions ($\mathbf{p'_i}$).

4.4.2 Joint constraints

Even with the use of a robust optimizer, the STA are not completely minimized. Indeed, non-physiological joint translation must be discarded. To cope with the rigid motion of the cluster, our approach is not meant to impose strong kinematic constraints, as this was addressed in [LO99]. We rather aim at applying little joint constraints, allowing some shifts at the joint. Our two-phase method

is explained below:

During a movement, several components contribute to the motion of a skin marker. Assuming that the pelvis motion is known, the HJC can slightly move during the rotation of the femur. This introduces one translation T_c and one rotation R. Additionally, a rigid displacement is observed due to STA which is denoted by another translation T_s. The motion of a marker with respect to the pelvis can hence be described by 3 transformations successively applied. Applying the translation before or after the rotation can yield to the same transform, only the numerical value of the translation will change. A rigid transform can always be decomposed into a rotation and a single translation. Therefore, one of the translations must be discarded, since we cannot accurately estimate both T_c and T_s simultaneously. Previous works (see Section 2.3) showed that, for the thigh, the magnitude of the STA is greater that the displacement of the HJC. Therefore, we decide to compute the best estimate of T_s and to assume that T_c is close to null. On the contrary, for the pelvis, it appears that the STA remains small. Thus, for this segment we assume that T_s is close to null and we estimate T_c instead.

In practice, we use the pelvic and femoral coordinate systems to assess the relative position between the hip and femur bones. As discussed in Section 3.6.1, the femoroacetabular translations are equal to zero, when the origins of the two frames are aligned on the same point. Joint constraints therefore consist in applying a translation to the femur, so that the origins of the pelvic and femoral frames are aligned on the HJC estimated from the pelvis motion. Figure 4.17 illustrates this correction. Consequently, the HJC is kept fixed during the femur motion. We will now see how T_c can be estimated for the femur.

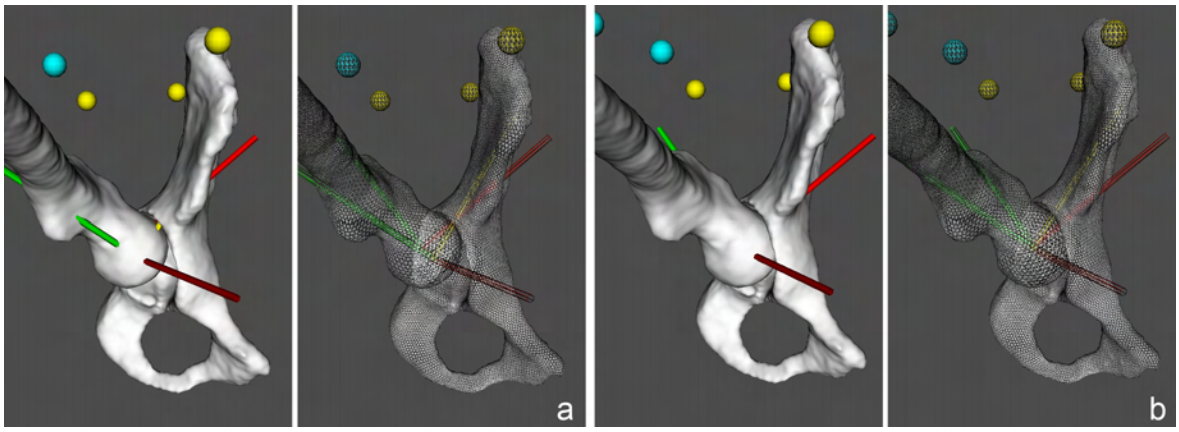

Figure 4.17: a) The femur undergoes non-physiological translations due to STA b) The position of the femur is corrected, so that the origins of the pelvic and femoral frames are aligned on the HJC.

4.4.3 Collision detections

When the HJC is kept fixed during the previous phase, the surfaces of the femur and hip bone may intersect, especially during extreme motion (Figure 4.18). This intersection should be canceled by adjusting the HJC.

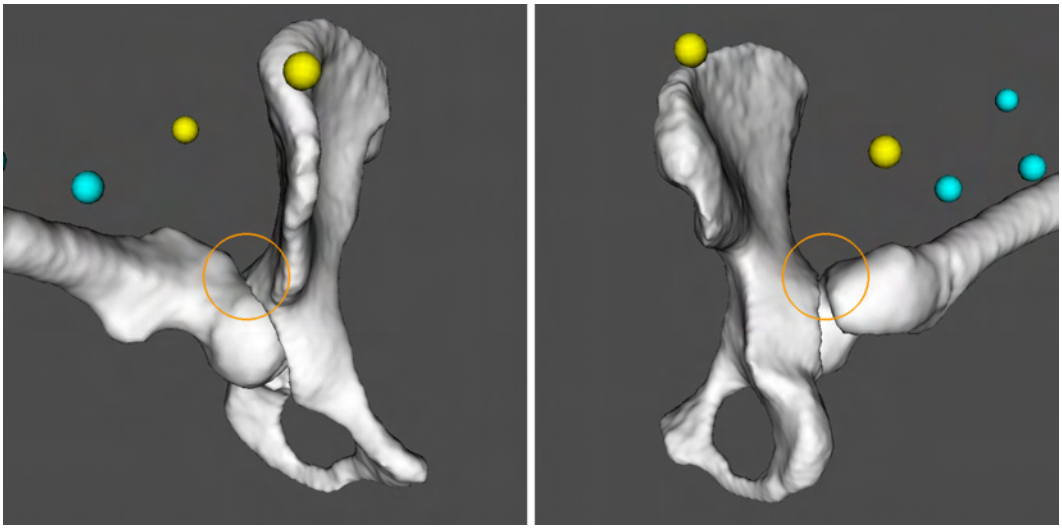

Figure 4.18: Intersection (orange circles) between the surfaces of the femur and hip bone that generally occurs during extreme motion (front and back views).

We assume that the position of the hip bone is correct, because the magnitude of the STA remains small for this bone. Therefore, in case of collision between the articulating bones, it is the position of the femur that must be corrected, for each instant frame, in order to reach the non-penetrating state. This correction corresponds to a translation of the HJC of vector $\mathbf{D_{HJC}}$. For fast computation, we test points between the proximal femur and acetabulum only, and a uniform-level octree subdivision [GLM96] is used for the hip bone model. The following algorithm is applied (Figure 4.19): let us consider Φ being the *collider* (i.e., the femur) and Γ the *collided object* (i.e., the hip bone). The two meshes are defined by a set of points $\Phi = \{P_i \in \mathbb{R}^3\}_{i=1}^{n}$ and $\Gamma = \{Q_i \in \mathbb{R}^3\}_{i=1}^{n}$, respectively. First, we project each point P_i onto Γ, yielding the projected point $P_{i\perp}$. Then, P_i is defined as being inside, and therefore colliding, if:

$$\mathbf{P_i P_{i\perp}}.\mathbf{N_{P_{i\perp}}} > 0 \tag{4.13}$$

where $\mathbf{N_{P_{i\perp}}}$ is the outward normal at $P_{i\perp}$. This subset of k colliding points $C_k = \{P_1, \ldots, P_k\}$ creates the displacement vector:

$$\mathbf{D} = \frac{\sum_{i=1}^{k} \mathbf{P_i P_{i\perp}}}{k} = \frac{\sum_{i=1}^{k} \mathbf{d_i}}{k} \tag{4.14}$$

The *collider* undergoes a translation proportional to the vector $\mathbf{D}$. This algorithm is iteratively performed for each instant frame, until no more collisions are detected. As a result, the translation $\mathbf{D_{HJC}}$ of the HJC is equivalent to the sum of the translation vectors applied to the *collider*.

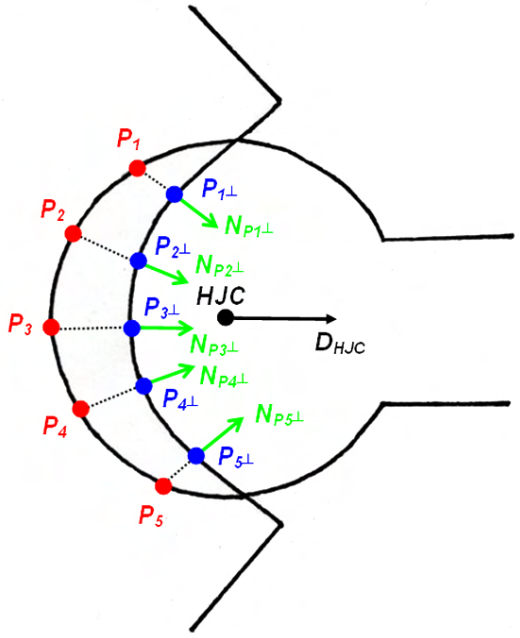

Figure 4.19: 2D schematic view of the collisions detection algorithm: the femur is corrected at each instant frame. As a result, the HJC undergoes a translation of vector $\mathbf{D_{HJC}}$.

4.4.4 Validation

To validate our hip joint kinematics estimation, a dynamic MRI study was conducted. The study was carried out on 6 volunteers (3 females and 3 males, mean ± std. Dev. age: 30.17 ± 3.13 years; mean ± std. Dev. weight: 64.33 ± 8.78kg) during clinical motion patterns: flexion/ extension, abduction/ adduction, internal/ external rotation. To assess skin/ bone relative movement, MRI-compatible markers with injected contrast agent were placed onto the skin and acquired. To ensure the movements repeatability across volunteers, a positioning device was used to block the leg at the different steps. A fast MRI protocol [GPMTV05] allowing accurate bone tracking was applied based on a fast gradient echo sequence (acquisition time: 2.5min). The MR series were then processed and the trajectories of the visible markers were calculated using a 2D/ 3D registration method [GPMTV05] for bone and markers tracking.

Since the true bone and markers motion are known, it is interesting to evaluate the magnitude of STA

in our data. Indeed, we can compute the markers positions as if they were rigidly fixed to the bone (using the bone transforms given by the tracking method) and compare these computed positions with the actual markers positions. To quantify the markers displacements, we calculate for each instant frame and for each marker, the displacements in the X, Y and Z directions and the Euclidean distance between the computed and actual marker position. Table 4.3 summarizes by subject the overall markers displacements. These results depict relatively strong markers displacements, with peak values of more than $1cm$.

	X	**Y**	**Z**	**Euclidean distance**
Subject #1				
Mean	2.02	1.64	1.78	3.61
RMS	2.57	2.02	2.2	3.95
Std. Dev.	1.6	1.2	1.31	1.6
Subject #2				
Mean	3.76	1.55	2.61	5.59
RMS	6.87	1.91	4.64	8.51
Std. Dev	5.78	1.11	3.86	6.46
Subject #3				
Mean	5.56	1.91	5.83	9.19
RMS	7.57	2.53	8.3	11.52
Std. Dev.	5.16	1.66	5.93	6.97
Subject #4				
Mean	3.34	1.85	3.32	5.67
RMS	4.66	2.42	4.714	7.05
Std. Dev.	3.26	1.57	3.34	4.21
Subject #5				
Mean	3.13	2.57	3.65	6.25
RMS	3.92	3.87	4.88	7.37
Std. Dev.	2.38	2.91	3.26	3.91
Subject #6				
Mean	8.27	1.81	6.73	12.29
RMS	16.22	2.38	13.05	20.96
Std. Dev.	14.01	1.55	11.23	17.05

Table 4.3: Markers displacements in X, Y and Z directions, and Euclidean distances between the computed and actual marker position. Values are reported in mm.

To validate our proposed algorithm, we will compare the hip joint kinematics derived from the marker position data and the true hip motion obtained with the tracking method. As the kinematic errors must be expressed in the hip joint coordinate system, several transformations are needed. With our algorithm, the motion of the hip and femur bones are estimated using relative transformations, whereas the tracking method provides global transformations. The relative bone transforms are therefore first

converted to global bone transforms through Equation 3.22, and the hip joint kinematics is then computed from Equation 3.19. To verify if our algorithm performs better than traditional bone pose estimators, its performance is compared to the SVD algorithm. Finally, the benefit of using joint constraints is also verified. Thus, four different tests are performed:

- Using the RFSQP optimizer with joint constraints
- Using the RFSQP optimizer without joint constraints
- Using the SVD algorithm with joint constraints
- Using the SVD algorithm without joint constraints

Table 4.4 shows the femur position and orientation reconstruction errors expressed in the hip joint coordinates system, according to the four different tests.

	tz	**tx**	**ty**	γ	α	β
RFSQP optimizer with joint constraints						
Mean	0.37	0.45	0.19	0.43	3.28	1.49
RMS	0.4	0.59	0.24	0.55	3.86	1.71
Std. Dev.	0.17	0.4	0.16	0.37	2.06	0.89
RFSQP optimizer without joint constraints						
Mean	2.42	3.44	1.76	0.44	3.58	1.55
RMS	2.99	4.12	2.01	0.56	4.14	1.8
Std. Dev.	1.9	2.35	1.06	0.37	2.12	0.95
SVD algorithm with joint constraints						
Mean	0.27	0.27	0.14	0.53	5.0	3.33
RMS	0.36	0.42	0.2	0.81	6.12	4.03
Std. Dev.	0.24	0.36	0.15	0.66	3.68	2.43
SVD algorithm without joint constraints						
Mean	4.17	3.53	1.66	0.53	5.0	3.33
RMS	5.51	4.37	2.22	0.81	6.12	4.03
Std. Dev.	3.74	2.79	1.67	0.66	3.68	2.43

Table 4.4: Femur reconstruction errors for medio-lateral (tz), antero-posterior (tx) and proximo-distal (ty) translations $[mm]$, and for flexion/ extension (γ), abduction/ adduction (α) and internal/ external rotation (β) $[deg]$.

Only the error on the femur translation/ orientation was calculated, since no markers were placed on the pelvis (due to insufficient MRI-compatible markers available). As previously stated in Section 2.3, the femur exhibits substantial skin motion, while the pelvis is relatively free of artifacts. From these results, we conclude that the RFSQP optimizer performs better than the SVD algorithm. Joint

constraints are also essential to decrease the translation errors. Moreover, it is worth mentioning that our translation errors are in the order of magnitude of the bone motion tracking accuracy ($\sim 0.5mm$). The STA errors are hence significantly minimized by the use of the proposed algorithm, with respect to the amount of STA found in our data.

4.5 Body animation

Only animating the hip do not provide a global view of the movement performed by the subject. Moreover, it could confuse an orthopedist who is not used to visualize objects in 3D. Therefore, to improve the analysis and visualization of the motion, a ball and stick representation of the overall skeleton is added and a run-time skin animation is performed through a skeleton-driven deformation algorithm.

Skeleton-driven deformation is very popular in virtual human animation, as it allows simple computation of skin deformation according to the subject's pose. In literature, skeleton-driven deformation is often referred to as Sub-Space Deformation (SSD) or skinning [MTLT88]. The idea is to compute skin transformation as a weighted sum of joint transforms (matrix blending), weights being defined according to joint influences.

Our technique to animate the skeleton and the skin is explained below:

4.5.1 Skeleton animation

In stick-figure representation, the skeleton consists in a series of bones (i.e., sticks) connected together by joints (i.e., balls). Contrary to orthopaedics and biomechanics where a precise modeling of bone surfaces is required, the only requirement here is the use of precise joint centers. Joint degrees of freedom are exploited to derive or analyze postures of the articulated figure. Each joint has a transformation (up to 3 DOFs and stored as a transformation matrix) and an optional parent bone. As a result, the skeleton forms a hierarchy where the root is a joint with 6 DOFs. Our skeleton implementation consists of 16 joints and 20 bones.

Bone poses are obtained from motion capture data through Equation 4.10. However, because the RFSQP optimizer needs many iterations to converge, we use the SVD algorithm for faster, yet less accurate computation. Eventually, joint constraints are imposed to discard the translation. Since the goal is purely visual, the emphasis is not on the accuracy, but on the computational cost reduction. Figure 4.20 shows examples of computed dancing postures.

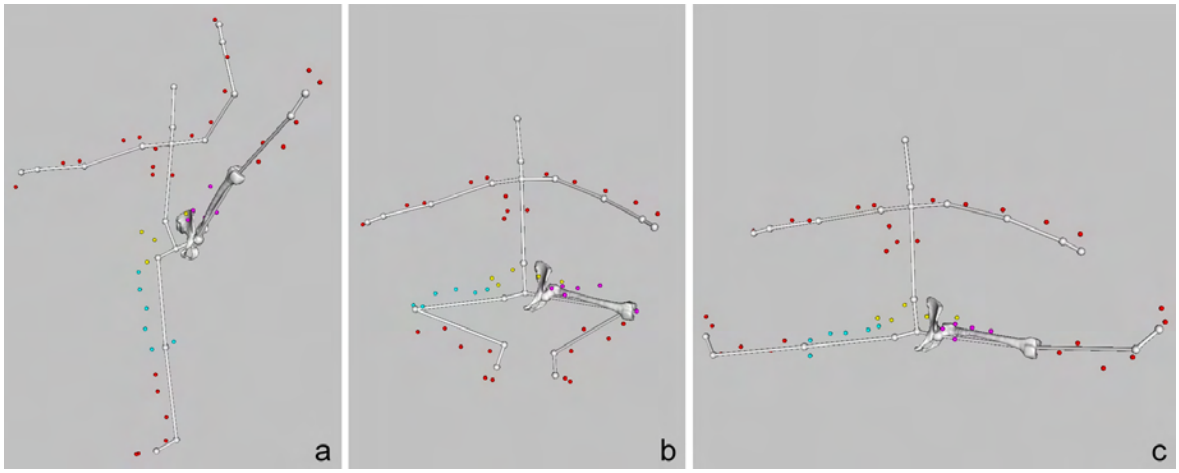

Figure 4.20: Examples of computed dancing postures: a) développé à la seconde b) grand plié c) grand écart facial.

4.5.2 Skinning

The skin we animate is the body scan model that was previously used for the anatomical calibration. The resolution of this mesh is suitable for real-time animation. Skinning is the process of attaching and deforming a renderable skin to an underlying articulated skeleton. Using a smooth skinning algorithm, each vertex in the mesh can be attached to more than one joint, each attachment affecting the vertex with a different strength or weight. The final transformed vertex position is a weighted average of the initial position transformed by each of the attached joints. For example, the vertices in a subject's knee could be partially weighted to both the hip joint (controlling the thigh) and knee joint (controlling the shank). Many vertices will only need to be attached to one or two joints and rarely is it necessary to attach a vertex to more than four. These attachments are defined using a commercial animation software (Autodesk 3ds Max[1]) and are then imported in our application.

Our skinning algorithm works as follows: let us say that a particular vertex is attached to N different joints. Each attachment is assigned a weight w_i which represents how much influence the joint will have on it. To ensure that no undesired scaling will occur, all of the weights for a vertex are normalized so that:

$$\sum w_i = 1 \qquad = w_0 + w_1 + \ldots + w_{N-1} \tag{4.15}$$

To compute the position $\mathbf{v}'$ of the vertex in the global coordinate system (in our case, the MRI scanner

[1] `http://usa.autodesk.com/`, accessed November 2009

frame), we transform it by each joint that it is attached to, and compute a weighted sum of the results:

$$\mathbf{v}' = \sum w_i \mathbf{v} \cdot \mathbf{B}_{[\mathbf{i}]}^{-\mathbf{1}} \cdot \mathbf{W}_{[\mathbf{i}]} \tag{4.16}$$

where $\mathbf{v}$ is the untransformed vertex in the skin local frame, the frame in which the body scan model was originally modeled. The matrix $\mathbf{W}_{[\mathbf{i}]}$ is the global transform of the joint for attachment i. We use the indexing notation $[i]$ to indicate that we don't want the matrix of the i^{th} joint in the skeleton (which would be written as $\mathbf{W_i}$), but instead we want the global matrix of attachment i's joint. The matrix $\mathbf{B}_{[\mathbf{i}]}$ is called the binding matrix for joint i and represents the transformation from joint local frame to skin local frame. Therefore, the inverse of this matrix, $\mathbf{B}_{[\mathbf{i}]}^{-\mathbf{1}}$, represents the opposite transformation from skin local frame to joint local frame. Consequently, the combined transformation $\mathbf{B}_{[\mathbf{i}]}^{-\mathbf{1}} \cdot \mathbf{W}_{[\mathbf{i}]}$ in Equation 4.16 first transforms $\mathbf{v}$ from skin local to joint local, then from joint local to global space. In our case, the body scan model is already repositioned in the MRI space thanks to the anatomical calibration, the matrix $\mathbf{B}_{[\mathbf{i}]}^{-\mathbf{1}}$ can thus be ignored. The skinning equation that must be computed for each vertex and for each instant frame is hence simplified to:

$$\mathbf{v}' = \sum w_i \mathbf{v} \cdot \mathbf{W_i} \tag{4.17}$$

Figure 4.21 shows examples of computed dancing postures with the animated body scan model.

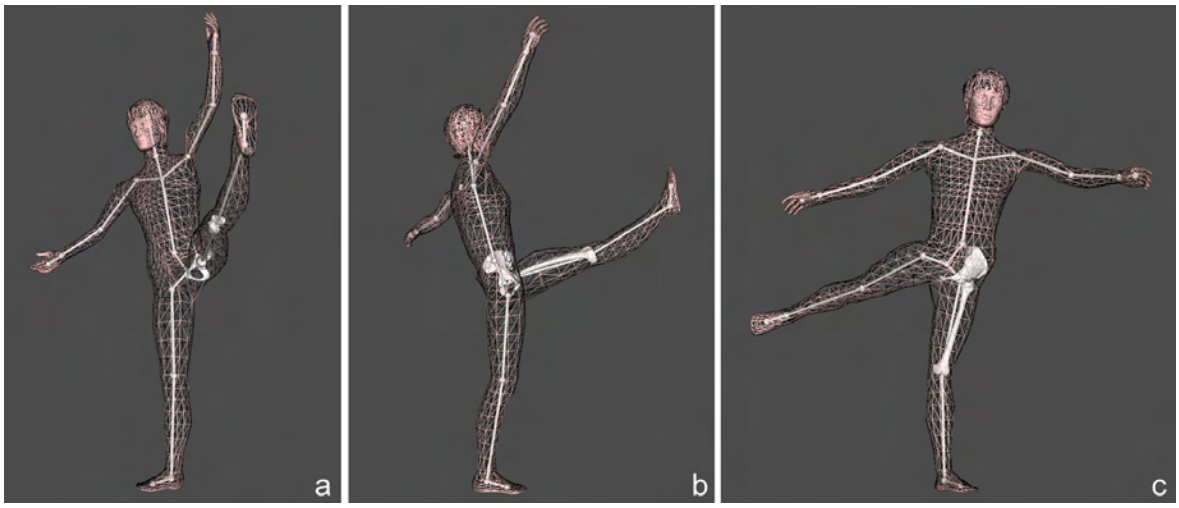

Figure 4.21: Examples of computed dancing postures with the animated body scan model: a) développé à la seconde b) développé devant c) arabesque.

4.6 Semantic-driven platform

In this thesis, a large amount of multimodal data are used (3D models, MRI, 3D body scan data and motion capture data). The orthopedists must therefore manage and visualize information at a high level of complexity. To reduce this complexity, to exploit the information effectively and to guide the orthopedist during patient's examination, we developed a semantic-driven platform able to centralize and structure the multimodal data inputs and the medical knowledge in a coherent and unified manner. Indeed, there is an increasing need to provide more user-centric systems that act as "intelligent" assistants, able to interact naturally with human users and with the information environment. Our system integrates conventional diagnostic support (MRI, morphological measurement tools), visualization features and the processing methods presented in this chapter. Figure 4.22 shows a screen shot of the software's graphical user interface.

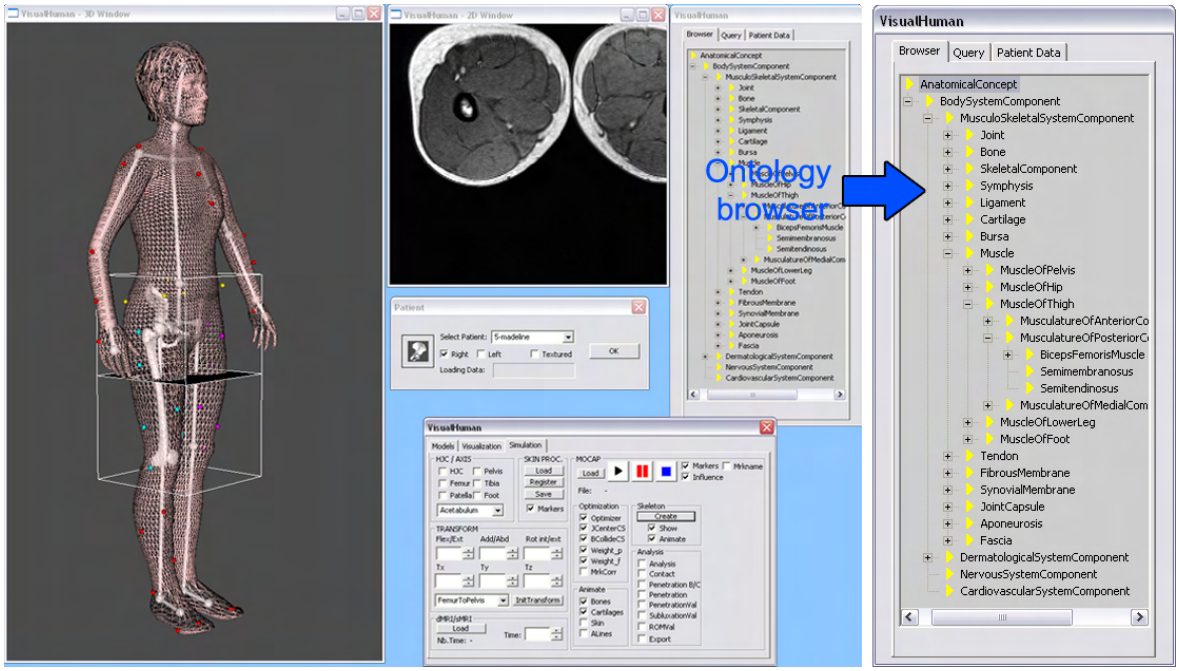

Figure 4.22: The semantic-driven platform with the ontology (right hand window and right image), the 3D visualization window (left), the MRI window (middle top), the patient loader (middle window) and the visualization/ simulation tools (bottom right window).

The platform is driven by a medical ontology that takes into account not only the anatomy, but also the functionalities of the musculoskeletal system. Our model comprises 825 classes and 1244 instances, representing the concepts and their relationships that relate to the structural anatomy of the human musculoskeletal system at the macroscopic level. This ontology thus contains the core

medical knowledge and acts as a medical interpreter between the user and the data (e.g., the ontology is accessible through the graphical user interface). Furthermore, the ontology offers a support for data fusion and completion, and automates the data transfer and processing thanks to the quick access to the simulation parameters stored in the model.

The primary goal is to provide orthopedists with an interactive visualization/ simulation framework of the individualized hip joint examination. The software was therefore developed in close collaboration with orthopedic surgeons and was tested in the clinical environment. More information about the semantic-driven platform and use case scenarios can be found in [CGMT07]. Appendix C also provides details about the software's implementation and functionalities.

4.7 Conclusion

The different steps to estimate the hip joint kinematics have been developed in this chapter: the recording phase by using optical motion capture technology with an appropriate markers protocol, the anatomical calibration phase to register anatomical and motion frames based on the 3D body scanning technology and the bone pose estimation phase by using an optimized fitting algorithm which accounts for STA and anatomical constraints. Moreover, we have seen how we have improved the visualization and analysis of the motion by animating the overall skeleton and skin of the subject. All implementations/ tests have been integrated/ performed into/ with the use of a semantic-driven platform.

In the medical field especially, because of its obvious societal impact, an important phase is the validation. Therefore, before proceeding to *in vivo* measurements and analysis, our methods have been carefully validated. Now that our motion protocol is set up, experiments can be carried out. We will apply our algorithms and methodology to the investigation of extreme range of motion of the hip joint in typical dancing postures. The results of our proposed contributions and the study of professional ballet dancers' hips are detailed in the coming chapter.

Chapter 5

Experiments and results

[1]Auguste Rodin, 1840-1917. Six studies of Kampuchean dancers. Painting, 1906. Image from `http://www.musee-rodin.fr/expositions/cambodge.html` used by permission.

5.1 Introduction

Professional ballet dancers present a high risk of developing hip osteoarthritis (OA) due to repetitive and extreme movements performed during their daily dancing activities [Mas01] [Bin03] [LS06] [GH09]. In the nondysplastic hip, early OA could be caused by femoroacetabular impingements (FAI) which occur when there is an abutment conflict between the proximal femur and the acetabular rim [BKG05] [PMD+06] [TGB+08] [LeG09]. FAI of the cam/ pincer type cannot explain observed OA in hips with normal morphology. However, repetitive microtrauma is believed to be one of the causes of the development of early OA in the young active adult [Mas01] [MNS+01]. Indeed, sporting activities that require frequent lateral (external) rotation [Mas01] [MNS+01] [Bin03] [MNA+03] [CKH+09] [GH09] or hyperabduction [NV00] [GH09] such as ballet, have been thought to result in labral tears. Nevertheless, the arthrogenous movements have not yet been clearly identified. It is also unknown whether the femoral head and acetabulum are congruent in extreme positions (e.g., split position). Joint congruency could be another potential cause of early OA.

Our hypothesis is that the practice of some dancing movements could expose the dancer's hip to a loss of joint congruence and to recurrent impingements, which could lead to early chondrolabral damages. In this chapter, we present the results of a prospective study conducted with female professional ballet dancers. The purpose of this study is to visualize and simulate extreme ranges of motion of the hip and to detect and locate potential FAI. Moreover, we aim at quantifying *in vivo* the range of motion (ROM) and congruence of the hip joint in typical dancing positions. We will show how our methodology and algorithms presented in Chapter 3 and 4 contribute to this investigation.

The remaining of this chapter is organized as follows: first, we introduce the subjects and the clinical evaluation (anamnesis, MRI examination and morphological analysis) performed in collaboration with the University Hospital of Geneva. Then, we present the motion capture protocol and the techniques developed to detect and locate FAI, to compute the joint congruency and to quantify the hip ROM. Finally, a statistical analysis is conducted and the results of our proposed contributions are reported. The chapter ends with a discussion about the study's findings.

5.2 Subjects

The present study was carried out on 11 female dancers (22 hips) aged between 18 and 38 years (mean: 25.36 years; std. Dev.: 6.78 years) with a mean mass (Std. Dev.) of $54.36kg$ ($4.52kg$) and a mean height (Std. Dev.) of $168.72cm$ ($4.9cm$) (Table 5.1). The volunteers were all professional

and performed classical ballet and contemporary dance. The exclusion criterion was a history of hip surgery. The study was approved by the local ethics committees and the volunteers gave written informed consent.

Subject	**Age**	**Weight** $[kg]$	**Height** $[cm]$
#1	30	53	170
#2	35	60	157
#3	22	60	168
#4	30	54	171
#5	21	48	167
#6	19	54	177
#7	18	48	167
#8	38	50	170
#9	24	54	168
#10	21	60	173
#11	21	57	168

Table 5.1: Subjects age, weight and height.

5.3 Clinical evaluation

To determine the prevalence of FAI of the cam/ pincer type and the prevalence and type of hip lesions on MRI in dancers, a clinical evaluation was carried out. All subjects underwent MR imaging and a complete physical examination of the hip. Moreover, the morphology of the dancers' hips was analyzed using standard measurements. Clinical examination and MR imaging were performed by orthopedists and radiologists from the University Hospital of Geneva, respectively. We supported them in these tasks by providing a statistical assessment of the data. Morphological analysis was executed by us. For this purpose, a set of measurement tools was implemented in 3D, improving the (subjective) reading of medical images.

In the following, the clinical evaluation outcomes are presented and discussed. The aim is to clinically evaluate the dancers' hips and to subsequently compare the findings to motion capture simulation (see Section 5.8.7).

5.3.1 Anamnesis and clinical examination

A thorough anamnesis and clinical examination [DMKC$^+$09] [DKCC$^+$10] was performed by two experienced orthopedic surgeons. The dancers were asked to complete a questionnaire about the presence

of pain, activities which triggered the pain, and on the chronological relation of the pain with their dancing activity. The passive ROM of the articulation of the hip in the different directions (flexion/ extension, abduction/ abduction, internal/ external rotation) was clinically determined using a double-armed goniometer. An anterior impingement test in flexion, internal rotation and adduction was also performed.

7 dancers complained of inguinal hip pain while dancing only. Pain could be reproduced by the anterior impingement test for 3 of them. The dancers could be divided into 3 groups:

1. Pain and lesions on MRI (6 dancers).
2. Pain and normal MRI (1 dancer).
3. No pain but lesions on MRI (4 dancers).

No correlation between symptoms and lesions on MRI was thus observed. Dancer's hip ROM was normal in flexion/ extension and abduction/ adduction, but internal rotation tended to be lower and external rotation higher than normal, in relation to the "turnout" position (i.e., the basic position on which all ballet movement follows). No difference of ROM between the 3 groups was noted.

5.3.2 MRI examination

The dancers were MRI scanned with a 1.5-T system (Avanto, Siemens Medical Solutions, Erlangen, Germany). The images were acquired in the supine position and were also used to reconstruct the hip joint 3D models (bones and soft tissues) of the subjects. Two musculoskeletal radiologists performed a consensus reading blinded to the clinical examination. For each subject, acetabular cartilage lesions and labral lesions were assessed and documented, including locations and extents. The presence of subchondral acetabular or femoral bony abnormalities (e.g., cysts) and the presence of a herniation pit (a round cystic lesion at the anterior aspect of the femoral neck) were reported.

Based on the assessment of the MRI scans, three types of lesions were found [DMKC$^+$09] [DKCC$^+$10] (Figure 5.1):

- Degenerative labral lesions.
- Cartilage thinning associated with subchondral cysts.
- Pits in superior or posterosuperior position.

For more than 80% of the dancers' hips presenting lesions, labral and acetabular damages were diagnosed in the superior (61% and 77%, respectively) and posterosuperior parts (22% and 8%, respectively) of the acetabular rim. Fibrocystic changes (herniation pits) were found in 11 hips, 9 being located in a superior or posterosuperior position (81%). Eventually, the same types of lesions were found for symptomatic and asymptomatic dancers.

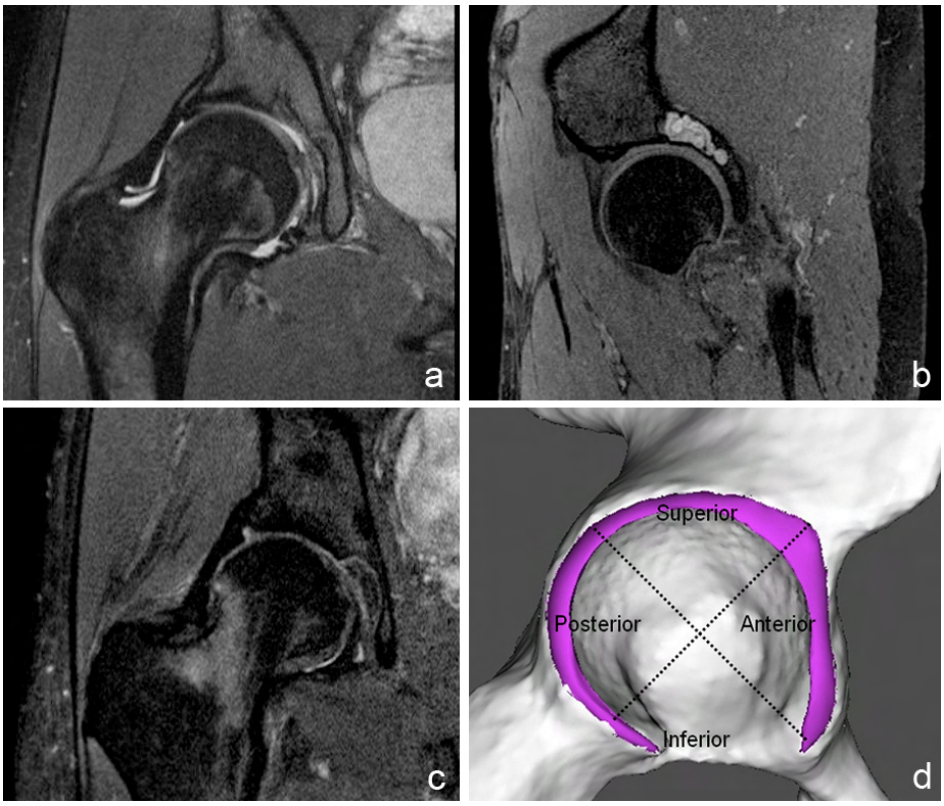

Figure 5.1: a,b,c) Types of lesions found in dancers: degenerative labrum (a), cartilage thinning associated with subchondral cysts (b), herniation pit (c) d) Spatial partitioning of the acetabular region in quadrants to report the location of lesions.

5.3.3 Morphological analysis

The normality of the dancers' hips was measured according to radiographic criteria. Under the collaboration with radiologists and orthopedists, we developed tools to quantify morphological features related to the femoral head and the acetabulum. The morphology of the hip is well described by selected anatomical parameters:

One important parameter is the computation of the acetabular version that identifies the orientation

of the opening of the acetabulum. This measure is an indicator of pincer FAI [PMD$^+$06]. We have implemented the standard measurement method from [RLK99], in a fully automatic fashion. It is based on the angle between the sagittal direction and lines drawn between the anterior and posterior acetabular rim, at different heights (Figure 5.2a). The angle is considered as positive when inclined medially to the sagittal plane (anteversion) and negative when inclined laterally to the sagittal plane (retroversion). Normal hips are anteverted. Contrary to [RLK99], we use the anatomical axis of the 3D reconstruction of the acetabulum (i.e., the pelvic frame) instead of a reference axis based on MRI slices. Thus, our results are independent from the patient positioning in the magnet bore.

Another indicator of pincer FAI is the acetabular depth [PMD$^+$06]. If the acetabulum is too deep (i.e., *coxa profunda*), pincer FAI are more favorable to occur. The depth of the acetabulum is defined as the distance in mm between the center of the femoral head (O) and the line $AR-PR$ connecting the anterior (AR) and posterior (PR) acetabular rim (Figure 5.2b). The value is considered as positive and normal if O is lateral to the line $AR-PR$. This measure requires an accurate identification of O. Thus, our method automatically fits a sphere to approximate the femoral head, so as to simplify and reduce errors in typical manual measurement.

A standard parameter related to the femur geometry is the femoral alpha (α) neck angle that is used for detecting cam FAI [PMD$^+$06]. The α angle is measured in 8 positions around the femoral neck using radially reformatted images superimposed on the 3D reconstruction model to make sure being in the femoral neck axis. We have implemented the measurement method from [NWS$^+$02]. The α angle is being defined by the angle formed by the line $O-O'$ connecting the center of the femoral head (O) and the center of the femoral neck (O') at its narrowest point, and the line $O-P$ connecting O and the point P where the distance between the bony contour of the femoral head and O exceeds the radius (r) of the femoral head (Figure 5.2c). Deviation from the normal geometry is usually associated with larger α angles ($> 55°$). As for the acetabular depth, this measure requires an accurate identification of O. Therefore, the same method is used to automatically fit a sphere approximating the femoral head.

In addition to those cam/ pincer indicators, two measurements were performed to verify if the dancers' hips had any other morphological abnormalities. The first measure is the neck-shaft angle (Figure 5.3a). A *coxa vara* is diagnosed, whereby the angle between the femoral neck and the shaft of the femur is reduced to less than 120°. A *coxa valga* is identified if the angle is bigger than 135°. In both cases, these bony deformities induce a modification of the joint stability and ROM.

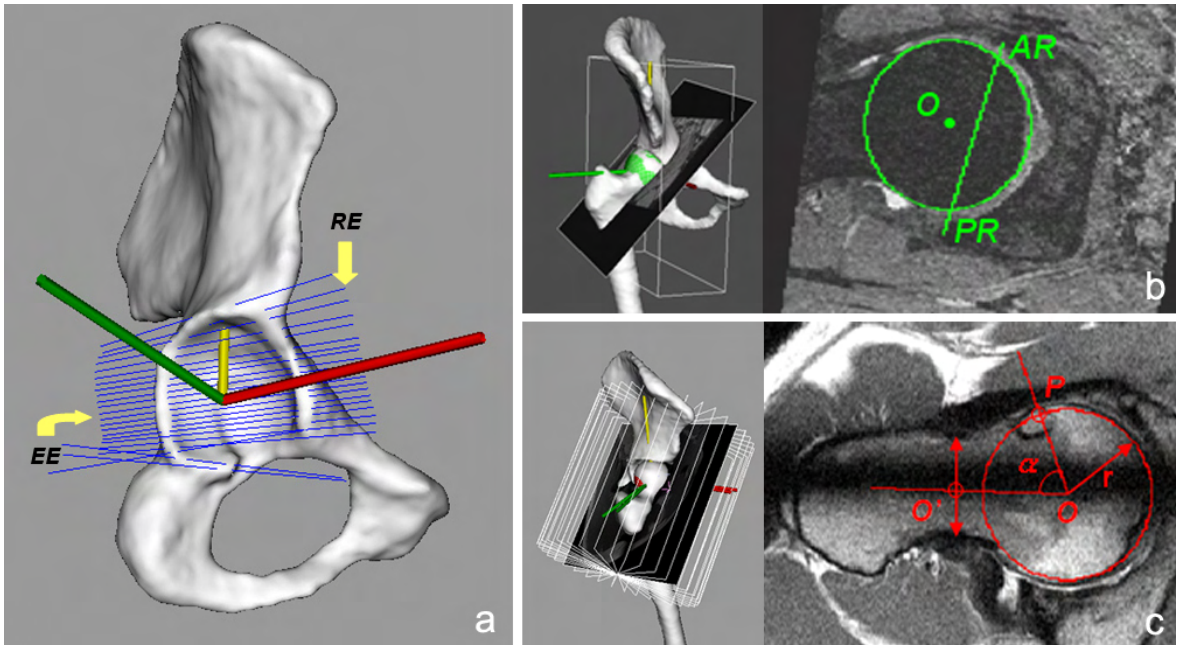

Figure 5.2: a) Computation of the acetabular version based on 3D reconstruction; roof edge (RE) and equatorial edge (EE) are lines drawn between the anterior and posterior acetabular edges, defining the orientation of the acetabular opening proximally and at the maximum diameter of the femoral head respectively (arrows) b) Definition of the acetabular depth (right) on a transverse oblique MR image (left) c) Definition of the α angle (right) on a radial MR image (left), illustrating a cam type morphology ($\alpha = 85°$).

The second measure is related to the torsional relationship of the femur to the pelvis, called the femoral neck torsion. This is defined by the angle formed by the line $O - O'$ connecting the center of the femoral head (O) and the center of the femoral neck (O') at its narrowest point, and the line $MC - LC$ connecting the medial condyle (MC) and the lateral condyle (LC). This angle is calculated in the axial plane by superimposing MR images taken at different heights (Figure 5.3b). In the normal subject, the head and neck of the femur are angulated by $10 - 14°$ relative to the femoral condyles. When the angle is superior, we speak about antetorsion and about retrotorsion otherwise.

All the dancers' hips were analyzed, according to those 5 measures. No cam/ pincer morphology was identified and it was concluded that all the measured hips were anteverted, with a positive depth and a normal α angle [DMKC$^+$09] [DKCC$^+$10]. No other morphological abnormalities were detected and no difference of morphology between the 3 groups was noted (see Section 5.3.1). Table 5.2 summarizes the results of our morphological analysis. For the α angles, only the more significant measures (in the anterior and anterosuperior planes) are reported.

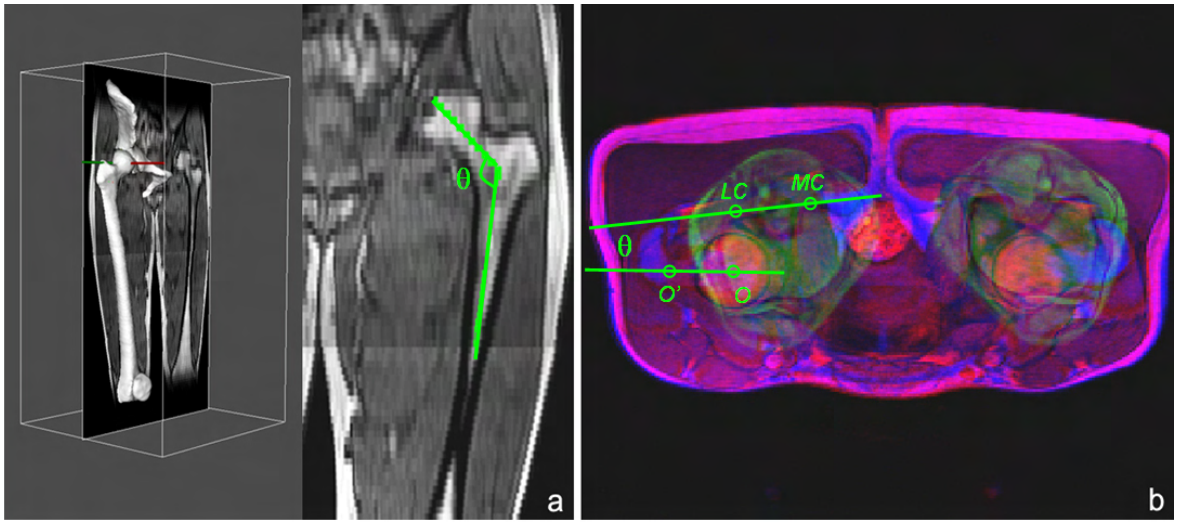

Figure 5.3: a) Computation of the neck-shaft angle (right) on a frontal MR image (left), illustrating a normal morphology ($\theta = 132°$) b) Definition of the femoral neck torsion. The torsion angle is calculated in the axial plane by superimposing MR images taken at different heights (each image is stored in a different color channel).

Measures	**Min**	**Mean ± Std. Dev.**	**Max**
Acetabular version	0.34	7.02 ± 3.41	15.67
Acetabular depth	4.64	8.14 ± 1.27	10.26
α angle (anterior)	36.52	45.32 ± 4.13	53.85
α angle (anterosuperior)	34.88	45.14 ± 6.02	55
Neck-shaft angle	123.71	133.03 ± 5.07	144.11
Femoral neck torsion	3.68	9.87 ± 3.99	17.62

Table 5.2: Morphological analysis ($N = 22$ hips).

5.4 Motion capture protocol

After MRI scanning and clinical evaluation, the 11 dancers were optically motion captured with our Vicon system. To track their motion, we used the markers configuration described in Section 4.2.1. Data from the subjects were acquired during 6 dancing movements (Figure 5.4): arabesque, développé devant, développé à la seconde, grand écart facial, grand écart latéral and grand plié. These movements were chosen, because they required and combined extreme hip flexion and/ or abduction

with rotation. Moreover, they seemed to create significant stress in the hip joint, according to the dancers' experience.

Figure 5.4: Recorded dancing movements: a) arabesque b) développé devant c) développé à la seconde d) grand écart facial e) grand écart latéral f) grand plié.

The volunteers were subsequently 3D body scanned to proceed with anatomical calibration (see Section 4.3) and the hip joint kinematics was computed from the recorded markers trajectories, using our skin artifacts correction method (see Section 4.4). Figure 5.5 shows the computed dancing postures for the subject #1.

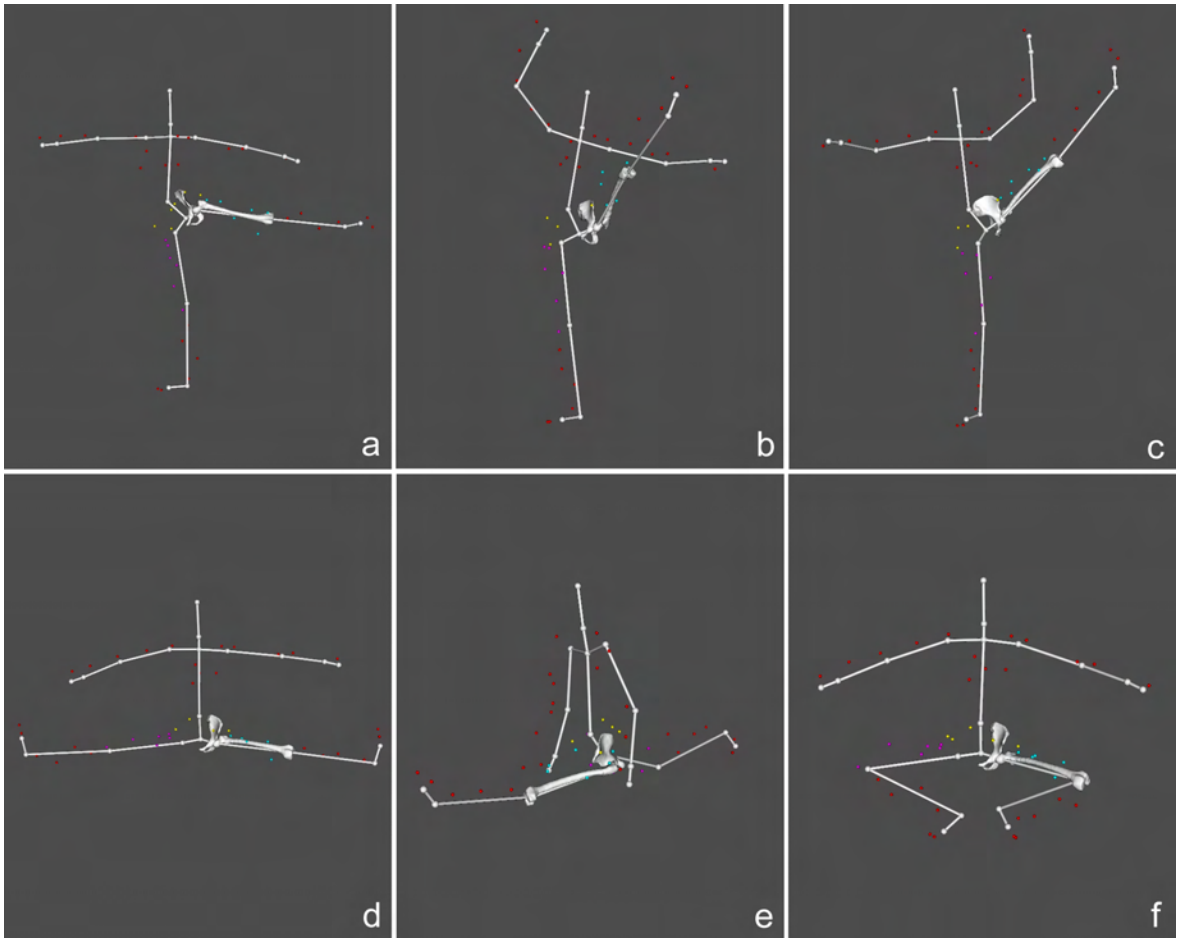

Figure 5.5: Computed dancing postures for the subject #1 (here the left hip): a) arabesque b) développé devant c) développé à la seconde d) grand écart facial e) grand écart latéral f) grand plié.

5.5 Range of motion quantification

With the use of motion capture, the active ROM of the hip joint can be accurately determined, which is clinically not possible. Moreover, a dynamic study of the hip joint in extreme positions, such as the ones regularly assumed by the dancers, has never been performed. Thus, no data related to extreme active hip ROM exists in the literature. To address this, we quantified for the 6 recorded dancing movements the ROM of each dancer.

The ROM is calculated at each point of the motion using the pelvic and femoral coordinate systems. In fact, bone relative transforms are obtained from motion capture data, thanks to our bone pose estimation algorithm. Those relative transformations are then converted to global bone transforms through Equation 3.22, and the hip joint kinematics is computed from Equation 3.19. Finally, standard

medical joint angles are easily determined from the resulting matrix $\mathbf{R}_{HF}$. The computed ROMs are reported by movement in Section 5.8.

5.6 Hip joint congruency quantification

It is unknown whether the femoral head and acetabulum are congruent in extreme positions. Thus, the congruency of the hip joint was verified for each dancer and for the 6 recorded dancing movements, thanks to our motion capture simulation.

When computing the kinematics of the hip joint, we have seen that the position of the femur was corrected to discard possible collisions with the hip bone during extreme motion (third component of our skin artifact minimization method, see Section 4.4.3). This correction corresponds to a translation of the HJC of vector $\mathbf{D_{HJC}}$ in the femoral frame. By making reference to this vector, the relative position between the hip and femur bones is described at each point of the motion. This vector therefore provides numerical information about joint subluxation (Figure 5.6). Findings concerning the congruency of the dancers' hips during the different recorded movements are reported in Section 5.8.

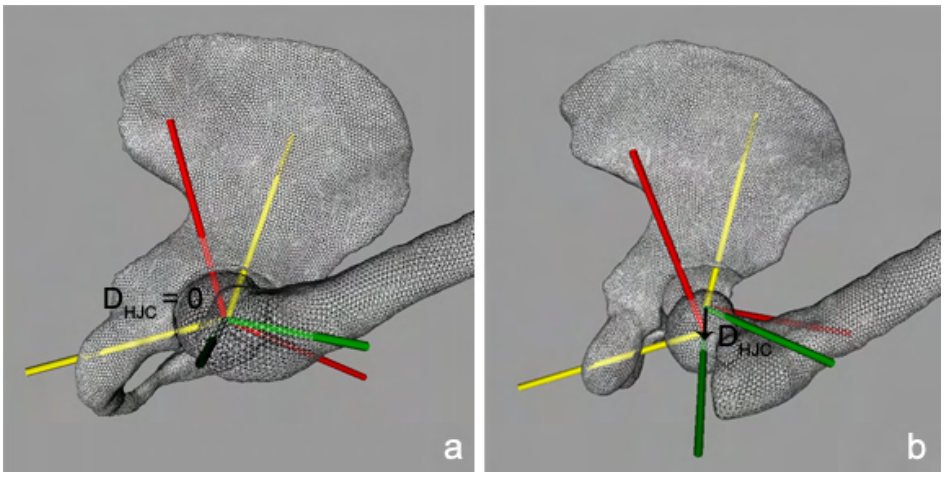

Figure 5.6: The vector $\mathbf{D_{HJC}}$ used to quantify the congruency of the hip joint: a) the translation of the HJC is null and the joint is thus congruent b) the translation of the HJC denotes a subluxation.

5.7 FAI detection

According to [TGB+08] and to the FAI theory, hip damages occur at the zone of femoroacetabular impingement. However, the concurrence of the actual impingement zone and resulting joint damage in the same patient has not yet been confirmed. Moreover, there is a lack of validated non-invasive methods to ascertain impingement during motion. To address this issue, we developed a FAI detection algorithm [MTCS08] [CLMT08] [CSKC+09] to accurately locate the region of conflict between the joint tissues. The 6 recorded dancing movements were investigated and the results were subsequently compared to the MRI findings (see Section 5.8.7). Our FAI detection algorithm works as follows:

Individual impingement zones are automatically detected and calculated in real-time over the full range of motion. While visualizing the dancer's hip joint in motion, collision detections are performed to locate abnormal contacts between the proximal femur and the labrum (see Figure 5.7). For fast computation, a uniform-level octree subdivision [GLM96] is used for the femur model and the following algorithm is applied: let us consider Φ being the labrum and Γ the femur. The two meshes are defined by a set of points $\Phi = \{P_i \in \mathbb{R}^3\}_{i=1}^n$ and $\Gamma = \{Q_i \in \mathbb{R}^3\}_{i=1}^n$, respectively. First, we project each point P_i onto Γ, yielding the projected point $P_{i\perp}$. Then, P_i is defined as being inside, and therefore colliding, if $\mathbf{P_iP_{i\perp}}.\mathbf{N_{P_{i\perp}}} > 0$ where $\mathbf{N_{P_{i\perp}}}$ is the outward normal at $P_{i\perp}$.

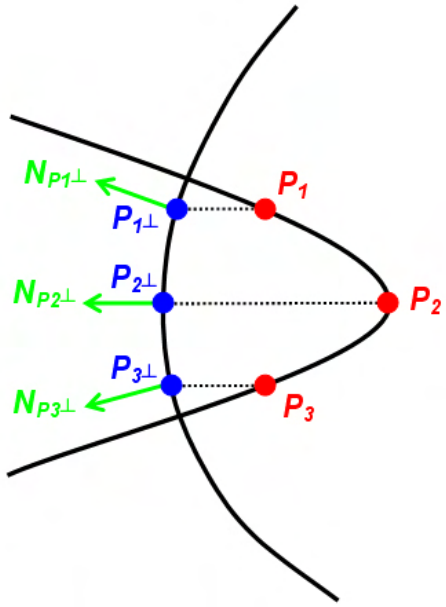

Figure 5.7: 2D schematic view of the FAI detection algorithm. The penetration depth is defined for each P_i by the norm of the vector $\mathbf{P_iP_{i\perp}}$ and determines the topographic extent (in mm) of the labrum compression.

To estimate the overall FAI, the surface-to-surface distance (i.e., penetration depth) is computed. This distance is defined for each P_i by the norm of the vector $\mathbf{P_i P_{i\perp}}$ and determines the topographic extent (in mm) of the labrum compression. Moreover, the visualization of the penetration depth distribution on the surface of the labrum is represented using a color table (Figure 5.8a). To describe and document the exact location of the impingement zone, the acetabulum is divided into 8 sectors (position 1 anterior, position 2 anterosuperior, position 3 superior, position 4 posterosuperior, position 5 posterior, position 6 posteroinferior, position 7 inferior, position 8 anteroinferior), as depicted in Figure 5.8b. The impingement zones are hence assigned numbers correlating with their position. The simulation results are presented and discussed in the coming section.

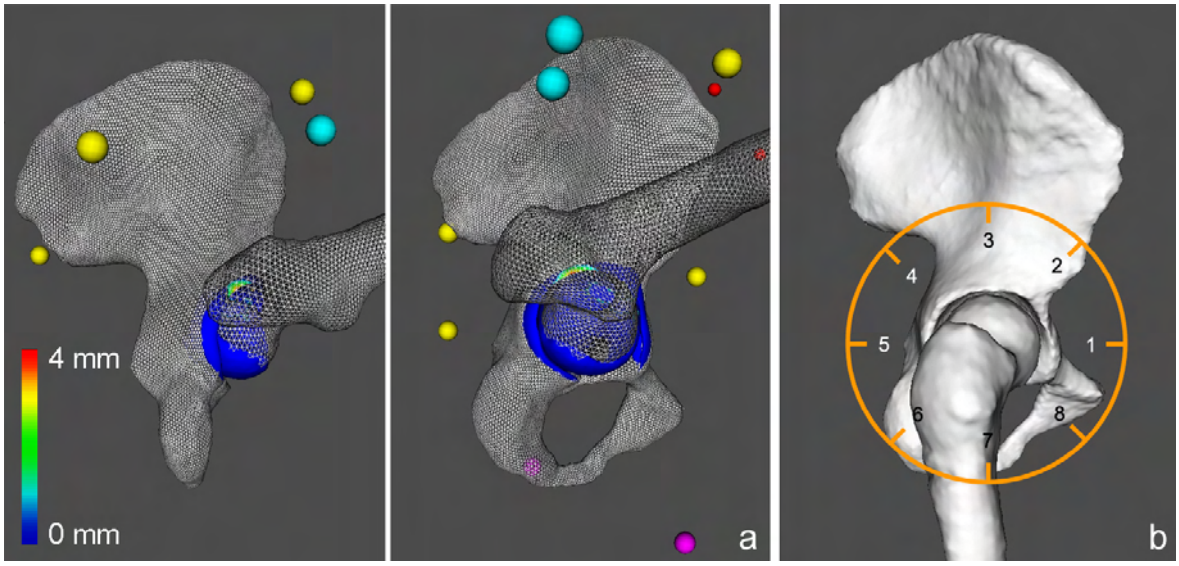

Figure 5.8: a) Visualization of the FAI region during extreme motion (posterior and lateral views). The colors represent the penetration depth distribution b) Acetabulum divided into 8 sectors (position 1 anterior, position 2 anterosuperior, position 3 superior, position 4 posterosuperior, position 5 posterior, position 6 posteroinferior, position 7 inferior, position 8 anteroinferior) to report the location of the impingement zone.

5.8 Statistical analysis and results

A statistical analysis was conducted for each of the 6 recorded dancing movements. We calculated the frequency of impingement, subluxation and created histograms displaying the frequency of distribution of the zone of impingement. We computed the mean values and the standard deviations of the penetration depth, subluxation and range of motion according to the 3 standard anatomical angles. We finally compared the simulation results with the clinical findings.

As shown in Table 5.3, dancing involves intensive hip flexion and abduction (except the arabesque where the hip is in extension and the grand écart latéral where one hip is in extension). For all movements, no significant left-right differences were noted. Globally, the angles showed low standard deviations, suggesting that movements were repeated similarly across dancers.

Movements	**Left hip**		**Right hip**	
	Mean	**Std. Dev.**	**Mean**	**Std. Dev.**
Arabesque				
Flex / Ext	0 / 0 / 28.42	10.26	0 / 0 / 23.48	11.03
Abduction	18.73	7.88	21.58	7.71
IR / ER	0 / 0 / 27.78	13.62	0 / 0 / 22.74	20
Développé devant				
Flex / Ext	88.47 / 0 / 0	14.59	92.55 / 0 / 0	15.2
Abduction	24.99	14.96	24.28	10.37
IR / ER	0 / 0 / 2.72	29.95	0 / 0 / 0.73	11.71
Développé à la seconde				
Flex / Ext	84.96 / 0 / 0	18.61	95.25 / 0 / 0	16.61
Abduction	49.96	5.21	49.28	6
IR / ER	18.39 / 0 / 0	17.6	22.18 / 0 / 0	15.01
Grand écart facial				
Flex / Ext	62.27 / 0 / 0	23.41	72.83 / 0 / 0	18.52
Abduction	73.12	6.05	71.52	8.46
IR / ER	0 / 0 / 2.37	25.15	9.98 / 0 / 0	24.54
Grand écart latéral (front leg)				
Flex / Ext	116.4 / 0 / 0	18.46	117.07 / 0 / 0	5.85
Abduction	38.88	13.58	34.68	14.02
IR / ER	35.76 / 0 / 0	15.06	37.99 / 0 / 0	8.94
Grand écart latéral (back leg)				
Flex / Ext	0 / 0 / 31.21	6.65	0 / 0 / 42.86	13.37
Abduction	25.81	5.74	29.87	8.42
IR / ER	0 / 0 / 27.37	13.8	0 / 0 / 28.16	18.24
Grand plié				
Flex / Ext	52.99 / 0 / 0	13.39	62.19 / 0 / 0	18.3
Abduction	68.28	7.68	64.92	8.09
IR / ER	0 / 0 / 10.22	11.34	0 / 0 / 11.22	18.49

Table 5.3: Range of motion of the hip joint by movement. Values are reported in *deg*.

Findings concerning impingement and subluxation are presented and discussed below for each recorded dancing movement. Moreover, Table 5.4 summarizes mean values and standard deviations of computed penetration depths and subluxations by movement. Figures 5.10 and 5.11 also graphically compare the frequency of impingement and subluxation by movement.

5.8.1 Arabesque

For the 11 dancers analyzed, neither FAI nor subluxation were detected, while performing this movement. We believe this may have a kinematical interpretation: since only low amplitude angles are required to reproduce this motion, this does not create significant stress in the hip joint.

5.8.2 Développé devant

Impingements were observed for 24% of the dancers' hips. The mean penetration depth (Std. Dev.) was $2.5mm$ ($1.2mm$). The computed zones of impingement were variably distributed between the anterior and posterior quadrant of the acetabulum (position 2 to 5 according to our documentation), as depicted in Figure 5.9a. No subluxations were noted.

5.8.3 Développé à la seconde

FAI were detected for 45% of the dancers' hips. 78% of the contacts were located in the superior or posterosuperior area of the acetabular rim (Figure 5.9b). The penetration depths were intense (mean: $3.25mm$; std. Dev.: $1.91mm$), with a peak value of $6.22mm$. Subluxations were observed in 25% of the cases, but the femoroacetabular translations were significant (mean: $4.56mm$) for all hips, as suggested by the low standard deviation ($1.14mm$). Furthermore, when a subluxation occurred, it was always correlated to an impingement.

5.8.4 Grand écart facial

While executing this movement, impingements were often observed (61% of the dancers' hips). All computed impingement zones were located in the superior or posterosuperior quadrant of the acetabulum (Figure 5.9c). The mean penetration depth (Std. Dev.) was $3.63mm$ ($2.55mm$). Moreover, this is the movement with the highest frequency of subluxation (39%) with a mean value (Std. Dev.) of $3.42mm$ ($1.6mm$). All subluxations were associated with an impingement.

5.8.5 Grand écart latéral

For the leg in flexion (front leg), the highest frequency of FAI (70% of the dancers' hips) was noted. The mean penetration depth (Std. Dev.) was $2.22mm$ ($1.83mm$). The simulation showed that all collisions occurred at the superior or posterosuperior acetabular rim (Figure 5.9d). We also found strong femoroacetabular translations (mean: $5.14mm$; std. Dev.: $1.28mm$) in 31% of the cases that were correlated to impingements.

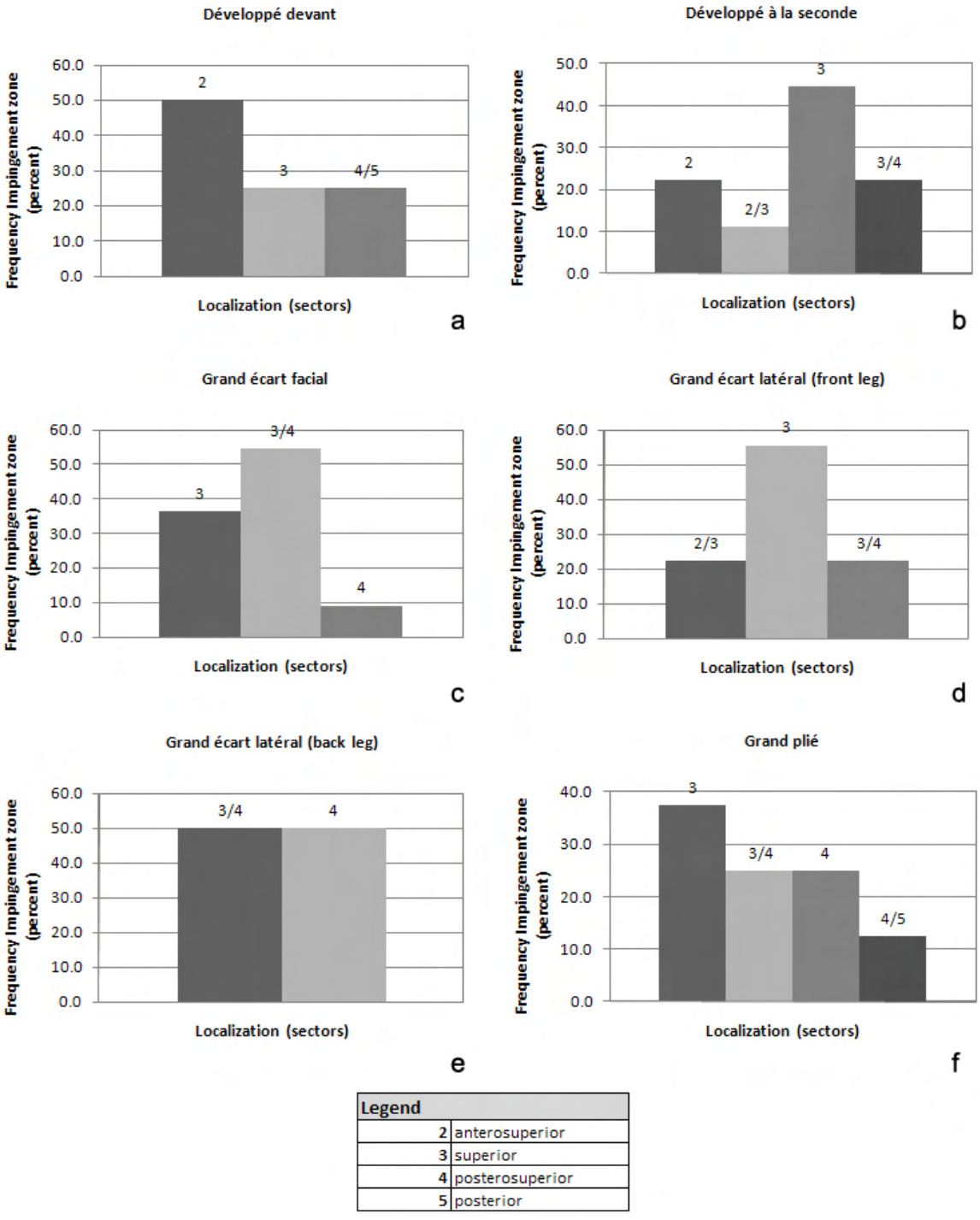

Figure 5.9: Histograms showing the distribution of frequency of the computed impingement zones for each movement: a) développé devant b) développé à la seconde c) grand écart facial d) grand écart latéral (front leg) e) grand écart latéral (back leg) f) grand plié.

For the leg in extension (back leg), the frequency of impingement was low (22% of the dancers' hips), as well as the penetration depths (mean: 1.11mm; std. Dev.: 1.33mm). The contacts were all located in the superior or posterosuperior quadrant of the acetabulum (Figure 5.9e). Only one subluxation was detected.

5.8.6 Grand plié

Impingements were observed for 44% of the dancers' hips. The mean penetration depth (Std. Dev.) was 2.47mm (1.76mm). All computed impingement zones were located in the superior or posterosuperior area of the acetabular rim, as shown in Figure 5.9f. The frequency of subluxation was low (17%) with a mean value (Std. Dev.) of 3.77mm (2.08mm). However, all femoroacetabular translations were correlated to an impingement.

Movements	**Penetration depth Mean ± Std. Dev. (range)**	**Subluxation Mean ± Std. Dev. (range)**
Arabesque	0	0
Développé devant	2.5 ± 1.2 (1.12 - 4.01)	0
Développé à la seconde	3.25 ± 1.91 (0.89 - 6.22)	4.56 ± 1.14 (3.16 - 5.57)
Grand écart facial	3.63 ± 2.55 (0.77 - 6.88)	3.42 ± 1.6 (0.93 - 5.67)
Grand écart latéral (front leg)	2.22 ± 1.83 (0.32 - 5.84)	5.14 ± 1.28 (3.33 - 6.35)
Grand écart latéral (back leg)	1.11 ± 1.33 (0.17 - 2.05)	3.15 ± 0
Grand plié	2.47 ± 1.76 (0.37 - 4.93)	3.77 ± 2.08 (1.4 - 5.29)

Table 5.4: Computed penetration depths and subluxations by movement. Values are reported in mm.

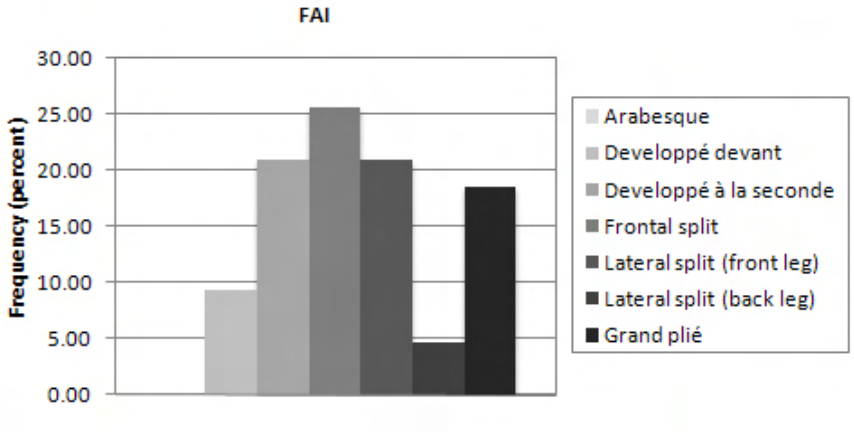

Figure 5.10: Histogram showing the frequency of impingement by movement.

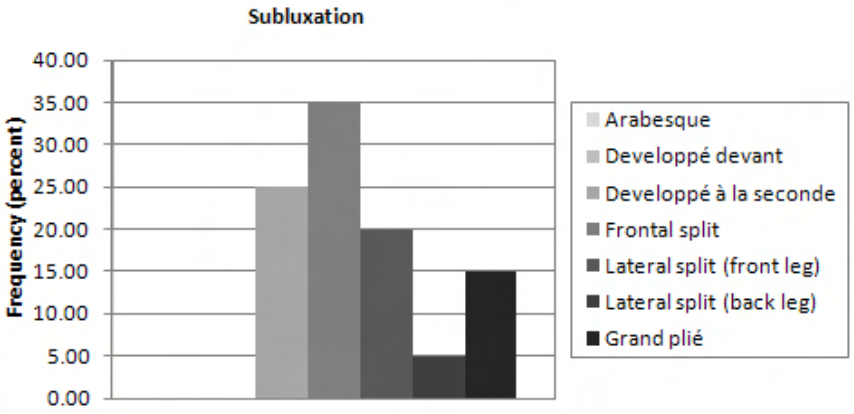

Figure 5.11: Histogram showing the frequency of subluxation by movement.

5.8.7 Comparison of simulation and clinical findings

The simulation results were finally compared with the clinical findings. After analysis, two conclusions could be drawn:

According to the clinical examination and to the literature [KRN+97] [GFB+04] [SHP+06], the passive hip ROM of dancers is normal compared to the general population, with a trend to increased flexion, abduction and external rotation. However, only trained subjects are able to assume dancing movements, such as the ones performed in ballet. As expected, this extreme motion is thus possible thanks to a combination of three articular motion patterns [CKCD+10a] [CKCD+10b]. This assertion is also confirmed by the active ROM computed from motion capture, showing that dancing requires intensive hip flexion and abduction combined with rotation.

For almost all movements, the computed zones of impingement were mainly located in the superior or posterosuperior quadrant of the acetabulum (position 3 and 4). Based on the MRI examination, the degenerative labral lesions were diagnosed in superior (61%) or posterosuperior (22%) position. The simulation results were hence relevant with respect to the MRI findings. Furthermore, it is worth mentioning that the detected lesions were typical lesions of femoroacetabular conflicts, but their locations were unusual. Indeed, resulting chondrolabral damages in the cam or pincer hip are generally located in the anterosuperior position [SSG03] [BZM+05] [BKG05] [TGB+08]. Consequently, we think that dancing implies a new superior/ posterosuperior FAI [CKCD+09] [CKCD+10a] [CKCD+10b], as depicted in Figure 5.12.

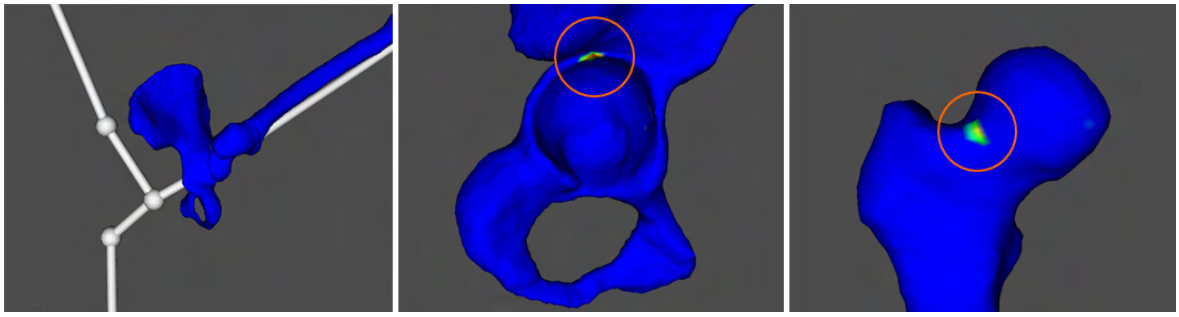

Figure 5.12: An example of superior FAI while performing a développé à la seconde (left) and the corresponding contact zones (orange circles, middle and right images) on the hip and femur bones models (the cartilages and the labrum are not shown for clarity). The type of contact is characteristic of a femoroacetabular conflict, but located in superior position.

5.9 Discussion

In this chapter, we have presented the results of a prospective study [CKCD$^+$09] [CKCD$^+$10a] [CKCD$^+$10b] conducted with female professional dancers. FAI and joint congruency were actively assessed and demonstrated *in vivo*. Without the motion capture, the hip ROM would also not have been clinically determinated with the same reliability. As far as we know, this is the first *in vivo* study of the hip joint in extreme dancing positions.

The results have been reported for 11 dancers, presenting no morphological abnormalities. The computed FAI can therefore not be imputed to any cam or pincer morphology. This already reveals that motion seems to have a direct influence on the physiology of the hip joint. Strong penetration depths were computed for all extreme movements (range: $0.17 - 6.88mm$). Knowing that the labrum has superiorly and posteriorly an average height of $6 - 7mm$ [WCCS03], our results indicate that the labrum is highly compressed during extreme motion. For all dancers' hips, FAI and subluxations occurred at the maximal hip ROM and were frequently observed. Moreover, the subluxations were always correlated to impingements, suggesting that a subluxation would occur in response to the collision between the proximal femur and the acetabular rim. These findings corroborate the fact that the hip joint undergoes a high stress during extreme motion, as it was also pointed out in previous studies [NV00] [Mas01] [MNS$^+$01] [Bin03] [MNA$^+$03] [CKH$^+$09] [GH09].

Based on our statistical analysis, the frequency of impingement and subluxation varied with the types of movement. However, four dancing movements seem to be harmful for the hip joint: the grand écart facial where the highest frequency of subluxation (39%) was observed, the grand écart latéral (front leg) where the highest frequency of FAI (70%) was noted, the développé à la seconde

and the grand plié where high penetration depths (mean: $3.25mm$ and $2.47mm$, respectively) and femoroacetabular translations (mean: $4.56mm$ and $3.77mm$, respectively) were quantified. Thanks to the motion capture, these arthrogenous movements could be identified. Our findings thus indicate that these movements should be limited in frequency during dancing class. The hip joint would be even better preserved.

Eventually, it is interesting to note that a MRI-based assessment of the congruence of the hip joint in split position was conducted at MIRALab (see [GKCMT$^+$09] for more details). Compared with our study, the femoroacetabular translations were similar (mean: $2.05 \pm 0.74mm$; range: $0.63 - 3.56mm$), but slightly lower to those we computed. One explanation could be that the hip joint kinematics computation is less accurate in motion capture than in MRI scanning. In fact, our translation errors are in the order of magnitude of the MRI bone motion tracking accuracy (see Section 4.4.4), and they thus cannot explain the discrepancies in the results. However, in the MRI study, the assessment was limited to a single static posture and did not account for joint dynamics. It is therefore understandable to obtain a higher amount of subluxation when analyzing the hip joint in active motion.

In summary, the results of this study validate our hypothesis. From our data, we conclude:

1. The practice of some dancing movements exposes the dancer's hip to recurrent impingements located in the superior or posterosuperior quadrant of the acetabulum.

2. The femoral head and acetabulum are not always congruent in typical dancing positions.

Based on the evidence, we believe that FAI and subluxation could lead to cartilage hyperpression and therefore to early OA.

Chapter 6

Conclusion

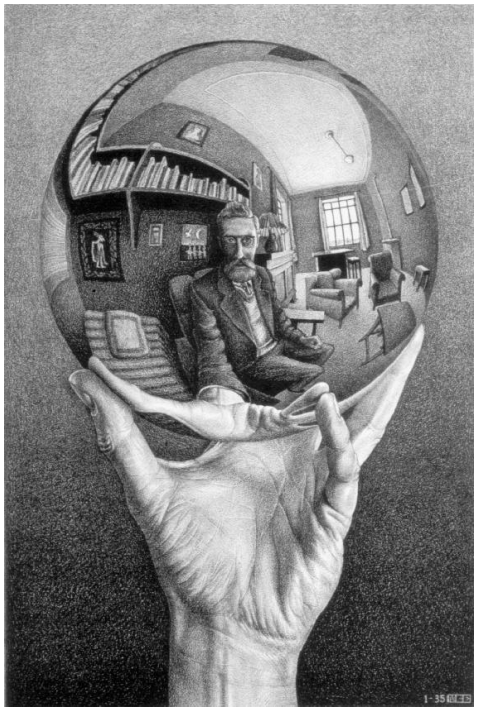

[1] M.C. Escher's "Hand with Reflecting Sphere" ©2010 The M.C. Escher Company - the Netherlands. All rights reserved. Image from `http://www.mcescher.com/` used by permission.

6.1 Contributions

In this Section, we briefly summarizes the initial goals of our work, as well as our contributions.

Osteoarthritis (OA) affects the hip joint and is among the leading causes of chronic musculoskeletal disabilities. Many causes could be at the origin of hip OA (e.g., cam/ pincer impingements, dysplasia), but the exact pathogenesis for idiopathic OA has not yet been clearly delineated. The aim of the present work was therefore to investigate the hypothesis of extreme repetitive movements as a source of chondrolabral degeneration. To verify this hypothesis, we have proposed a protocol for joint motion estimation using optical systems, where the critical issues of soft tissues artifacts and anatomical calibration are effectively addressed. Using this validated protocol, we have subsequently studied the *in vivo* motion of professional ballet dancers' hips in typical dancing positions. Our work represents one of the first attempt to model the extreme kinematical behavior of the hip articulation.

We have demonstrated the efficiency of the proposed methods [MTCS08] [CLMT08] [CAVMT09] [CSKC$^+$09] over previous techniques in the following aspects:

- **Accuracy:** through an adequate validation we have shown that the accuracy of our methods is millimeter-based. Thanks to the 3D body scanning technology and to the use of 3D models, the anatomical calibration is more precise. Unlike previous techniques applying strong kinematic constraints, our bone pose estimation algorithm allows some shifts at the joint providing a more valid simulation from a physiological point of view.

- **Robustness:** our bone pose estimation algorithm is able to handle large and various ranges of motion, as well as inter-patient variability.

- **Automation:** from little input from the user (a standard file of recorded markers' trajectories), our bone pose estimation algorithm is able to compute straightforwardly the subject's hip joint kinematics. Moreover, by exploiting geometric features of the 3D models, our anatomical calibration method is mostly automated.

- **Clinical feasibility:** compared to previous techniques being time consuming due to the several additional data acquisitions required, our motion protocol is more feasible. Indeed, it requires only one additional data acquisition (a 15 seconds scan of the subject's body surface).

- **Computational speed:** our bone pose estimation algorithm allows the real-time visualization and interaction with the data, which facilitates the analysis of complex human system.

- **Flexibility:** the proposed methods are quite generic and are not limited to a specific joint.

Thanks to our dancers' study, we have also stressed the following clinical findings [CKCD+09] [DMKC+09] [CKCD+10a] [CKCD+10b] [DKCC+10]:

- In young adults, early OA is not only the result of cam/ pincer impingements. Repetitive extreme movements could affect the development of early hip OA.
- Prolonged dancing could expose the morphological "normal" hip to recurrent superior or posterosuperior impingements and to joint subluxation.
- Some dancing movements seem to be arthrogenous: développé à la seconde, grand écart facial, grand écart latéral and grand plié. These movements should be hence limited in frequency.
- No specific morphology seems to be required for dancing. Extreme ranges of motion are possible thanks to intensive and regular training. They are the result of a combination of three articular motion patterns.

The achievements of our work have been detailed in various journals, conferences or workshop articles. Appendix D provides the complete list of publications made during this thesis work.

6.2 Limitations and future work

Despite the advances attributable to the presented methods, they present a certain number of limitations. The experience that we have acquired during this thesis let us highlight some aspects and problems that should receive a particular attention in future research. More work is also required in testing and validation. We are now reviewing weaknesses of our techniques and are proposing new directions per topic:

6.2.1 Anatomical calibration

Automation and flexibility in terms of processing and geometry respectively, are two aspects that could be even more improved regarding our anatomical calibration method. We advocate the following enhancements:

- The identification of the markers positions on the scan data could be speed up. Faster process would be achievable through spacial body's partitioning and automatic features detection techniques.

- Our registration method is based on the use of generic models. To increase its flexibility, it would be appropriate to develop a more comprehensive algorithm that is independent from the models' geometry.

6.2.2 Bone pose estimation

There is a possible extension that could be investigated regarding our bone pose estimation algorithm: instead of correcting the hip joint center when abnormal contacts occur between the hip bone and the femur, we could introduce physically-based constraints derived from continuum mechanics. The idea would be to integrate forces (loads) and velocities to find the joint equilibrium for each instant frame, and consequently to have a more accurate approximation of the hip joint center's position. Our method would be no longer geometrically based, but driven by a more advanced mechanical simulation able to model the dynamic behavior of the articulation. However, loads should be available, which can be difficult to measure according to the motor task (e.g., dancing movements).

6.2.3 Femoroacetabular impingement detection

While we have focused on the geometric interpretation of contact between the joint tissues, we believe that our simulation could benefit from biomechanical models:

- Our simulation ignores soft tissues and potential bone deformation under loads. Taking into account the mechanical properties of the bones, cartilages and labrum could provide information about the contact pressure distribution in the joint, and thus contribute to a better understanding of the pathology.
- Our simulation is also limited to the labrum (bone/ cartilage contact). We have noticed some difficulties in estimating the contact between the femoral and acetabular cartilages, because of their thin thickness (i.e., the models entirely interpenetrate). Indeed, the penetration depth, as a geometric measure, cannot be accurately and robustly computed for those cartilages without accounting for their deformation.

Hence, future work should include a physically-based simulation of the bony and chondrolabral structures. This is actually the topic of another PhD thesis at MIRALab.

6.2.4 Validation

Due to measurement difficulties (for instance, no access to the bone kinematics) and musculoskeletal system complexity, functional models are difficult to validate. Extensive testing and data collection

are mandatory, which could not be exhaustively achieved during this thesis. We recommend the following additional validation tests:

- To improve the validation of our anatomical calibration method, new tests should be performed with subjects of different corpulence.
- To extend the validation of our bone pose estimation algorithm, further experiments could be carried out to estimate the error made on the hip joint kinematics during extreme movements. For example, these experiments could be conducted in open MRI.

Appendix A

Acronyms

Acronyms used throughout the text and their definition:

AF: Anatomical Frame

AL: Anatomical Landmark

ASIS: Anterior Superior Iliac Spine

CAST: Calibrated Anatomical System Technique

CFA: Common Factor Analysis

CT: Computed Tomography

CTF: marker Cluster Technical Frame

DOF: Degree Of Freedom

FAI: FemoroAcetabular Impingement

FE: Femoral Epicondyle

GT: Greater Trochanter

HF: Head of the Fibula

HJC: Hip Joint Center

ISB: International Society of Biomechanics

LE: Lateral Epicondyle

LM: Lateral Malleolus

MoCap: Motion Capture

MRI: Magnetic Resonance Imaging

MSDs: Musculoskeletal Disorders

OA: Osteoarthritis

PCA: Principal Component Analysis

PSIS: Posterior Superior Iliac Spine

RMS: Root Mean Square

ROM: Range Of Motion

RSA: Röntgen Stereophotogrammetric Analysis

SQP: Sequential Quadratic Programming

STA: Soft tissue artifact

STC: Standardisation and Terminology Committee

SVD: Single Value Decomposition

Appendix B

Osteoarthritis (OA)

This description was gathered on the web on the courtesy of Medical Multimedia Group LLC, eOrthopod[1]:

Osteoarthritis (sometimes referred to as degenerative, or wear-and-tear, arthritis) is a common problem for many people after middle age. OA commonly affects the hip joint. The main problem in OA is the degeneration of the articular cartilage. Articular cartilage is the smooth lining that covers the surfaces of the ball-and-socket joint of the hip. The cartilage gives the joint freedom of movement by decreasing friction. When the articular cartilage degenerates, the subchondral bone is uncovered and rubs against bone. Small outgrowths called bone spurs or osteophytes may form in the joint.

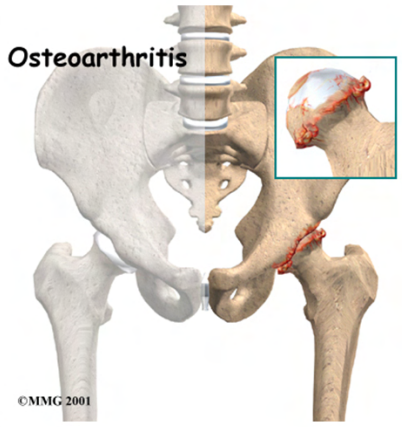

Figure B.1: Osteoarthristis condition. Image courtesy of Medical Multimedia Group LLC, eOrthopod.

[1] `http://www.eOrthopod.com/`, accessed November 2009

Causes: OA of the hip can be caused by a hip injury earlier in life. Changes in the movement and alignment of the hip eventually lead to excessive wear and tear on the joint surfaces. The alignment of the hip can be altered from a fracture in the bones around or inside the hip. Cartilage injuries, infection, or bleeding within the joint can also damage the joint surface of the hip. Scientists believe genetics makes some people prone to developing OA in the hip. Problems in the subchondral bone may trigger changes in the articular cartilage: some medical conditions can make the subchondral bone too hard or too soft, changing how the cartilage normally cushions and absorbs shock in the joint. Avascular necrosis (AVN) is another cause of degeneration of the hip joint. In this condition, the femoral head (the ball portion of the hip) loses a portion of its blood supply and actually dies.

Symptoms: the symptoms of hip OA usually begin as pain while putting weight on the affected hip. The affected hip is felt stiff and tight due to a loss in its range of motion. As the condition becomes worse, pain may be present all the time.

Nonsurgical treatment: OA cannot be cured, but medicines are available to ease symptoms and to slow down the degeneration of the joint: mild pain reliever and anti-inflammatory medication. Cortisone injection may be prescribed but may actually speed up the process of degeneration. Physical therapy can help to learn how to control symptoms: rest, heat, topical rubs, range of motion, strengthening and stretching exercises. A cane may be needed to ease pressure when walking.

Surgery:

- Arthroscopy: surgeons can use an arthroscope (miniature TV camera inserted into the joint though a small incision) to check the condition of the articular cartilage in a joint. At the same time, joint cleaning can be performed by removing loose fragments of cartilage. Another method involves simply flushing the joint with a saline solution, after which some patients report relief. Hip arthroscopy is relatively new, and it is unclear at this time which patients will benefit.

- Osteotomy: when the alignment of the hip joint is altered from disease or trauma, more pressure than normal is placed on the surfaces of the joint. This extra pressure leads to more pain and faster degeneration of the joint surfaces. Angle realignment (osteotomy) aims at spreading forces over a larger surface in the hip joint. In this procedure, the bone of either the pelvic socket or femur is cut, and the angle of the joint is changed. In some cases, it can result in shifting pressure to the other healthier parts of the hip joint.

- Bone resurfacing: femoral bone resurfacing can last from 10 to 20 years and is easier on the patient than total hip replacement. Particularly for younger people and persons who have

complications from taking steroids, this is a good option. Total hip replacement is often viewed as a last resort and femoral bone resurfacing can delay the need for hip replacement for many years.

- Artificial hip replacement: this is the ultimate solution for advanced hip OA. Surgeons prefer not to put a new hip joint in patients less than 60 years old. This is because younger patients are generally more active and might put too much stress on the joint, causing it to loosen or even crack. A revision surgery to replace a damaged joint is harder to do, has more possible complications, and is usually less successful than a first-time joint replacement surgery.

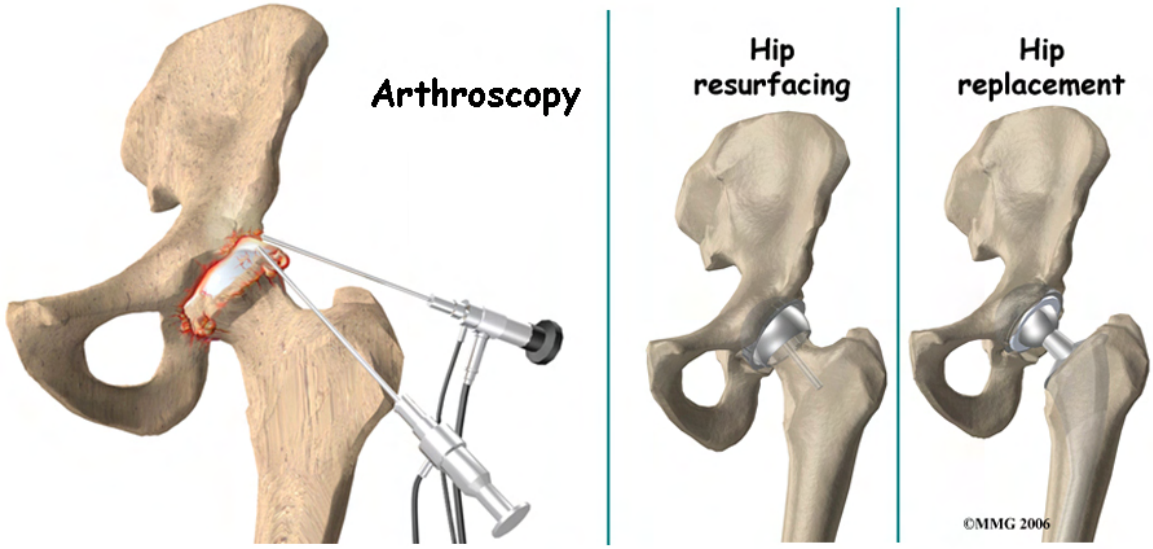

Figure B.2: Surgical procedures. Image courtesy of Medical Multimedia Group LLC, eOrthopod.

Rehabilitation: shortly after surgery, walking is practiced using walker or a pair of crutches. Exercises are used to improve muscle tone and strength in the hip and thigh muscles and to help prevent the formation of blood clots. In addition, a therapist helps the patient to maximize hip strength, and restore a normal walking.

Appendix C

Software implementation and functionalities

General implementation

Developments have been performed in conventional C++ using Microsoft Visual Studio .NET with additional libraries:

- The open source toolkit VTK (©1993-2008 Ken Martin, Will Schroeder, Bill Lorensen, All rights reserved).
- The Berkeley DB XML API[1], an embedded XML database with XQuery-based access.
- The Microsoft Foundation Class (MFC).

All tests presented in this thesis have been performed on a Quad Core of $2.33GHz$ with $4Gb$ of memory and a GeForce 9800 GTX graphics card, under Microsoft Windows XP.

To allow future use of our application, we have chosen to completely separate the interface from the methods. All functions can be accessed via a main C class to facilitate the reuse, the parameterization and the automation.

The following diagram shows the basic relationships between the developed C classes (in italic):

[1] `http://www.oracle.com/database/berkeley-db/index.html`, accessed November 2009

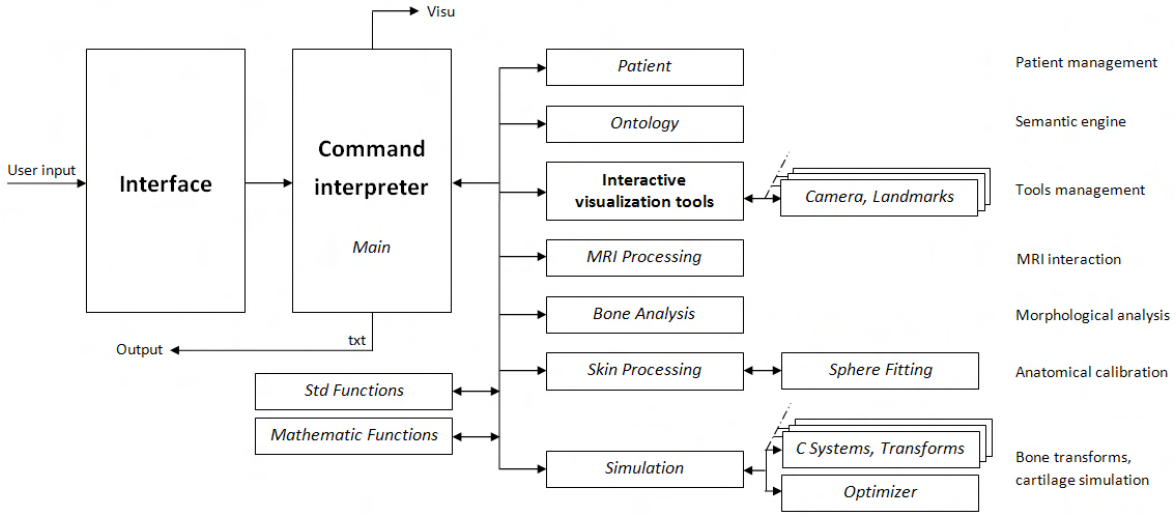

Figure C.1: System overview.

Interface and functionalities

As mentioned in Section 4.6, we have developed a semantic-driven platform able to centralize and structure the multimodal data inputs and the medical knowledge in a coherent and unified manner. The platform is driven by a medical ontology that takes into account not only the anatomy, but also the functionalities of the musculoskeletal system. Our system integrates conventional diagnostic support (e.g., MRI, morphological measurement tools), visualization features and simulation functions (e.g., motion capture, FAI detection). Our application can be divided into several components:

The 2D and 3D Windows

The main components of our application are the 2D and 3D Windows. The 2D Window displays MR images, whereas the 3D Window displays 3D objects.

How to handle the 2D Window:

- Left mouse button to adjust the brightness/ contrast of the image.
- Middle mouse button to interactively place landmarks.

How to handle the 3D Window:

- Rotation: by positioning the pointer within the dark area, left mouse button to the left or right to rotate vertically and up and down to rotate horizontally. Horizontal and vertical rotation can be combined in a single mouse movement.

- Zoom: by holding down right mouse button, move up to zoom in or down to zoom out.
- To move the 3D objects, middle mouse button: left, right, up, down.
- To bring the 3D objects back to center, hold `R` key.

Figure C.2: The 2D and 3D Windows.

The Patient loader

After having launched the application, the first step consists in selecting the patient to be analyzed.

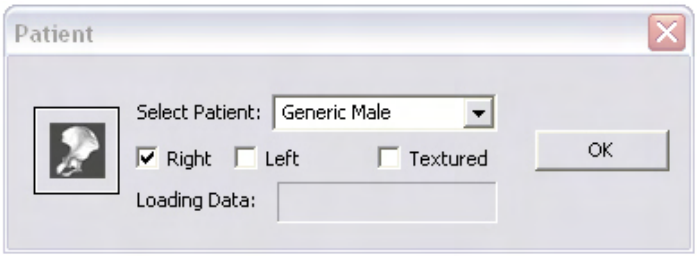

Figure C.3: Patient loader.

Using the Patient loader, the user can:

- Select a patient in the list.

- Choose the side (right or left leg).
- Enable 3D models' texturing. Default is without textures.
- Load the patient's data (OK button). N.B.: Only the 3D models of the bones and the MRI are loaded at this stage.

The Ontology browser

The user has a direct access to the ontology. He/ she can browse the ontology's classes and dynamically load the 3D objects (i.e., 3D model or 3D segmented data) associated to the selected concept.

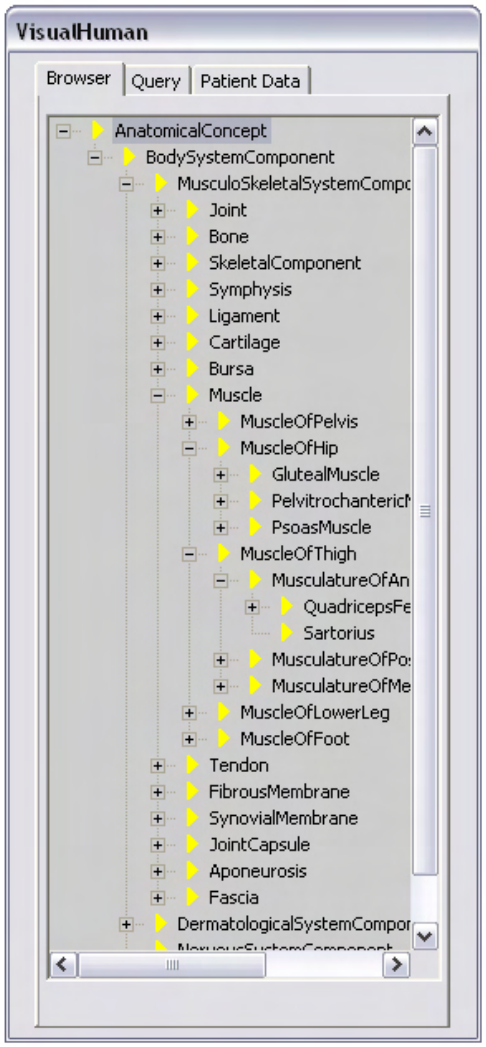

Figure C.4: Ontology browser.

The Query dialog box

The user can query the ontology using the basic or advanced search engine. By providing the appropriate input, the system finds and displays all concepts corresponding to the user request. Then, the user can load the 3D objects (i.e., 3D model or 3D segmented data) associated to the selected concept.

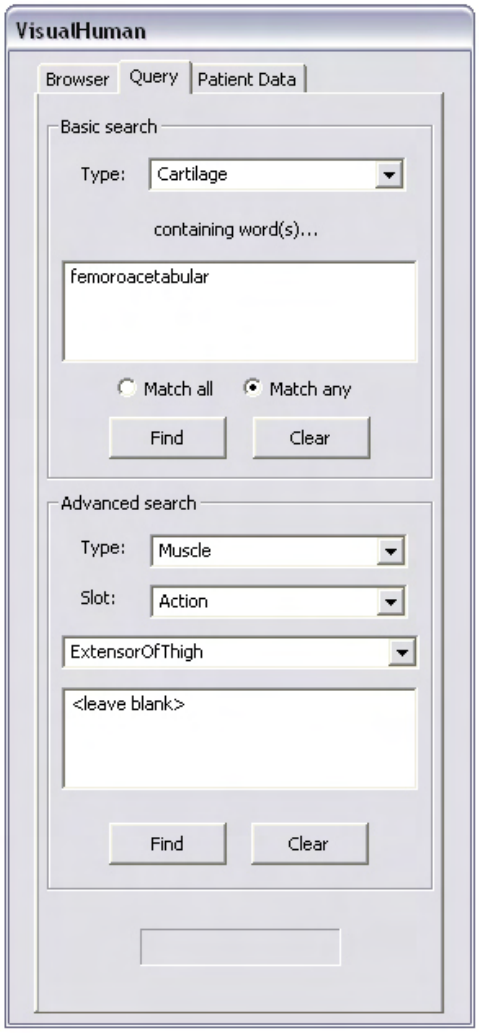

Figure C.5: Query dialog box.

- `Basic search`: the user specifies the type of organ, keywords and matching type (e.g., any cartilages containing the keyword "femoroacetabular").
- `Advanced search`: the user specifies the type of organ, its property (slot) and value (e.g., the muscles acting as extensor of the thigh).

The Patient's data browser

Instead of loading the patient's data from the ontology, the user can browse the data from a list. This list is organized by data type (e.g., 3D models, medical images, motion capture data) and by organs (e.g., muscles, cartilages). When the user selects a data, the system loads it in the application.

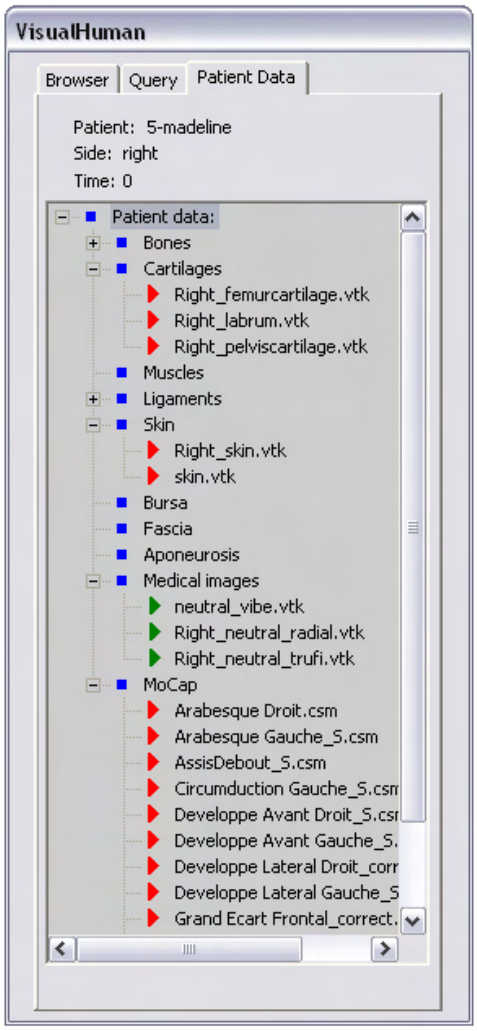

Figure C.6: Patient's data browser.

The Objects list and Organ properties dialog boxes

The user can ask the system to list all 3D objects loaded in the application. Then, he/ she can retrieve information related to the anatomical and functional properties of the selected object, by querying the ontology.

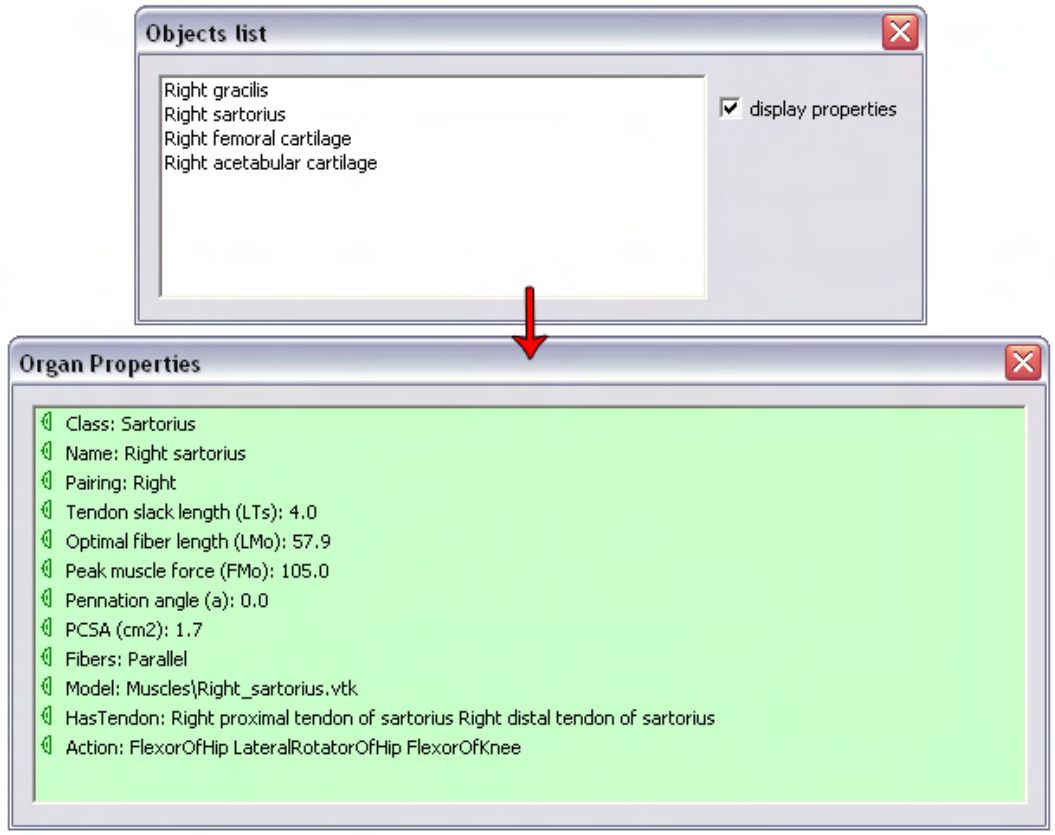

Figure C.7: Objects list and organ properties dialog boxes.

The Dissection mode dialog box

For the muscles, the user can choose between several muscle's dissection modes (e.g., displaying only the muscles which are flexor of the hip or are in the medial compartment of the thigh, etc.).

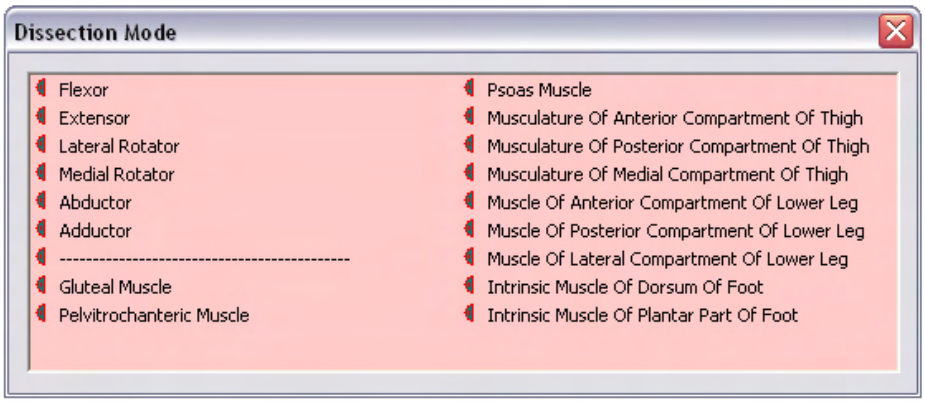

Figure C.8: Dissection mode dialog box.

When the user chooses a muscle's dissection mode, the system removes from the 3D Window the muscles which are not included in the dissection mode. This functionality is driven by the ontology, and is dedicated to improve the navigation through the articulation.

The Models dialog box

The Models dialog box controls the display of 3D models. The user can choose which models to display with certain opacity, appearance (e.g., wireframe, surface view) or visualization type (e.g., medial axis, action lines). He/ she can also change the resolution of the models and display anatomical features (e.g., anatomical landmarks, organ's attachments).

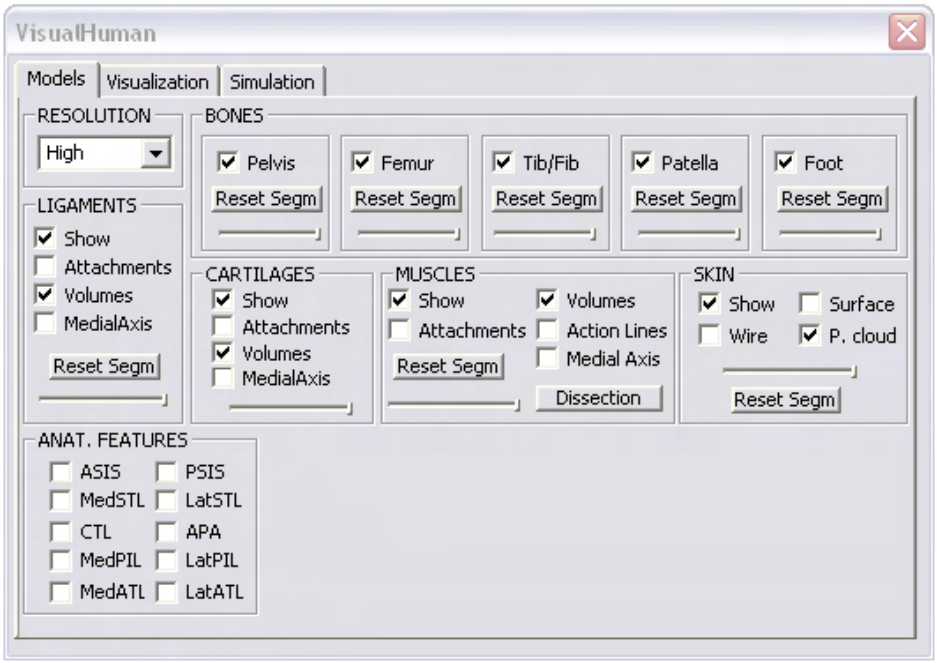

Figure C.9: Models dialog box.

Using the Models dialog box, the user can:

- Change the resolution of the 3D models (High, Medium, Low).
- Show/ hide a 3D model (pelvis, femur, tibia/ fibula, patella, foot, ligaments, cartilages, muscles, and skin).
- Reset the segmentation of a 3D model (pelvis, femur, tibia/ fibula, patella, foot, ligaments, cartilages, muscles, and skin).

- Change the opacity of a 3D model (pelvis, femur, tibia/ fibula, patella, foot, ligaments, cartilages, muscles, and skin).
- Show/ hide the attachments (ligaments, cartilages, and muscles).
- Change the visualization type to volumes, medial axis or action lines (ligaments, cartilages, and muscles). Default is the volumic representation.
- Change the appearance of the skin (surface, wireframe or point cloud). Default is point cloud.
- Show the Dissection mode dialog box.
- Show/ hide an anatomical landmark (ASIS, PSIS, MedSTL, LatSTL, CTL, APA, MedPIL, LatPIL, MedATL, LatATL).

The Visualization dialog box

The Visualization dialog box controls the display of MRI data. It also gives access to the morphological measures (e.g., acetabular version, femoral alpha neck angle), to the interactive visualization tools (e.g., landmarks, annotations, cameras), and to import/ export functions.

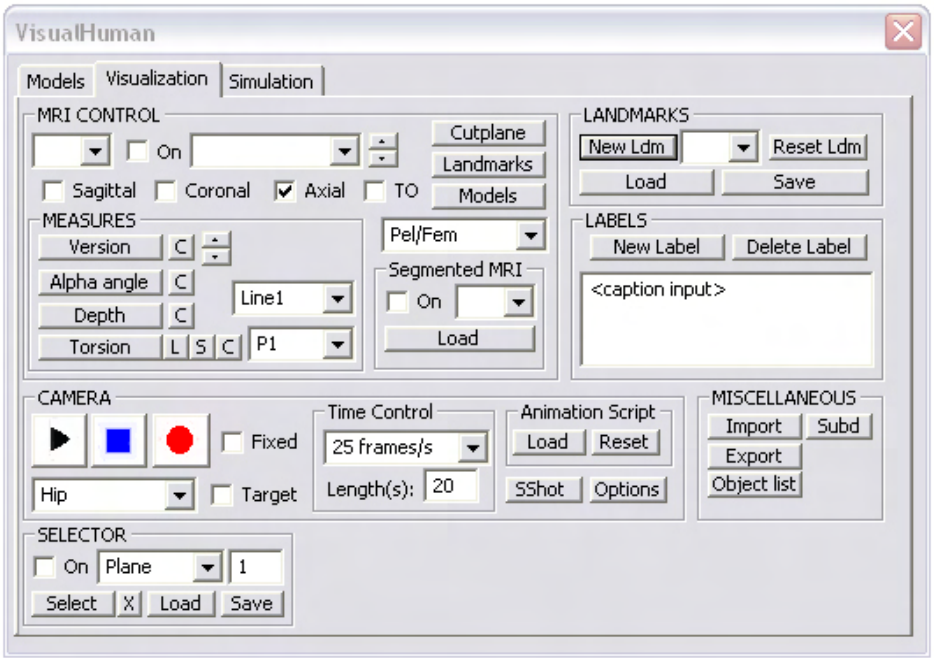

Figure C.10: Visualization dialog box.

Using the Visualization dialog box, the user can:

- With the MRI controllers:
  - Stop/ start the MRI interaction (i.e., moving the "cutplane" in the 3D Window to update the MRI slice in the 2D Window).
  - Change the MRI slice's orientation to sagittal, coronal, axial or transverse oblique (TO).
  - Show/ hide the MRI volume.
  - Change the MRI volume (i.e., several MRI are loaded in the application, but only one volume can be displayed at the same time).
  - Change the acquisition's time (e.g., the images acquired in supine position is one acquisition's time, while the images in split position is another one).
  - Load a segmented MRI.
  - Change the segmented MRI (i.e., several segmented MRI can be loaded in the application, but only one can be displayed at the same time).
  - Show/ hide the segmented MRI.
  - Show/ hide/ change the 3D models overlay (i.e., the contours of the 3D models can be drawn on the MRI slice in the 2D Window).
  - Show/ hide landmarks (i.e., the landmarks can be drawn on the MRI slice in the 2D Window).
- With the morphological measures:
  - Compute the acetabular version.
  - Compute the femoral alpha neck angle.
  - Compute the acetabular depth.
  - Compute the femoral neck torsion.
- With the interactive visualization tools:
  - Interact with predefined 3D cameras, such as: select a camera, start/ stop the camera, update the frame-rate (e.g., 25 or 30 frames/ seconds), update the animation length, load an animation script, make a video, etc.
  - Take a screen shot of the 3D Window.
  - Show the Image options dialog box.
  - Show the Objects list dialog box.

  - Interact with landmarks, such as: create a new landmark, reset all landmarks, load/ save landmarks, etc.
  - Add/ delete a 3D annotation (label).
  - Select 3D model points using a selector (i.e., several selectors are available in the application: a sphere, a plane, etc.).
  - Show/ hide/ change the selector.
  - Reset/ load/ save 3D model points.

- With the import/ export functions:
  - Import a 3D scene in VTK, OBJ or STL.
  - Export a 3D scene in VTK, OBJ or STL.

The Simulation dialog box

The Simulation dialog box controls the simulation of 3D models. The user can simulate the articulations by specifying joint angles or using motion capture or dynamic MRI data. He/ she can also perform the anatomical calibration and compute kinematic parameters (e.g., hip joint center, coordinate systems).

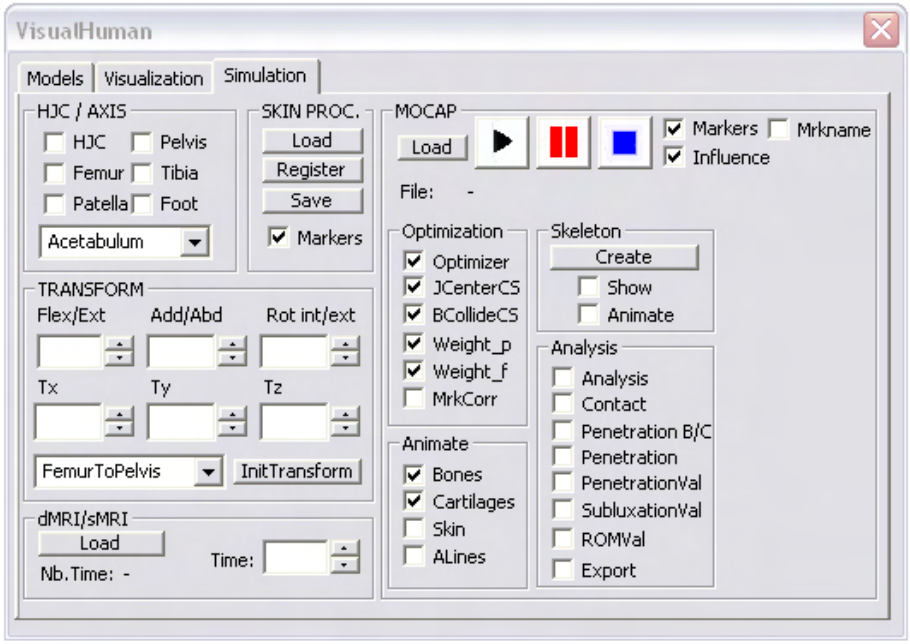

Figure C.11: Simulation dialog box.

Using the Simulation dialog box, the user can:

- With the kinematic controllers:
  - Compute the hip joint's center.
  - Show/ hide a bone's coordinates system (pelvis, femur, tibia, patella, and foot).
  - Compute a bone pose by specifying the joint angles and translations (flex/ ext, abd/ add, rot int/ ext, Tx, Ty, Tz).
- With the anatomical calibration functions:
  - Load the calibration data (body scan model, markers and MRI skin).
  - Make the registration.
  - Save the calibration data (calibrated body scan model and markers).
- With the motion capture controllers:
  - Load the markers.
  - Load the markers trajectories.
  - Show/ hide the markers.
  - Show/ hide the markers names.
  - Play/ pause/ stop the animation.
  - Enable/ disable the animation of 3D models (bones, cartilages and skin).
  - Interact with the virtual skeleton, such as: create the virtual skeleton, show/ hide the virtual skeleton, enable/ disable the animation of the virtual skeleton, etc.
  - Enable/ disable the optimizer.
  - Enable/ disable anatomical constraints.
  - Show/ hide the error made on the markers during motion.
  - Compute/ export the penetration depth.
  - Compute/ export the subluxation amount.
  - Compute/ export the hip joint range of motion.
  - Compute/ export bone poses to 4×4 homogeneous matrices.
- With the dMRI controllers:

– Load a dynamic MRI.

– Increment/ decrement the acquisition's time (i.e, simulate the bones to the next or previous time step).

The Image options dialog box

Before exporting a video or making a screen shot, the user can change the appearance of the 3D Window.

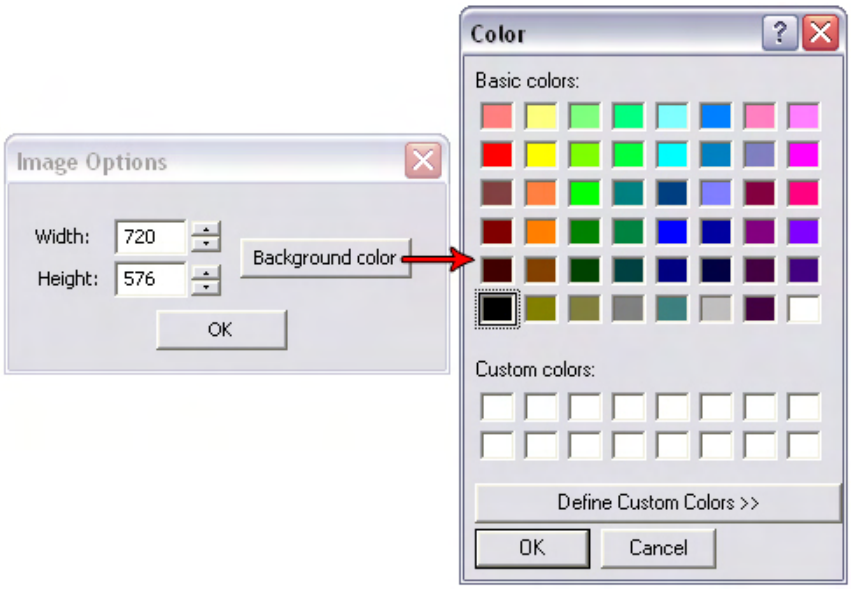

Figure C.12: Image options dialog box.

Using the Image options dialog box, the user can:

- Change the background color.
- Resize the 3D Window.

Appendix D

Publications

C. Charbonnier, F. Kolo-Christophe, V.B. Duthon, N. Magnenat-Thalmann, C. Becker, P. Hoffmeyer, J. Menetrey. *Professional Dancer's Hip: A Motion Capture Study.* Trans Orthop Res Soc, New Orleans, Louisiana, March 2010.

V.B. Duthon, F. Kolo-Christophe, C. Charbonnier, N. Magnenat-Thalmann, S.R. Duc, C.W.A. Pfirrmann, C. Becker, P. Hoffmeyer, J. Menetrey. *Correlation of Clinical and MRI Findings in Professional Dancers' Hip: A New Femoro-acetabular Impingement?* Trans Orthop Res Soc, New Orleans, Louisiana, March 2010.

C. Charbonnier, F. Kolo-Christophe, S.R. Duc, C.W.A. Pfirrmann, J. Menetrey, V.B. Duthon, N. Magnenat-Thalmann, C. Becker, P. Hoffmeyer, *Extreme Motion as a Potential Initiator of Hip Osteoarthritis.* Swiss Med Wkly, EMH, Suppl. 173, 139(23-24):18S, 2009.

V.B. Duthon, J. Menetrey, F. Kolo-Christophe, C. Charbonnier, S.R. Duc, C.W.A. Pfirrmann, N. Magnenat-Thalmann, C. Becker, P. Hoffmeyer, *Professional Dancers' Hip: Correlation of Clinical and MRI Findings.* Swiss Med Wkly, EMH, Suppl. 173, 139(23-24):18S, 2009.

C. Charbonnier, J. Schmid, F. Kolo-Christophe, N. Magnenat-Thalmann, C. Becker, P. Hoffmeyer. *Virtual Hip Joint: from Computer Graphics to Computer-Assisted Diagnosis.* Eurographics 2009 - First Medical Prize, Eurographics Association, Munich, Germany, pp. 1-4, April 2009.

C. Charbonnier, L. Assassi, P. Volino, N. Magnenat-Thalmann. *Motion Study of the Hip Joint in Extreme Postures.* Vis Comput, Springer-Verlag, 25(9):873-882, 2009.

L. Assassi, C. Charbonnier, J. Schmid, P. Volino, N. Magnenat-Thalmann. *From MRI to Anatomical Simulation of the Hip Joint.* Computer Animation and Virtual Worlds Journal, Special Issue on Physiological Human, John Wiley and Sons, 20(1):53-66, 2009.

C. Charbonnier, E. Lyard, N. Magnenat-Thalmann. *Analysis of Extreme Hip Motion in Professional Ballet Dancers.* Proceedings of the 10th International Symposium on 3D Analysis of Human Movement [CD-ROM], Amsterdam, Netherlands, October 2008.

N. Magnenat-Thalmann, C. Charbonnier, J. Schmid. *Multimedia Application to the Simulation of Human Musculoskeletal System: A Visual Lower Limb Model from Multimodal Captured Data.* Proceedings of the IEEE International Workshop on Multimedia Signal Processing, IEEE Publisher, Cairns, Australia, pp. 520-525, October 2008.

C. Charbonnier, B. Gilles, N. Magnenat-Thalmann. *A Semantic-Driven Clinical Examination Platform.* In Surgetica'2007, Computer-Aided Medical Interventions: Tools and Applications, Sauramps Médical, Chambéry, France, pp. 183-189, September 2007.

Glossary

accelerometers	An accelerometer is a device for measuring the total specific external force on the sensor. This is sometimes referred to as the acceleration. Accelerometers may be part of an Inertial Navigation System, used to detect and measure vibrations, or for measuring acceleration due to gravity (inclination). An accelerometer inherently measures its own motion (locomotion), in contrast to a device based on remote sensing, 18
anatomical frames	This is a local frame rigidly associated with a bone segment defined specifically to meet the requirements of intra- and inter-subject repeatability. Their planes normally approximate the frontal, transverse and sagittal anatomical planes. This is achieved by setting a geometric rule that constructs the anatomical frame using selected anatomical landmarks determined in the marker cluster technical frame through the anatomical calibration exercise, 34
anatomical landmarks	Anatomical landmarks are small areas of a bone segment that are used to compute anatomical frames. They are generally located by palpation, 22

cluster technical frame — This is the technical frame used to describe the movement of a segment and is reconstructed using the instantaneous position of at least three non-aligned superficial markers associated with the bony segment and tracked by a photogrammetric system, 34

electromyography — The electromyography is a technique for evaluating and recording physiologic properties of muscles. A thin needle electrode is inserted into the muscle and the electromyograph records the electrical activity in the muscle at rest and while contracting. EMG helps evaluate and diagnose muscle and nerve disorders. Besides invasive approach (needles), surface EMG (sEMG), where electrodes are placed on the skin above muscles, allows superficial analysis for muscle stimulation recording, 17

forces plates — Force plates are commonly used to measure ground reaction forces (6 DOFs). Although there are many types of plates, they all work under the same principle - a force applied to the plate causes an electrical signal proportional to the applied force. To record the forces, the subject should land in the middle part of the plate, 17

gyroscopes — A gyroscope is a device for measuring or maintaining orientation, based on the principles of conservation of angular momentum. The device is a spinning wheel or disk whose axle is free to take any orientation. This orientation changes much less in response to a given external torque than it would without the large angular momentum associated with the gyroscope's high rate of spin. Since external torque is minimized by mounting the device in gimbals, its orientation remains nearly fixed, regardless of any motion of the platform on which it is mounted, 18

photogrammetry — Photogrammetry is the first remote sensing technology ever developed, in which geometric properties about objects are determined from photographic images. Historically, photogrammetry is as old as modern photography itself, and can be dated to mid-nineteenth century. This approach uses methods from many disciplines including optics and projective geometry, 12

stereophotogrammetry — Stereophotogrammetry is the general term applied to the science of measurement from photographs when an overlapping stereopair of photographs is used. In contrast to single photographs, which can only extract 2D information, stereophotogrammetry allows 3D information to be extracted, 12

Bibliography

[AA01] E. Alexander and T.P. Andriacchi. Correcting for deformation in skin-based marker systems. *J Biomech, Elsevier*, 34:355–361, 2001.

[AAT+98] T.P. Andriacchi, E.J. Alexander, M.K. Toney, C. Dyrby, and J. Sum. A point cluster method for in vivo motion analysis: applied to a study of knee kinematics. *J Biomech Eng, ASME*, 120:743–749, 1998.

[ABA03] E.J. Alexander, C. Bregler, and T.P. Andriacchi. Non-rigid modeling of body segments for improved skeletal motion estimation. *Comput Model Eng Sci, Tech Science Press*, 4(3-4):351–364, 2003.

[ACCL92] C. Angeloni, A. Cappozzo, F. Catani, and A. Leardini. Quantification of relative displacement between bones and skin and plate-mounted marker. In *Proc of the VIII Meeting on European Society of Biomechanics*, page 279, Roma, Italy, 1992.

[ACCL93] C. Angeloni, A. Cappello, F. Catani, and A. Leardini. Evaluation of soft tissue artifacts in the in-vivo determination of human knee instantaneous helical axis. In *Proc of the 2nd International Symposium on 3D Analysis of Human Movement*, pages 57–60, Poitiers, France, July 1993.

[BCL+98] M.G. Benedetti, F. Catani, A. Leardini, E. Pignotti, and S. Giannini. Data management in gait analysis for clinical applications. *Clin Biomech, Elsevier*, 13(3):204–215, 1998.

[BGK+96] P. Beylot, P. Gingins, P. Kalra, N. Magnenat-Thalmann, W. Maurel, D. Thalmann, and J. Fasel. 3D interactive topological modeling using visible human dataset. In *Computer Graphics Forum (Proc. Eurographics '96)*, volume 15, pages 33–44. Blackwell Publishing, 1996.

[BH96] S.A. Banks and W.A. Hodge. Accurate measurement of three-dimensional knee replacement kinematics using single-plane fluoroscopy. *IEEE Trans Biomed Eng, IEEE*, 43(6):638–649, 1996.

[Bin03] D. Binningsley. Tear of the acetabular labrum in an elite athlete. *Br J Sports Med, BMJ Publishing Group Ltd*, 37:84–88, 2003.

[BKG05] M. Beck, M. Kalhor, and R. Ganz. Hip morphology influences the pattern of damage to the acetabular cartilage: femoroacetabular impingement as a cause of early osteoarthritis. *J Bone Joint Surg Br, British Editorial Society of Bone & Joint Surgery*, 87:1012–1018, 2005.

[BMH97] S.A. Banks, G.D. Markovich, and W.A. Hodge. In vivo kinematics of cruciate-retaining and -substituting knee arthroplasties. *J Arthroplasty, Elsevier*, 12:297–304, 1997.

[BP98] K.A. Ball and M.R. Pierrynowski. Modeling of the pliant surfaces of the thigh and leg during gait. In *Proc of SPIE*, volume 3254, pages 435–446, San Jose, USA, 1998. Society of Photo-Optical Instrumentation Engineers.

[BPB90] A.L. Bell, D.R. Petersen, and R.A. Brand. A comparison of the accuracy of several hip center location prediction methods. *J Biomech, Elsevier*, 23:617–621, 1990.

[BRL+06] D.L. Benoit, D.K. Ramsey, M. Lamontagne, L. Xu, P. Wretenberg, and P. Renstroem. Effect of skin movement artifact on knee kinematics during gait and cutting motions measured in vivo. *Gait & Posture, Elsevier*, 24(2):152–164, 2006.

[BT95] P.T. Boggs and J.W. Tolle. *Sequential Quadratic Programming*. Acta Numerica, Cambrigde University Press, Cambridge, UK, 1995.

[BZM+05] P.E. Beaulé, E. Zaragoza, K. Motamedi, N. Copelan, and F.J. Dorey. Three-dimensional computed tomography of the hip in the assessment of femoroacetabular impingement. *J Ortho Res, John Wiley and Sons*, 23(6):1286–1292, 2005.

[Cap84] A. Cappozzo. Gait analysis methodology. *Hum Mov Sci, Elsevier*, 3:27–54, 1984.

[CAVMT09] C. Charbonnier, L. Assassi, P. Volino, and N. Magnenat-Thalmann. Motion study of the hip joint in extreme postures. *Vis Comput, Springer-Verlag*, 25(9):873–882, 2009.

[CBF06] S. Chegini, M. Beck, and S.J. Fergusson. Femoro acetabular impingement as a possible initiator of cartilage degeneration. In J. Middleton, N. Shrive, and M. Jones, editors,

7th International Symposium on Computer Methods in Biomechanics and Biomedical Engineering (CMBBE 2006), pages 705–710, Antibes, France, March 2006.

[CBF08] S. Chegini, M. Beck, and S.J. Ferguson. The effects of impingement and dysplasia on stress distributions in the hip joint during sitting and walking: A finite element analysis. *J Ortho Res, John Wiley and Sons*, 27(2):195–201, 2008.

[CCC06] A. Cereatti, U. Della Croce, and A. Cappozzo. Reconstruction of skeletal movement using skin markers: comparative assessment of bone pose estimators. *Journal of NeuroEngineering and Rehabilitation [Online], BioMed Central*, 3(7), 2006.

[CCCL95] A. Cappozzo, F. Catani, U. Della Croce, and A. Leardini. Position and orientation of bones during movement: anatomical frame definition and determination. *Clin Biomech, Elsevier*, 10:171–178, 1995.

[CCCL97] A. Cappello, A. Cappozzo, U. Della Croce, and A. Leardini. Bone position and orientation reconstruction using external markers. *Three-Dimensional Analysis of Human Locomotion*, Chichester, UK:Wiley:147–171, 1997.

[CCK99] U. Della Croce, A. Cappozzo, and D.C. Kerrigan. Pelvis and lower limb anatomical landmark calibration precision and its propagation to bone geometry and joint angles. *Med Biol Eng Comp, Springer-Verlag*, 37:155–161, 1999.

[CCL93] A. Cappozzo, F. Catani, and A. Leardini. Skin movement artifacts in human movement photogrammetry. In *Proc of the XIVth Congress of the International Society of Biomechanics*, volume I, pages 238–239, 1993.

[CCL+96] A. Cappozzo, F. Catani, A. Leardini, M.G. Benedetti, and U. Della Croce. Position and orientation in space of bones during movement: experimental artefacts. *Clin Biomech, Elsevier*, 11(2):90–100, 1996.

[CCP+97] A. Cappello, A. Cappozzo, P.F. La Palombara, L. Lucchetti, and A. Leardini. Multiple anatomical landmark calibration for optimal bone pose estimation. *Hum Mov Sci, Elsevier*, 16(2-3):259–274, 1997.

[CDC+09] A. Cereatti, M. Donati, V. Camomilla, F. Margheritini, and A. Cappozzo. Hip joint centre location: An ex vivo study. *J Biomech, Elsevier*, 42(7):818–823, 2009.

[CFD95] L. Chèze, B.J. Fregly, and J. Dimnet. A solidification procedure to facilitate kinematic analyses based on video system data. *J Biomech, Elsevier*, 28:879–884, 1995.

[CGMT07] C. Charbonnier, B. Gilles, and N. Magnenat-Thalmann. A semantic-driven clinical examination platform. In *Surgetica'2007, Computer-Aided Medical Interventions: Tools and Applications, Sauramps Médical*, pages 183–189, Chambery, France, September 2007.

[CKCD+09] C. Charbonnier, F. Kolo-Christophe, S.R. Duc, C.W.A. Pfirrmann, J. Menetrey, V.B. Duthon, N. Magnenat-Thalmann, C. Becker, and P. Hoffmeyer. Extreme motion as a potential initiator of hip osteoarthritis. *Swiss Med Wkly, EMH*, Suppl. 173, 139(23-24):18S, 2009.

[CKCD+10a] C. Charbonnier, F. Kolo-Christophe, V.B. Duthon, N. Magnenat-Thalmann, C. Becker, P. Hoffmeyer, and J. Menetrey. Assessment of congruence and impingement of the hip joint in professional ballet dancers. *Am J Sports Med, Sage*, Submitted, 2010.

[CKCD+10b] C. Charbonnier, F. Kolo-Christophe, V.B. Duthon, N. Magnenat-Thalmann, C. Becker, P. Hoffmeyer, and J. Menetrey. Professional dancer's hip: A motion capture study. In *Trans Orthop Res Soc*, New Orleans, Louisiana, 2010.

[CKH+09] J.C. Clohisy, E.R. Knaus, D.M. Hunt, J.M. Lesher, M. Harris-Hayes, and H. Prather. Clinical presentation of patients with symptomatic anterior hip impingement. *Clin Orthop Rel Res, Springer-Verlag*, 467:638–644, 2009.

[CLCC05] U. Della Croce, A. Leardini, L. Chiari, and A. Cappozzo. Human movement analysis using stereophotogrammetry Part 4: Assessment of anatomical landmark misplacement and its effects on joint kinematics. *Gait & Posture, Elsevier*, 21:226–237, 2005.

[CLMT08] C. Charbonnier, E. Lyard, and N. Magnenat-Thalmann. Analysis of extreme hip motion in professional ballet dancers. In *Proc of the 10th International Symposium on 3D Analysis of Human Movement [CD-ROM]*, Amsterdam, Netherlands, October 2008.

[CMA06] S. Corazza, L. Muendermann, and T.P. Andriacchi. Markerless motion capture methods for the estimation of human body kinematics. In *Proc of the 9th International Symposium on 3D Analysis of Human Movement*, Valenciennes, France, June 2006.

[CPF03] P. Cerveri, A. Pedotti, and G. Ferrigno. Robust recovery of human motion from video using kalman filters and virtual humans. *Hum Mov Sci, Elsevier*, 22(3):377–404, 2003.

[CPF05] P. Cerveri, A. Pedotti, and G. Ferrigno. Kinematical models to reduce the effect of skin artifacts on marker-based human motion estimation. *J Biomech, Elsevier*, 38:2228–2236, 2005.

[Cro06] U. Della Croce. Soft tissue artifacts in movement analysis. In *Proc of the 9th International Symposium on 3D Analysis of Human Movement*, Valenciennes, France, June 2006.

[CSFL05] A. Cappello, R. Stagni, S. Fantozzi, and A. Leardini. Soft tissue artifact compensation in knee kinematics by double anatomical landmark calibration: Performance of a novel method during selected motor tasks. *IEEE Trans Biomed Eng, IEEE*, 52(2):992–998, 2005.

[CSKC+09] C. Charbonnier, J. Schmid, F. Kolo-Christophe, N. Magnenat-Thalmann, C. Becker, and P. Hoffmeyer. Virtual hip joint: from computer graphics to computer-assisted diagnosis. In *Eurographics 2009 - First Medical Prize*, pages 1–4, Munich, Germany, April 2009. Eurographics Association.

[CTR04] I.W. Charlton, P. Tate, and L. Roren. Repeatability of an optimised lower body model. *Gait & Posture, Elsevier*, 20:213–221, 2004.

[D'A06] Nicola D'Apuzzo. State of the art of the methods for static 3D scanning of partial or full human body. In *3D Modelling*, Paris, France, June 2006.

[DBD+04] A. Duhamel, J.L. Bourriez, P. Devos, P. Krystkowiak, A. Deste, P. Derambure, and L. Defebvre. Statistical tools for clinical gait analysis. *Gait & Posture, Elsevier*, 20:204–212, 2004.

[DCVC07] M. Donati, V. Camomilla, G. Vannozzi, and A. Cappozzo. Enhanced anatomical calibration in human movement analysis. *Gait & Posture, Elsevier*, 26:179–185, 2007.

[DCVC08] M. Donati, V. Camomilla, G. Vannozzi, and A. Cappozzo. Anatomical frame identification and reconstruction for repeatable lower limb joint kinematics estimates. *J Biomech, Elsevier*, 41(10):2219–2226, 2008.

[DHW+04] K. Denis, T. Huysmans, T. De Wilde, C. Forausberger, W. Rapp, B. Haex, J. Vander Sloten, R. Van Audekercke, G. Van der Perre, K.R. Heitmann, and H. Diers. A 4D-optical measuring system for the dynamic acquisition of anatomical structures. In *MICCAI 2004, LNCS*, volume 2, pages 259–266. Springer-Verlag, 2004.

[DJA05] H. Dejnabadi, B. M. Jolles, and K. Aminian. A new approach to accurate measurement of uniaxial joint angles based on a combination of accelerometers and gyroscopes. *IEEE Trans Biomed Eng, IEEE*, 52(8):1478–1484, 2005.

[DJC+06] H. Dejnabadi, B. M. Jolles, E. Casanova, P. Fua, and K. Aminian. Estimation and visualization of sagittal kinematics of lower limbs orientation using body-fixed sensors. *IEEE Trans Biomed Eng, IEEE*, 53(7):1385–1393, 2006.

[DKCC+10] V.B. Duthon, F. Kolo-Christophe, C. Charbonnier, N. Magnenat-Thalmann, S.R. Duc, C.W.A. Pfirrmann, C. Becker, P. Hoffmeyer, and J. Menetrey. Correlation of clinical and MRI findings in professional dancers' hip: A new femoro-acetabular impingement? In *Trans Orthop Res Soc*, New Orleans, Louisiana, 2010.

[DMKC+09] V.B. Duthon, J. Menetrey, F. Kolo-Christophe, C. Charbonnier, S.R. Duc, C.W.A. Pfirrmann, N. Magnenat-Thalmann, C. Becker, and P. Hoffmeyer. Professional dancers' hip: Correlation of clinical and MRI findings. *Swiss Med Wkly, EMH*, Suppl. 173, 139(23-24):18S, 2009.

[DOTG91] R.B. Davis, S. Ounpuu, D. Tyburski, and J.R. Gage. A gait analysis data-collection and reduction technique. *Hum Mov Sci, Elsevier*, 10:575–587, 1991.

[ES86] K.B. Eberhardt and G. Selvik. Some aspects of knee joint kinematics in rheumatoid arthritis as studied with rontgen stereophotogrammetry. *Clin Rheumatol, Springer-Verlag*, 5:201–209, 1986.

[FGL88] K.S. Fu, R.C. Gonzalez, and C.S.G Lee. *Robotics: control, sensing, vision and intelligence*. McGraw-Hill, New York, 1988.

[FJAA08] J. Favre, B.M. Jolles, R. Aissaoui, and K. Aminian. Ambulatory measurement of 3d knee joint angle. *J Biomech, Elsevier*, 41:1029–1035, 2008.

[FLMM97] J. Fuller, L.J. Liu, M.C. Murphy, and R.W. Mann. A comparison of lower extremity skeletal kinematics measured using skin- and pin-mounted markers. *Hum Mov Sci, Elsevier*, 16:219–242, 1997.

[FRB05] B. Fregly, H. Rahman, and S.A. Banks. Accurate measurement of three dimensional natural knee kinematics using single-plane fluoroscopy. *J Biomech Eng, ASME*, 127(4):692–699, 2005.

[FSC+02] S. Fantozzi, R. Stagni, A. Cappello, M. Bicchierini, A. Leardini, and F. Catani. Skin motion artefact characterization from 3d fluoroscopy and stereophotogrammetry. In *IV World Congress of Biomechanics*, Calgary, Canada, August 2002.

[GFB+04] A. Gupta, B. Fernihough, G. Bailey, P. Bombeck, A. Clarke, and D. Hopper. An evaluation of differences in hip external rotation strength and range of motion between female dancers and non-dancers. *Br J Sports Med, BMJ Publishing Group Ltd*, 38(6):778–783, 2004.

[GH09] M.M. Groh and J. Herrera. A comprehensive review of hip labral tears. *Curr Rev Musculoskelet Med, Springer-Verlag*, 2:105–117, 2009.

[Gil07] Benjamin Gilles. *Anatomical and Kinematical Modelling of the Musculoskeletal System from MRI.* PhD thesis, Université de Genève, 2007.

[GJGMSM04] S. Glyn-Jones, H.S. Gill, P. McLardy-Smith, and D.W. Murray. Roentgen stereophotogrammetric analysis of the birmingham hip resurfacing arthroplasty: A two-year study. *J Bone Joint Surg, The Journal of Bone and Joint Surgery, Inc.*, 86-B:172–176, 2004.

[GKCMT+09] B. Gilles, F. Kolo-Christophe, N. Magnenat-Thalmann, C. Becker, S. Duc, J. Menetrey, and P. Hoffmeyer. MRI-based assessment of hip joint translations. *J Biomech, Elsevier*, 42(9):1201–1205, 2009.

[GKM+07] E. Garling, B. Kaptein, B. Mertens, W. Barendregt, H. Veeger, R. Nelissen, and E. Valstar. Soft-tissue artefact assessment during step-up using fluoroscopy and skin-mounted markers. *J Biomech, Elsevier*, 40:18–24, 2007.

[GLM96] S. Gottschalk, M. Lin, and D. Manocha. Obbtree: A hierarchical structure for rapid interference detection. In *SIGGRAPH'96*, pages 171–180. Addison Wesley, 1996.

[GMMT06] B. Gilles, L. Moccozet, and N. Magnenat-Thalmann. Anatomical modelling of the musculoskeletal system from MRI. In R. Larsen, M. Nielsen, and J. Sporring, editors, *MICCAI 2006, LNCS*, volume 4190, pages 289–296. Springer-Verlag, October 2006.

[GPB+03] R. Ganz, J. Parvizi, M. Beck, M. Leunig, H. Notzli, and K.A. Siebenrock. Femoroacetabular impingement: a cause for osteoarthritis of the hip. *Clin Orthop Rel Res, Springer-Verlag*, 417:112–120, 2003.

[GPMTV04] B. Gilles, R. Perrin, N. Magnenat-Thalmann, and J-P. Vallée. Bone motion analysis from dynamic MRI: acquisition and tracking. In *MICCAI 2004, LNCS*, volume 2, pages 942–949. Springer-Verlag, September 2004.

[GPMTV05] B. Gilles, R. Perrin, N. Magnenat-Thalmann, and J-P. Vallée. Bones motion analysis from dynamic MRI: acquisition and tracking. *Acad Radiol, Elsevier*, 12:2385–2392, Oct. 2005.

[GS83] E.S. Grood and W.J. Suntay. A joint coordinate system for the clinical description of three-dimensional motions: application to the knee. *J Biomech Eng, ASME*, 105:136–144, 1983.

[HLL99] K. Halvorsen, M. Lesser, and A. Lundberg. A new method for estimating the axis of rotation and the center of rotation. *J Biomech, Elsevier*, 2(11):1221–1227, 1999.

[Hor87] B.K.P. Horn. Closed-form solution of absolute orientation using unit quaternions. *J Opt Soc Am, Optical Society of America*, 4(4):629–642, 1987.

[HOS+97] J.P. Holden, J.H. Orsini, K.L. Siegel, T.M. Kepple, L.H. Gerber, and S.J. Stanhope. Surface movement errors in shank kinematics and knee kinetics during gait. *Gait & Posture, Elsevier*, 5:217–227, 1997.

[HYC04] J. Houck, H.J Yack, and T. Cuddeford. Validity and comparisons of tibiofemoral orientations and displacement using a femoral tracking device during early to mid stance of walking. *Gait & Posture, Elsevier*, 19:76–84, 2004.

[InL+01] K. Ito, M.A. Minka 2nd, M. Leunig, S. Werlen, and R. Ganz. Femoroacetabular impingement and the cam-effect: a MRI based quantitative anatomical study of the femoral headneck offset. *J Bone Joint Surg Br, British Editorial Society of Bone & Joint Surgery*, 83:171–176, 2001.

[Jol86] T. Jollife. *Principal Components Analysis*. Springer-Verlag, New York, 1986.

[JSH+02] S. Van Sint Jan, V. Sholukha, I. Hilal, A. Leardini, P. Salvia, P. Poulet, and al. Advanced modelling and simulation of lower limb motion using medical imaging, electrogoniometry and gait analysis data. In *Proc of the 7th International Symposium on 3D Analysis of Human Movement*, Newcastle, England, July 2002.

[Kan05] MyungJin Kang. *Individualized generation of motions of hip joint*. PhD thesis, Université de Genève, 2005.

[Kap96] I.A. Kapandji. *Physiologie articulaire, schémas commentés de mécanique humaine.* Fascicule II - Membre inférieur. Maloine, Paris, 5e edition, 1996.

[KASS94] T.M. Kepple, A.S. Arnold, S.J. Stanhope, and K.L. Siegel. Assessment of a method to estimate muscle attachments from surface landmarks: a 3D computer graphics approach. *J Biomech, Elsevier*, 27:365–371, 1994.

[KBG+95] P. Kalra, P. Beylot, P. Gingins, N. Magnenat-Thalmann, P. Volino, P. Hoffmeyer, J. Fasel, and F. Terrier. Topological modeling of human anatomy using medical data. In *Comput Anim*, pages 172–180, 1995.

[KL94] D. Karlsson and A. Lundberg. Accuracy estimation of kinematic data derived from bone anchored external markers. In *Proc of the 3rd International Symposium on 3D Analysis of Human Movement*, pages 27–30, Stockholm, Sweden, July 1994.

[KLL83] T.R Kane, P.W. Likins, and D.A. Levinson. *Spacecraft dynamics.* McGraw-Hill, New York, 1983.

[KRN+97] K. Khan, P. Roberts, C. Nattrass, K. Bennell, S. Mayers, S. Way, J. Brown, J. McMeeken, and J. Wark. Hip and ankle range of motion in elite classical ballet dancers and controls. *Clin J Sport Med, Lippincott Williams & Wilkins*, 7(3):174–179, 1997.

[KSMMT03] M. Kang, H. Sadri, L. Moccozet, and N. Magnenat-Thalmann. Hip joint modeling for the control of the joint center and the range of motions. In *IFAC Symposium on modelling and control in biomedical systems*, pages 23–27. Elsevier, August 2003.

[KSMT05] M. Kang, H. Sadri, and N. Magnenat-Thalmann. Computer-assisted pre-operative planning for hip joint-preserving surgery. In *5th Annual Meeting of the International Society for Computer Assisted Orthopaedic Surgery*, pages 212–214. Pro Business, June 2005.

[KT99] D. Karlsson and R. Tranberg. On skin movement artifact-resonant frequencies of skin markers attached to the leg. *Hum Mov Sci, Elsevier*, 18:627–635, 1999.

[Laf84] M.A. Lafortune. *The use of intra-cortical pins to measure the motion of the knee joint during walking.* PhD thesis, The Pennsylvania State University, 1984.

[LBC+99] A. Leardini, M.G. Benedetti, F. Catani, L. Simoncini, and S. Giannini Clin Biomech. An anatomically based protocol for the description of foot segment kinematics during gait. *Clin Biomech, Elsevier*, 14(8):528–536, 1999.

[LCC+99] A. Leardini, A. Cappozzo, F. Catani, S. Toksvig-Larsen, A. Petitto, and V. Sforza et al. Validation of a functional method for the estimation of the hip joint centre location. *J Biomech, Elsevier*, 32(1):99–103, 1999.

[LCCC98] L. Lucchetti, A. Cappozzo, A. Cappello, and U. Della Croce. Skin movement artefact assessment and compensation in the estimation of knee joint kinematics. *J Biomech, Elsevier*, 31(11):977–984, 1998.

[LCCC05] A. Leardini, L. Chiari, U. Della Croce, and A. Cappozzo. Human movement analysis using stereophotogrammetry Part 3: Soft tissue artifact assessment and compensation. *Gait & Posture, Elsevier*, 21:212–225, 2005.

[LCS+94] M.A. Lafortune, P.R. Cavanagh, H.J. Sommer, H.J. Ill, and A. Kalenak. Foot inversion-eversion and knee kinematics during walking. *J Ortho Res, John Wiley and Sons*, 12:412–420, 1994.

[LCSK92] M.A. Lafortune, P.R. Cavanagh, H.J. Sommer, and A. Kalenak. Three dimensional kinematics of the human knee during walking. *J Biomech, Elsevier*, 25(4):347–357, 1992.

[LeG09] M. Leunig, P.E. Beaulé, and R. Ganz. The concept of femoroacetabular impingement. *Clin Orthop Rel Res, Springer-Verlag*, 467:616–622, 2009.

[LIB48] A.S. Levens, V.T. Inman, and J.A. Blosser. Transverse rotation of the segments of the lower extremity in locomotion. *J Bone Joint Surg, The Journal of Bone and Joint Surgery, Inc.*, 30A:859–872, 1948.

[LL91] M.A. Lafortune and M.J. Lake. Errors in 3D analysis of human movement. In *Proc of the 1st International Symposium on 3D Analysis of Human Movement*, pages 55–56, Montréal, Canada, July 1991.

[LNL+08] P. Lundgren, C. Nester, A. Liu, A. Arndt, R. Jones, A. Stacoff, P. Wolf, and A. Lundberg. Invasive in vivo measurement of rear-, mid- and forefoot motion during walking. *Gait & Posture, Elsevier*, 28:93–100, 2008.

[LO99] T.W. Lu and J.J. O'Connor. Bone position estimation from skin marker co-ordinates using global optimisation with joint constraints. *J Biomech, Elsevier*, 32:129–134, 1999.

[LO00] T.W. Lu and J.J. OConnor. Three-dimensional computer graphics-based modelling and mechanical analysis of the human locomotor system. In *Proc of the 6th International Symposium on 3D Analysis of Human Movement*, Cape Town, South Africa, May 2000.

[LPB+04] M. Lavigne, J. Parvizi, M. Beck, K.A. Siebenrock, R. Ganz, and M. Leunig. Anterior femoroacetabular impingement: Part I: Techniques of joint preserving surgery. *Clin Orthop Rel Res, Springer-Verlag*, 418:61–66, 2004.

[LS06] C.R. Lewis and S.A. Sahrmann. Acetabular labral tears. *Phys Ther, American Physical Therapy Association*, 86:110–121, 2006.

[LT01] C.T. Lawrence and A.L. Tits. A computationally efficient feasible sequential quadratic programming algorithm. *SIAM J Optim, Society for Industrial and Applied Mathematics*, 11(4):1092–1118, 2001.

[LTK+08] T.W. Lu, T.Y. Tsai, M.Y. Kuo, H.C. Hsu, and H.L. Chen. In vivo three-dimensional kinematics of the normal knee during active extension under unloaded and loaded conditions using single-plane fluoroscopy. *Med Eng & Phys, Elsevier*, 30(8):1004–1012, 2008.

[MA94] B.A. Maslen and T.R. Ackland. Radiographic study of skin displacement errors in the foot and ankle during standing. *Clin Biomech, Elsevier*, 9:221–226, 1994.

[Mas01] J.B. Mason. Acetabular labral tears in the athlete. *Clin J Sport Med, Lippincott Williams & Wilkins*, 20:779–790, 2001.

[MB06] F. Moerl and R. Blickhan. Three-dimensional relation of skin markers to lumbar vertebrae of healthy subjects in different postures measured by open MRI. *Eur Spine J, Springer-Verlag*, 15:742–751, 2006.

[MCA06] L. Muendermann, S. Corazza, and T.P. Andriacchi. The evolution of methods for the capture of human movement leading to markerless motion capture for biomedical applications. *Journal of NeuroEngineering and Rehabilitation [Online], BioMed Central*, 3, 2006.

[Men97] F. Menschik. The hip joint as a conchoid shape. *J Biomech, Elsevier*, 30:971–973, 1997.

[Men00] A. Menache. *Understanding Motion Capture for Computer Animation and Video Games*. Academic Press, San Diego, 2000.

[MG01] G. Moeslund and E. Granum. A survey of computer vision-based human motion capture. *Comput Vis Image Understand, Elsevier*, 81:231–268, 2001.

[ML00] N.J. Manek and N.E. Lane. Osteoarthritis: Current concepts in diagnosis and management. *Am Fam Physician, American Academy of Family Physicians*, 61(6):1795–1804, 2000.

[MMR+02] K. Manal, I. McClay, J. Richards, B. Galinat, and S. Stanhope. Knee moment profiles during walking: errors due to soft tissue movement of the shank and the influence of the reference coordinate system. *Gait & Posture, Elsevier*, 15:10–17, 2002.

[MMS+00] K. Manal, I. McClay, S. Stanhope, J. Richards, and B. Galinat. Comparison of surface mounted markers and attachment methods in estimating tibial rotations during walking: an in vivo study. *Gait & Posture, Elsevier*, 11:38–45, 2000.

[MNA+03] J.C. McCarthy, P.C. Noble, F.V. Aluisio, M. Schuck, J. Wright, and J.A. Lee. Anatomy, pathologic features, and treatment of acetabular labral tears. *Clin Orthop Rel Res, Springer-Verlag*, 406:38–47, 2003.

[MNS+01] J. McCarthy, P. Noble, M. Schuck, J. Wright, and J. Lee. The otto E. Aufranc Award: the role of labral lesions to development of early degenerative hip disease. *Clin Orthop Rel Res, Springer-Verlag*, 393:25–37, 2001.

[Mor99] D. Morrisson. *Multivariate statistical methods*. McGraw-Hill, New York, 1999.

[MSBT05] A. Maciel, S. Sarni, R. Boulic, and D. Thalmann. Stress distribution visualization on pre- and post-operative virtual hip joint. In *Proc Comp Assist Orthop Surg (CAOS'05)*, pages 298–301, 2005.

[MTCS08] N. Magnenat-Thalmann, C. Charbonnier, and J. Schmid. Multimedia application to the simulation of human musculoskeletal system: A visual lower limb model from multimodal captured data. In *Proc of the IEEE International Workshop on Multimedia Signal Processing*, pages 520–525, Cairns, Australia, October 2008. IEEE Publisher.

[MTLT88] N. Magnenat-Thalmann, R. Laperriere, and D. Thalmann. Joint-dependent local deformations for hand animation and object grasping. In *Proc. Graphics Interface*, pages 26–33, 1988.

[MWMTT98] W. Maurel, Y. Wu, N. Magnenat-Thalmann, and D. Thalmann. *Biomechanical Models for Soft Tissue Simulation*. Basic Research Series. Springer-Verlag, New York, 1998.

[Net06] Frank H. Netter. *Atlas of Human Anatomy.* W.B. Saunders Company, 4th edition, 2006.

[NJL+07] C. Nester, R.K. Jones, A. Liu, D. Howard, A. Lundberg, A. Arndt, P. Lundgren, A. Stacoff, and P. Wolf. Foot kinematics during walking measured using bone and surface mounted markers. *J Biomech, Elsevier*, 40:3412–3423, 2007.

[NV00] N. Santori N and R.N. Villar. Acetabular labral tears: result of arthroscopic partial limbectomy. *Arthroscopy, Elsevier*, 16:11–15, 2000.

[NWS+02] H.P. Nötzli, T.F. Wyss, C.H. Stöcklin, M.R. Schmid MR, K. Treiber, and J. Hodler. The contour of the femoral headneck-junction as a predictor for the risk of anterior impingement. *J Bone Joint Surg Br, British Editorial Society of Bone & Joint Surgery*, 84:556–560, 2002.

[PHS+02] C.W.A. Pfirrmann, M. Huser, G. Szekeli, J. Hodler, and C. Gerber. Evaluation of complex joint motion with computer-based analysis of fluoroscopic sequences. *Investig Radiol, Lippincott Williams & Wilkins*, 37(2):73–76, 2002.

[PMD+06] C. W. A. Pfirrmann, B. Mengiardi, C. Dora, F. Kalberer, M. Zanetti, and J. Hodler. Cam and pincer femoroacetabular impingement: Characteristic MR arthrographic findings in 50 patients. *J Radiol, Masson Editeur*, 240(3):778–785, 2006.

[RBF+02] M. Rabuffetti, G. Baroni, M. Ferrarin, G. Ferrigno, and A. Pedotti. Selfmarking of anatomical landmarks for on-orbit experimental motion analysis compared to expert direct-marking. *Hum Mov Sci, Elsevier*, 21:439–455, 2002.

[RLK99] D. Reynolds, J. Lucas, and K. Klaue. Retroversion of the acetabulum. a cause of hip pain. *J Bone Joint Surg, The Journal of Bone and Joint Surgery, Inc.*, 81(2):281–288, 1999.

[RT02] L. Roren and P. Tate. A new lower body model using global optimisation techniques. *Gait & Posture, Elsevier*, 16(Suppl.1):14–15, 2002.

[RvdBL+97a] C. Reinschmidt, A.J. van den Bogert, A. Lundberg, B.M. Nigg, and N. Murphy. Effect of skin movement on the analysis of skeletal knee joint motion during running. *J Biomech, Elsevier*, 30(7):729–732, 1997.

[RvdBL+97b] C. Reinschmidt, A.J. van den Bogert, A. Lundberg, B.M. Nigg, N. Murphy, A. Stacoff, and A. Stano. Tibiofemoral and tibiocalcaneal motion during walking: external vs. skeletal markers. *Gait & Posture, Elsevier*, 6(2):98–109, 1997.

[SB93] I. Söderkvist and P.A. Wedin J Biomech. Determining the movements of the skeleton using well-configured markers. *J Biomech, Elsevier*, 12:1473–1477, 1993.

[SBL08] A.G. Schache, R. Baker, and L.W. Lamoreux. Influence of thigh cluster configuration on the estimation of hip axial rotation. *Gait & Posture, Elsevier*, 27:60–69, 2008.

[SD06] R.A. Siston and S.L. Delp. Evaluation of a new algorithm to determine the hip joint center. *J Biomech, Elsevier*, 39:125–130, 2006.

[SdGLK96] M. Sati, J.A. de Guise, S. Larouche, and G. Drouin Knee. Quantitative assessment of skin-bone movement at the knee. *The Knee, Elsevier*, 3(3):121–138, 1996.

[SdQD+07] A. Stacoff, I. Kramers de Quervain, M. Dettwyler, P. Wolf, R. List, T. Ukelo, and E. Stuessi. Biomechanical effects of foot orthoses during walking. *The Foot, Elsevier*, 17:143–153, 2007.

[SE03] P.J. Schneider and D.H. Eberly. *Geometric Tools for Computer Graphics*. The Morgan Kaufmann Series in Computer Graphics and Geometric Modeling, 2003.

[Sel89] G. Selvik. Roentgen stereophotogrammetry. A method for the study of the kinematics of the skeletal system. *Acta Orthop Scand, Taylor & Francis*, 232:1–51, 1989.

[SFC+02] R. Stagni, S. Fantozzi, A. Cappello, F. Brigliadori, and A. Leardini. Effect of skin motion artefacts on knee joint kinematics. In *IV World Congress of Biomechanics*, Calgary, Canada, August 2002.

[SFC06] R. Stagni, S. Fantozzi, and A. Cappello. Propagation of anatomical landmark misplacement to knee kinematics: Performance of single and double calibration. *Gait & Posture, Elsevier*, 24:137–141, 2006.

[SFC08] R. Stagni, S. Fantozzi, and A. Cappello. Double calibration vs. global optimisation: Performance and effectiveness for clinical application. *Gait & Posture, Elsevier*, 29(1):119–122, 2008.

[SFCL05] R. Stagni, S. Fantozzi, A. Cappello, and A. Leardini. Quantification of soft tissue artifact in motion analysis by combining 3D fluoroscopy and stereophotogrammetry: a study on two subjects. *Clin Biomech, Elsevier*, 20:320–329, 2005.

[SHP+06] N. Steinberg, I. Hershkovitz, S. Peleg, G. Dar, Y. Masharawi, M. Heim, and I. Siev-Ner. Range of joint movement in female dancers and nondancers aged 8 to 16 years: anatomical and clinical implications. *Am J Sports Med, Sage*, 34(5):814–823, 2006.

[SJC+09] P. Salvia, S. Van Sint Jan, A. Crouan, L. Vanderkerken, F. Moiseev, V. Sholukha, C. Mahieu, O. Snoeck, and M. Rooze. Precision of shoulder anatomical landmark calibration by two approaches: A CAST-like protocol and a new anatomical palpator method. *Gait & Posture, Elsevier*, 29(4):587–591, 2009.

[SMBT05] S. Sarni, A. Maciel, R. Boulic, and D. Thalmann. Spreadsheet Framework for Visual Exploration of Biomedical Datasets. In *IEEE CBMS 2005*, pages 159–164. IEEE Publisher, 2005.

[SMC+06] M. Sangeux, F. Marin, F. Charleux, L. Duerselen, and M.C. Ho Ba Tho. Quantification of the 3D relative movement of external marker sets vs. bones based on magnetic resonance imaging. *Clin Biomech, Elsevier*, 21:984–991, 2006.

[SMT03] H. Seo and N. Magnenat-Thalmann. An automatic modeling of human bodies from sizing parameters. In *ACM SIGGRAPH 2003 Symp on Interact 3D Graph*, pages 19–26, April 2003.

[SMT08] J. Schmid and N. Magnenat-Thalmann. MRI bone segmentation using deformable models and shape priors. In D. Metaxas, L. Axel, G. Szekely, and G. Fichtinger, editors, *MICCAI 2008, Part I. LNCS*, volume 5241, pages 119–126. Springer-Verlag, September 2008.

[SSG03] K.A. Siebenrock, R. Schniger, and R. Ganz. Anterior femoro-acetabular impingement due to acetabular retroversion and its treatment by periacetabular osteotomy. *J Bone Joint Surg Am, The Journal of Bone and Joint Surgery, Inc.*, 85:278–286, 2003.

[TA75] G.J. Torotra and N.P. Anagnostakos. *Principles of Anatomy and Physiology*. Canfield Press, New York, 1975.

[TA02] S. Tashman and W. Andrest. Skin motion artifacts at the knee during impact movements. In *19th Annual meeting of the American Society of Biomechanics Stanford CA*. ASB Press, 2002.

[TED+05] W.R. Taylor, R.M. Ehrig, G.N. Duda, H. Schell, P. Seebeck, and M.O. Heller. On the influence of soft tissue coverage in the determination of bone kinematics using skin markers. *J Ortho Res, John Wiley and Sons*, 23:726–734, 2005.

[TGB+08] M. Tannast, D. Goricki, M. Beck, S. B. Murphy, and K. A. Siebenrock. Hip damage occurs at the zone of femoroacetabular impingement. *Clin Orthop Rel Res, Springer-Verlag*, 466:273–280, 2008.

[TK98] R. Tranberg and D. Karlsson. The relative skin movement of the foot: a 2D roentgen photogrammetry study. *Clin Biomech, Elsevier*, 13(1):71–76, 1998.

[vdBRL08] A.J. van den Bogert, C. Reinschmidt, and A. Lundberg. Helical axes of skeletal knee joint motion during running. *J Biomech, Elsevier*, 41:1632–1638, 2008.

[VNRR02] E.R Valstar, R.G.H.H Nelissen, J. H.C. Reiber, and P.M. Rozing. The use of roentgen stereophotogrammetry to study micromotion of orthopaedic implants. *ISPRS Journal of Photogrammetry and Remote Sensing, Elsevier*, 56:376–389, 2002.

[WCCS03] Y.Y. Won, I.H. Chung, N.S. Chung, and K.H. Song. Morphological study on the acetabular labrum. *Yonsei Med J, Yonsei University College of Medicine*, 44(5):855–862, 2003.

[web] Osteomyelitis website. http://www.osteomyelitis.com/. Accessed November 2009.

[WHH+00] P. Westblad, K. Halvorsen, T. Hashimoto, I.G. Winson, and A. Lundberg. Ankle-joint complex motion during stance phase of walking as measured by skin or bone anchored markers. In *Proc of the 6th International Symposium on 3D Analysis of Human Movement*, pages 49–51, Cape Town, South Africa, May 2000.

[WLJ+08] P. Wolf, A. Liu, R. Jones, A. Arndt, A. Lundberg, and A. Stacoff. Rearfoot kinematics: Invasive quantification of the skin movement artifact. *J Biomech, Elsevier*, 41(1):S164, 2008.

[WN01a] J.M. Wakeling and B.M. Nigg. Modification of soft tissue vibrations in the leg by muscular activity. *J Appl Physiol, The American Physiological Society*, 90:412–420, 2001.

[WN01b] J.M. Wakeling and B.M. Nigg. Soft tissue vibrations in the quadriceps measured with skin mounted transducers. *J Biomech, Elsevier*, 34:539–543, 2001.

[WSA+02] G. Wu, S. Siegler, P. Allard, C. Kirtley, A. Leardini, D. Rosenbaum, M. Whittle, D. D'Lima, L. Cristofolini, H. Witte, O. Schmid, and I. Strokes. ISB recommendation on definitions of joint coordinate system of various joints for the reporting of human joint motion - part i: Ankle, hip and spine. *J Biomech, Elsevier*, 35(4):543–548, 2002.

[YC06] Lydia Yahia-Cherif. *Anatomical Modeling and Motion Study of the Human Hip Joint*. PhD thesis, Université de Genève, 2006.

[YCGMMT04] L. Yahia-Cherif, B. Gilles, T. Molet, and N. Magnenat-Thalmann. Motion capture and visualization of the hip joint with dynamic MRI and optical systems. *Computer Animation and Virtual Worlds, John Wiley and Sons*, 15,(3-4):377–385, July 2004.

[YCMMT04] L. Yahia-Cherif, T. Molet, and N. Magnenat-Thalmann. Motion simulation of the hip joint using an optimized markers configuration. In *Proc of the 8th International Symposium on 3D Analysis of Human Movement*, Tempa, USA, April 2004.

[YCMT06] L. Yahia-Cherif and N. Magnenat-Thalmann. Quantification of skin movements artefacts using MRI. In *Proc of the 9th International Symposium on 3D Analysis of Human Movement*, Valenciennes, France, June 2006.

[YHC+00] H.J. Yack, J. Houck, T. Cudderford, M. Pierrynowski, and K. Ball. Measuring 3D knee motion with surface markers, it can be done. *Gait & Posture, Elsevier*, 11(2):148–149, 2000.

[YOES08] G. Yavuzer, O. Oken, A. Elhan, and H.J. Stam. Repeatability of lower limb three-dimensional kinematics in patients with stroke. *Gait & Posture, Elsevier*, 27:31–35, 2008.

[ZGS+06] M.S. Zihlmann, H. Gerber, A. Stacoff, K. Burckhardt, G. Szekeli, and W. Stuessi. Three-dimensional kinematics and kinetics of total knee arthroplasty during level walking using single plane fluoroscopy and force plates: A pilot study. *Gait & Posture, Elsevier*, 24:475–481, 2006.